

# UC Santa Barbara

## UC Santa Barbara Electronic Theses and Dissertations

### Title

Novel studies of buffer gas cooled polyatomic molecules for chemical analysis

### Permalink

<https://escholarship.org/uc/item/4d69q47t>

### Author

Koumarianou, Greta

### Publication Date

2023

Peer reviewed|Thesis/dissertation

University of California  
Santa Barbara

**Novel studies of buffer gas cooled polyatomic  
molecules for chemical analysis**

A dissertation submitted in partial satisfaction  
of the requirements for the degree

Doctor of Philosophy  
in  
Chemistry

by

Georgia Koumarianou

Committee in charge:

Professor David Patterson, Chair  
Professor Lior Sepunaru, co-Chair  
Professor Songi Han  
Professor Mattanjah de Vries  
Professor Andrew Jayich

March 2023

The dissertation of Greta Koumarianou is approved.

---

Mattanjah de Vries

---

Songi Han

---

Andrew Jayich

---

Lior Sepunaru, Committee Co-Chair

---

David Patterson, Committee Co-Chair

March 2023

## Acknowledgements

I would like to thank my advisor David Patterson for being such a great scientific mentor and for all his support throughout my graduate studies. Dave, thank you for having such a refreshing and different approach on doing science, working by your side taught me how to approach scientific challenges in such a unique way and be confident for the scientist I am today.

I would also like to thank Irene Yang and Ben Riley, the two undergraduate students I worked most closely to. Thank you for taking data by my side and teaching me how fulfilling mentoring can be. Troubleshooting wouldn't be the same without you, and your accomplishments bring me lots of happiness! Additionally, I am thankful to all members of the Patterson Group, especially Lincoln Satterthwaite and Scott Eierman. Lincoln thank you for teaching me all about buffer gas cells and our experiment and introducing me into actually building things. Scott, our lunches, conversations and pastry breaks motivated me to keep pushing during the hardest times!

None of these experiences would have been possible without the continuous support from my amazing friends Vani, Shannon and Ann. Meeting you was such a highlight of my time at UCSB and my experience would have never been as positive without you. Lastly, I would like to specially thank my boyfriend Hector. Thank you for taking the risk to join me in California and being my biggest supporter throughout everything!

To future scientists in the making.

# Curriculum Vitæ

## Georgia Koumarianou

### Education

- 2023 Ph.D. in Chemistry (Expected), University of California, Santa Barbara.
- 2018 M.S. in Physical Chemistry, University of Crete, Greece.
- 2016 B.S. in Chemistry, University of Crete, Greece.

### Publications

- Kinetic Signatures of Quantum Tunneling in Water Dimer Formation (2023). **G. Koumarianou**, B. Riley, L.Satterthwaite, Y. Brynjegard-Bialik, D. Patterson. (Under preparation).
- Low-temperature gas-phase kinetics of ethanol-methanol heterodimer formation (2023). L.Satterthwaite, **G. Koumarianou**, P. B. Carroll, R. Sedlik, I. Wang, M. McCarthy, D. Patterson. *J. Phys. Chem. A* (Submitted).
- Assignment-free chirality detection in unknown samples via microwave three-wave mixing (2022). **G. Koumarianou**, I. Wang, L. Satterthwaite, D. Patterson. *Commun Chem* 5, 31.
- Sub-Hz differential rotational spectroscopy of enantiomers (2021). L.Satterthwaite, **G. Koumarianou**, D. Sorensen, D. Patterson. *Symmetry*, 14(1), 28.
- High-resolution resonance-enhanced multiphoton photoelectron circular dichroism (2020). A.Kastner, **G. Koumarianou**, P. Glodic, P. C. Samartzis, N. Ladda, S.T. Ranecky, T. Ring, S. Vasudevan, C. Witte, H. Braun, H. Lee, A. Senftleben, R. Berger, G. B. Park, T. Schäfer, T. Baumert. *Phys. Chem. Chem. Phys.* 22, 7404-7411.
- Formation of highly excited iodine atoms from multiphoton excitation of CH<sub>3</sub>I (2020). K. Matthíasson, **G. Koumarianou**, M. Jiang, P. Glodic, P. C. Samartzis, Á. Kvaran. *Phys. Chem. Chem. Phys.* 22, 4984-4992.
- Two-color studies of CH<sub>3</sub>Br excitation dynamics with MPI and slice imaging (2019). A. Hafliason, P. Glodic, **G. Koumarianou**, P.C. Samartzis, Á. Kvaran. *Phys. Chem. Chem. Phys.* 21, 10391-10401.
- Multiphoton Rydberg and valence dynamics of CH<sub>3</sub>Br probed by mass spectrometry and slice imaging (2018). A. Hafliason, P. Glodic, **G. Koumarianou**, P.C. Samartzis, Á. Kvaran. *Phys. Chem. Chem. Phys.* 20, 17423-17433.
- Highly spin-polarized deuterium atoms from the UV dissociation of deuterium iodide (2017). D.Sofikitis, P.Glodic, **G. Koumarianou**, H. Jiang, L. Bougas, P.C. Samartzis, A.Andreev, P. Rakitzis. *Phys. Rev. Lett.* 118, 233401.

## Abstract

Novel studies of buffer gas cooled polyatomic molecules for chemical analysis

by

Georgia Koumarianou

Cold molecules (1-7K) have been a powerful probe of cold chemistry, chemical analysis and fundamental physics beyond the standard model. By far the most widely used source of cold molecules have been the pulsed supersonic jet. In the past decade another cooling method known as buffer gas cooling has emerged for the production of cold diatomic and polyatomic molecules in a continuous manner. Buffer gas cooled molecules are brought to low temperatures via collisions with cryogenic gas, which enables faster acquisition and assignment of molecular spectra. Buffer gas cooling coupled with microwave spectroscopy has enabled novel applications in chiral detection and mixture analysis due to its high sensitivity. In this work, such capabilities are further expanded with a focus on chiral systems. I describe the experimental advances in buffer gas cell design, and then discuss three key results: the chiral detection of unknown multi-component mixtures, the first microwave differential precision measurement for probing parity violation effects in chiral molecules, and the study of low temperature formation kinetics of ethanol-methanol and water dimers. Finally, I discuss the source and effects of stray electric fields in the buffer gas cell and present preliminary efforts towards studying chiral imprinting and buffer gas cooled reactive species.

# Contents

<b>Abstract</b>	<b>vi</b>
<b>1 Introduction</b>	<b>1</b>
1.1 Microwave spectroscopy of cold polyatomic molecules . . . . .	1
1.2 Buffer gas cooling . . . . .	3
1.3 Motivation and thesis outline . . . . .	4
<b>2 Experimental Apparatus</b>	<b>6</b>
2.1 Introduction . . . . .	6
2.2 Cryogenic buffer gas cell . . . . .	7
2.3 Vacuum and cryogenics . . . . .	11
2.4 Sample introduction . . . . .	14
2.5 Electronics . . . . .	21
<b>3 Chirality detection with microwave three-wave mixing</b>	<b>24</b>
3.1 Introduction to chirality . . . . .	24
3.2 Measuring chirality using electric dipole interactions . . . . .	25
3.3 Assignment-free chirality detection in unknown samples . . . . .	31
<b>4 Stray electric fields in the buffer gas cell</b>	<b>57</b>
4.1 Observation of stray electric fields in the buffer gas cell . . . . .	58
4.2 Spontelectrics: Effects of spontaneous polarization of cryo-deposited films in the buffer gas cell . . . . .	64
4.3 Discussion and current solutions . . . . .	68
<b>5 Studying parity-violation effects in chiral molecules with microwave spectroscopy</b>	<b>70</b>
5.1 Measuring parity violation effects in chiral molecules . . . . .	71
5.2 Experimental . . . . .	76
5.3 Results . . . . .	80



5.4	Systematics . . . . .	82
5.5	Discussion . . . . .	85
<b>6</b>	<b>Low temperature dimer formation</b>	<b>90</b>
6.1	Low-temperature kinetics of ethanol-methanol and ethanol-water heterodimer formation . . . . .	92
6.2	Kinetic Signatures of Quantum Tunneling in Water Dimer Formation . .	106
<b>7</b>	<b>Future Directions</b>	<b>116</b>
7.1	Towards the observation of chiral imprinting via M3WM . . . . .	116
7.2	Studying Radical species in the buffer gas cell . . . . .	120
7.3	Singlet-oxygen barrierless photooxidations in a buffer gas cell . . . . .	130
	<b>Bibliography</b>	<b>133</b>

# Chapter 1

## Introduction

### 1.1 Microwave spectroscopy of cold polyatomic molecules

Understanding molecules as quantum mechanical systems is a central objective of chemical and molecular physics. Molecules, compared to atoms, display rich internal dynamics including electronic, vibrational, rotational, and spin degrees of freedom. These properties make studying molecules a much more complex process but if manipulated in a controllable way, molecules could comprise a very promising physics toolbox that operates in a wide range of different energy and time scales. Recent advances in producing cold molecular samples are motivated by the promise of new science in the areas of cold chemistry, chemical analysis and fundamental physics beyond the standard model. Such studies are essential for bridging experiment and theory and understanding molecular structure and interactions at a fundamental level.

Microwave spectroscopy has been used for decades as a spectroscopic probe of molecular structure. The relationship between structure and the rotational transitions through

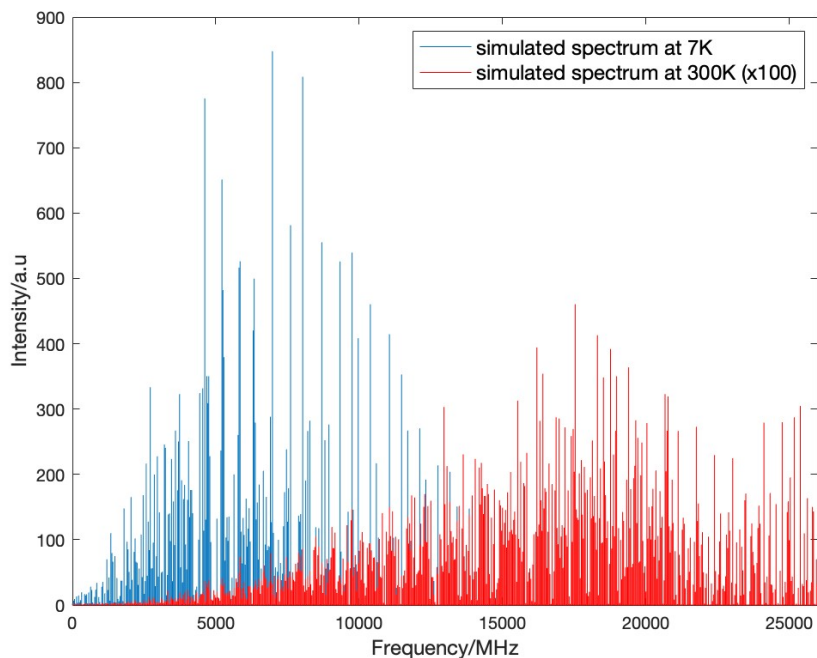


Figure 1.1: The simulated rotational spectra of 1,2 propanediol at 7K (blue) and 300K (red), up to the rotational levels with  $J=30$  using the PGOPHER package. The intensity of the transitions at 300K is multiplied by a factor of 100 for clarity.

the principal moments of inertia provides one of the most direct and accurate methods for structure determination of gas phase samples. From a rotational spectrum, one can extract information about fundamental structural properties such as centrifugal distortion, hyperfine spin-rotation and spin-spin effects, quantum tunneling, torsional and large amplitude effects. [1] However, all this information is extremely challenging to access from rotational spectra at room temperature because of their complexity. At room temperature, hundreds of rotational levels are occupied and the rotational partition function scales with temperature as  $T^{3/2}$ . This can be better seen in Figure 1.1, showing the simulated rotational spectra of 1,2 propanediol at 7K (blue) and 300K (red), up to the rotational levels with  $J=30$ . The intensity of the transitions of the room temperature spectrum are multiplied by a factor of 100. The complexity of the spectrum at room

temperature is one of the main reasons why microwave spectroscopy is not as widely used for chemical analysis as other methods like FTIR and NMR. The development of cold molecular sources tremendously benefited microwave spectroscopy showcasing its advantages to current chemical analysis methods.

The combination of supersonic-jet expansion techniques with Fourier transform microwave (FTMW) spectroscopy, especially the broadband chirped pulsed Fourier transform microwave method (CP-FTMW) revolutionized the field. Cold molecular samples (1-10 K) produced by molecular beams occupy less states according to  $T \leq \Delta E/k_b$  (where  $\Delta E$  is the energy spacing between levels), which combined with faster spectral acquisition capabilities, can lead to rotational spectra that are faster to acquire and simpler to assign. Current advances in microwave spectroscopy span the study of large van der Waals clusters, mixture analysis and chiral analysis. [2, 3, 4, 5, 6] Microwave spectroscopy is inherently molecule specific, allowing for simultaneous analysis of multi-component species, including their different conformers and isotopomers. Few examples of such capabilities have been demonstrated by the quantitative mixture analysis of natural essential oil samples and the conformational dynamics of small molecules.[7, 8] Two more noteworthy achievements paving the way for the future of the field is the structural studies of large water clusters [9, 10] and chiral recognition effects [11, 12].

## 1.2 Buffer gas cooling

Buffer gas cooling is a continuous cooling technique in which room temperature atoms or molecules are cooled via collisions with a cold buffer gas cell to low temperatures. Commonly used buffer gases are helium (4K), neon (20K) and argon (85K). Buffer gas cooling was pioneered by Frank de Lucia [13] for atoms and expanded to large polyatomic

molecules by the Doyle and Patterson Group.

The buffer gas cooling technique is quite general, as it can be adopted to a wide variety of different species. Small molecules (of roughly 10-15 atoms) can be routinely buffer gas cooled and in the past decade, the technique has been extended to larger polyatomic molecules as well. Nile Red ( $C_{20}H_{18}N_2O_2$ ) which comprises of 42 atoms has been buffer-gas cooled with helium buffer gas, while the Buckminster fullerene  $C_{60}$  holds the current record of the largest molecule buffer-gas cooled to 130 K with argon buffer gas.[14, 15] The technique has also been tested at organometallic species with heavier atoms, such as methyltrioxorhenium ( $CH_3ReO_3$ ), a promising candidate for parity violation studies [16]. As will be discussed further in this thesis, species such as van der Waals clusters and radicals also survive in the buffer gas environment which can be additionally utilized as a medium to study reaction kinetics and non-covalent interactions at low temperatures and not solely for thermalization.

### 1.3 Motivation and thesis outline

I first decided to join the Patterson group at UCSB to combine learning about cold molecule production and cryogenics, and apply it in doing spectroscopy on my favorite molecular property, chirality. I was very excited to be involved in designing and building the next novel state-of-the art chiral chemical analyzer and to innovate in physical chemistry by exploring the capabilities of buffer gas cells in studying molecules.

In this thesis which consists of six Chapters, I describe my journey. Chapters 1-2 can be considered a guide for readers interested in doing microwave spectroscopy in buffer gas cells from a chiral detection perspective. Chapters 2-5 contain our work showcasing a series of novel experiments made possible by advances in the buffer gas cell apparatus towards the new methods for extracting chiral information .

- Chapter 1: A brief description of the main concepts required to understand the experiments and motivation discussed in this thesis.
- Chapter 2: An experimental guide to the buffer gas cell apparatus with a focus on cryogenic design and sample introduction capabilities.
- Chapter 3: A detailed overview of our experimental results on producing three-wave mixing spectra, spectra that provide chiral information on-the-spot on unknown samples without the need for spectral assignment. This chapter contains a very detailed emphasis on the challenges faced and their solutions.
- Chapter 4: A report on stray electric fields inside buffer gas cells, including experimental data describing observed effect and its influence on experimental measurements, possible explanation and suggested solutions.
- Chapter 5: Our published results on the first precision differential spectroscopy result using microwave spectroscopy between two enantiomers. This result contributes towards understanding the systematics needed to measure parity violation effects in chiral molecules for the first time.
- Chapter 5: Experimental results on low-temperature dimer formation kinetics in a new updated buffer gas cell design. We extract formation rates at 10 K for ethanol and ethanol-methanol dimers and study conformational effects. We also collected kinetic data on water dimer isotopologue formation presenting insights on how tunneling motions participate in the dynamics via a quantum tunneling lens.
- Chapter 6: Future Directions. An overview of preliminary ideas and results for the next generation of experiments.

# Chapter 2

## Experimental Apparatus

### 2.1 Introduction

A large part of my thesis work involved the optimization and design upgrade of the buffer gas cell spectrometer with the goal of expanding its current experimental capabilities. The buffer gas cell apparatus is mainly designed as a microwave spectrometer that operates at cryogenic temperatures. Operating at 6 K allow us to produce less complex high sensitivity microwave spectra, taking advantage of the temperature dependence of the molecular partition function, low-noise amplification and high-speed data acquisition. In this chapter, I will describe in detail the apparatus design and requirements for the chiral detection, dimer formation and precision spectroscopy experiments described in following chapters.

## 2.2 Cryogenic buffer gas cell

The central components of the experimental apparatus is the cryogenic buffer gas cell and the molecular source.

### 2.2.1 Standard buffer gas cell design

A schematic of the standard buffer gas cell apparatus is shown in Figure 2.1. Gas-phase molecules in room temperature enter the cell, where they get thermalized via collisions with cold buffer gas. The cell is a (20cm  $\times$  20cm  $\times$  20cm) box made of superconductive copper 101. Two pairs of microwave horns are mounted at the back side of the cell, for performing microwave spectroscopy in the frequency range between 10-18 GHz and 18-26 GHz. Opposite to the horns' side, there is a spherical mirror with a curvature of approximately 8 inches. At the center of the mirror, there is an one inch diameter aperture for sample introduction. Molecules in the gas-phase reach the cell via a copper sample injection tube ( $R = 0.250$ ) that is positioned co-planar and center to the aperture. Microwave excitation pulses are emitted by one of the microwave horns, reach the curved mirror on the opposite side of the cell and get reflected back to the detection horn.

The entire cell is cooled down to 5 K via a two-stage closed cycle cryocooler (Cryomech compressor with a PT420 cold head). The 2nd stage of the cryocooler reaches a base temperature of 4.2 K. Additional heatloads related to material volume and thermal conductivity losses eventually raise the cell temperature by 0.5-1 K. Buffer gas cooling is a cryogenic experiment that takes place in high vacuum, therefore the cryogenic buffer gas cell is placed inside a vacuum chamber (300 K) and is further protected from blackbody radiation by a 0.125 inch thick aluminum radiation shield. A radiation shield made of superconductive copper 101 was adapted to future designs for faster and more efficient



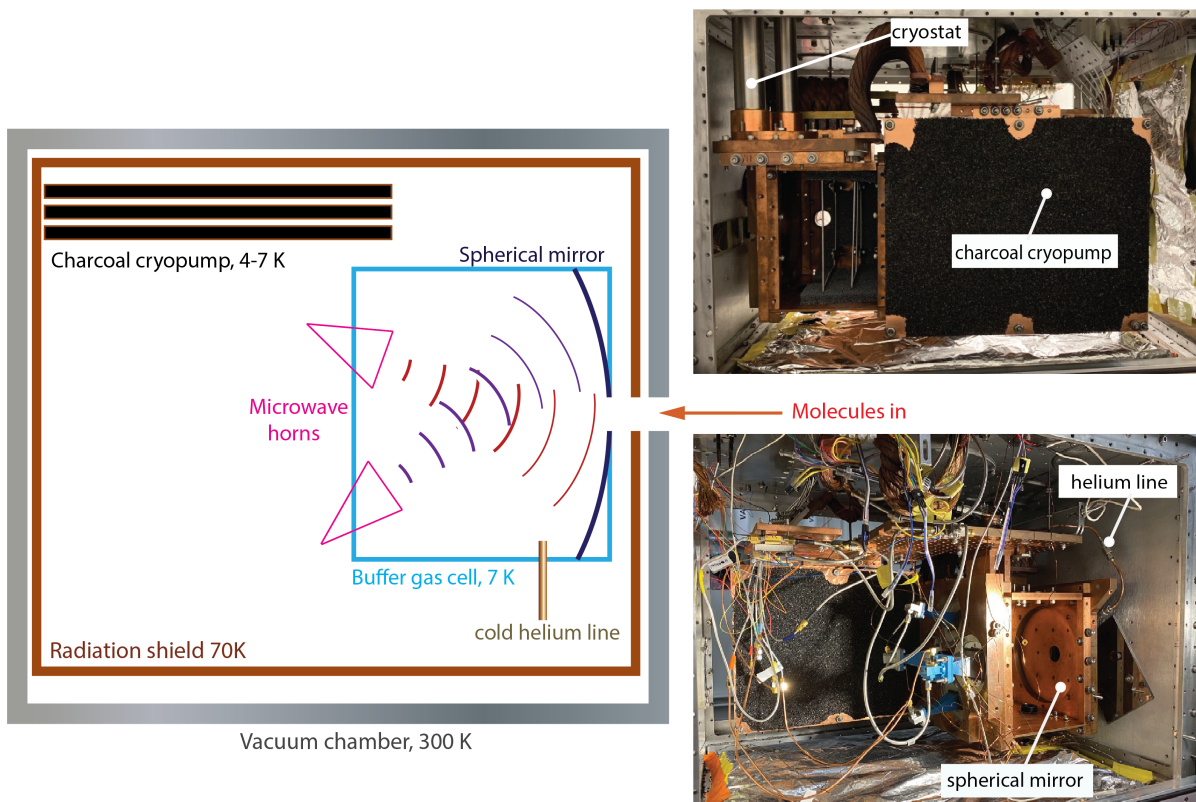


Figure 2.1: Schematic of the standard buffer gas cell apparatus. Molecules in room temperature enter the cell, where they get thermalized via collisions with cold helium gas. Microwave excitation pulses are emitted by one of the microwave horns, reach the curved mirror on the opposite side of the cell and get reflected back to the detection horn. Even though we are continuously adding gas-phase molecules and buffer gas at a rate of 10 sscm, cryopumps help maintain high vacuum by adsorbing the excess gas.

cooldowns. The radiation shield is thermally anchored to the 1st stage of the cryocooler and stays at a temperature between 45-70K. Aluminized mylar superinsulation is used as an additional layer of radiation shielding between the room temperature vacuum chamber and the radiation shield.

Helium gas enters from the cell via a cold line that is thermally anchored to the 2nd stage. We have tried two different configurations for the cold helium introduction line. In the original design [17], the helium enters the cell through a 12-hole pattern around the aperture on the spherical mirror. We also tried a simpler design where the helium

tube is attached to one of the side plates. Both methods performed similarly. Buffer gas is introduced at a typical flow rate of 8-12 standard cubic centimeters per minute (SCCM) controlled by a gas mass flow controller (Alicat Scientific). The neat sample is introduced typically at a rate of 4  $\mu\text{L}$  per second. Even though we are continuously adding gas-phase molecules and buffer gas, cryopumps help maintain high vacuum by adsorbing the excess gas. In this design, three stacked plates of charcoal cryopump are mounted outside the cell.

### 2.2.2 Second generation buffer gas cell

The next generation buffer gas cell was designed for high resolution and cold chemistry experiments in mind. As seen in Figure 2.2, the main difference between the two designs is the size. This buffer gas cell is 45 cm  $\times$  25 cm  $\times$  27 cm, occupying maximum volume of the vacuum chamber. In this design, there is no spherical mirror but instead a simpler horn configuration in which the two horns are facing one another.

The two designs share identical microwave circuitry and cryogenic components, except for the use of copper 101 radiation shield instead of aluminum. In this design, there are three sorb plates coated with activated coconut charcoal, that are approximately 45 cm  $\times$  25 cm and are stacked with spacers on the outward side of the back plate of the cell.

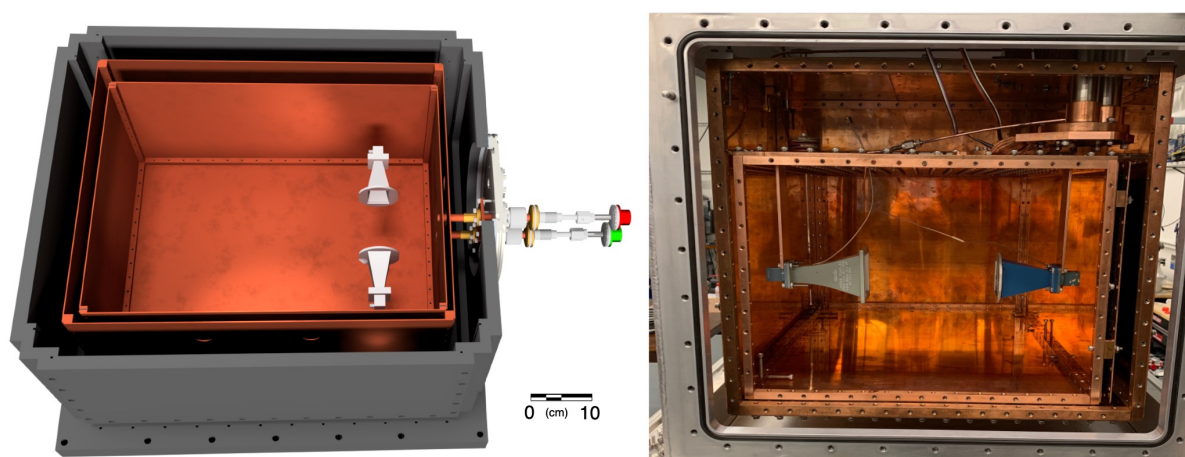


Figure 2.2: ((left) Schematic of the high-resolution buffer gas cell apparatus for studying dimer formation. Figure is adopted from [18] This cell is  $45\text{ cm} \times 25\text{ cm} \times 27\text{ cm}$ , occupying maximum volume of the vacuum chamber. A copper radiation shield was adapted for this design. (right) Image of the front view of the apparatus.

## 2.3 Vacuum and cryogenics

The chamber is pumped by a dry pump (Model EV-A10P, Ebara Technologies) with a pumping speed of 1000 L/min. This pump was specifically chosen because it is oil-free, has high atmosphere pumping speed and high water vapor pumping (gas ballast). It is important to run oil-free to maintain the adsorption capacity of the charcoal cryosorbs for longer times. We tried other type of dry scroll pumps like the Agilent Triscroll which effectively pumped down the chamber but at times struggled with water vapor pumping. It also required much more maintenance such as tip seal replacements every few months. During a standard cooldown, the dry pump pumps down the chamber from atmosphere to around 10 mTorr, in approximately 30 minutes. Then, the helium compressor brings the pressure down to high vacuum at  $10^{-6}$  mTorr and starts the cooling process which we usually do overnight. At equilibrium, the 1st stage of the cold head reaches approximately 40 K (top) 70 K (bottom) and the 2nd stage reaches 4.2 K. During the cooldown processes, different gases condense at different temperatures as seen in 2.3. At 4 K, only helium gas remains in the gas-phase. When we run the buffer gas cell with Neon gas, we use a small brass piece at the point where the 2nd stage connects with the buffer cell along with heaters to operate at 14-20 K.

### 2.3.1 Helium cryopumping with activated charcoal

To maintain high vacuum while continuously flowing buffer gas, we are cryopumping helium using sorbs made out of activated charcoal (Spectrum Chemical, mesh 8-30). Activated charcoal is a material with large surface area 1150-1250  $m^2/g$ . Albert G. Tobin et al. performed a thorough evaluation on its helium cryosorbing abilities including SEM images at high magnification demonstrating its large porosity. They measured a pumping speed of  $6.7 L/s \cdot cm^2$  and a pumping capacity of  $3.5 Torr \cdot L/cm^2$  .[19]

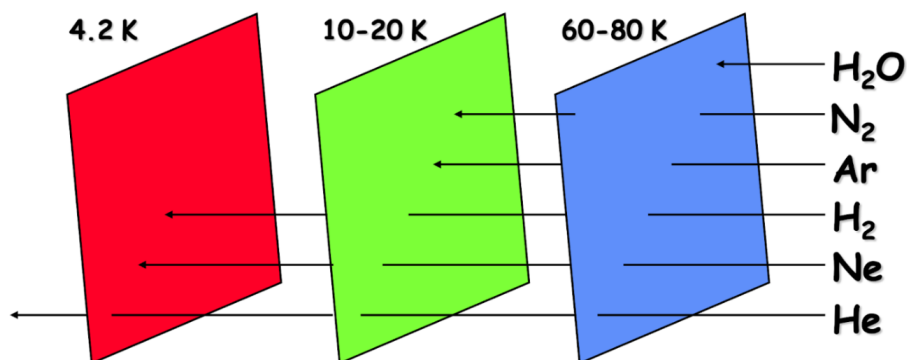


Figure 2.3: **Condensation temperatures for different common gases.** Image credits: L. Bertolini, Y. Li, LLNL

The cryosorbs we use are made out of stacked copper plates (9.5 x 12 inches, 1/16" thickness, super-conductive 101 copper). They are spaced 1/2" apart and they are thermally anchored to each other. The middle plate is anchored to the 2nd stage of the helium compressor which has a temperature of 5 K. The preparation of the plates involves three steps: 1) sanding of the copper surface, 2) coating the surface with epoxy (Stycast 2850FT epoxy mixed with Henkel Loctite catalyst 24LV curing epoxy hardener at 7.5:1 ratio), and 3) fully coating each side of the plate with the charcoal pellets. The curing process takes 24 hours with the catalysts we use.

The Stycast 2850FT epoxy has a thermal conductivity of  $1.01 \text{ W/m} \cdot \text{K}$ . I also tried using a different catalyst such as the Stycast 2850KT (that has a distinct blue color). This catalyst has a thermal conductivity of  $2.29 \text{ W/m} \cdot \text{K}$  and a shorter curing time (8-16h) than the 24LV catalyst, while also absorbing less water according to its specification. However, we observed no significant difference on the cooldown or runtime of the experiment.

For the rate of cryopumping needed for introducing 4-10 sccm of helium continuously for several hours, the sorb plate temperature, monitored by silicon diode sensors mounted on one of the plate, must remain below 8 K. When the sorb reaches its maximum capacity

or is under increased heatload, desorption begins leading to what we call “the crash”. During the crash, the helium is released and the pressure inside the chamber rises. In these conditions, thermal cycling to room temperature is necessary to regenerate the sorb. Sorb performance deteriorates with time and we typically replace the sorbs every six months. A sick sorb is easy to diagnose as it leads to shorter runtimes of the experiment and instant crashes after turning the helium buffer gas on and off more than once within the day. There is also some preliminary evidence that specific chemical species deteriorate the sorb performance dramatically after a few runs, these are fluorobenzene[20] and methanol [18].

The warm-up can take place naturally, where the temperature rises up after turning off the cryostat. To speed-up the process, we usually keep introducing buffer gas at 5-10 sccm, while the dry pump valve is on.

### 2.3.2 Temperature diagnostics

Silicon diode thermometers (DT670, Lakeshore) are positioned at various critical points of the apparatus as temperature diagnostics. For diagnosing the cryogenics, thermometers are placed at: the 1st stage of the cold head, 2nd stage of the cold head, cryosorb plates, top and bottom radiation shield, the cell and at the cryogenic amplifier.

A combination of the temperature readings between the cell with buffer gas on and off and the sorb plates can be very sensitive probes to the overall health of the experiment and can be very useful for day-to-day monitoring. This is a very straightforward way to optimize heat loads and fix unexpected issues especially when installing new components.

## 2.4 Sample introduction

Depending on the molecular species under study, there are various sample introduction methods compatible with cryogenic buffer gas cells: capillary injection, deposition on glasswool, pulsed valves with multiple inputs.

### 2.4.1 The capillary input manifold

As seen in Figure 2.4, liquid samples with high vapor pressure can be injected at specific sample rates ( 1-10  $\mu\text{L}/\text{sec}$ ) and transferred into the cell via a stainless steel capillary and standard high pressure liquid chromatography fittings. This method is described in detail in Ref.[17]. It has currently been replaced by the glasswool deposition method.

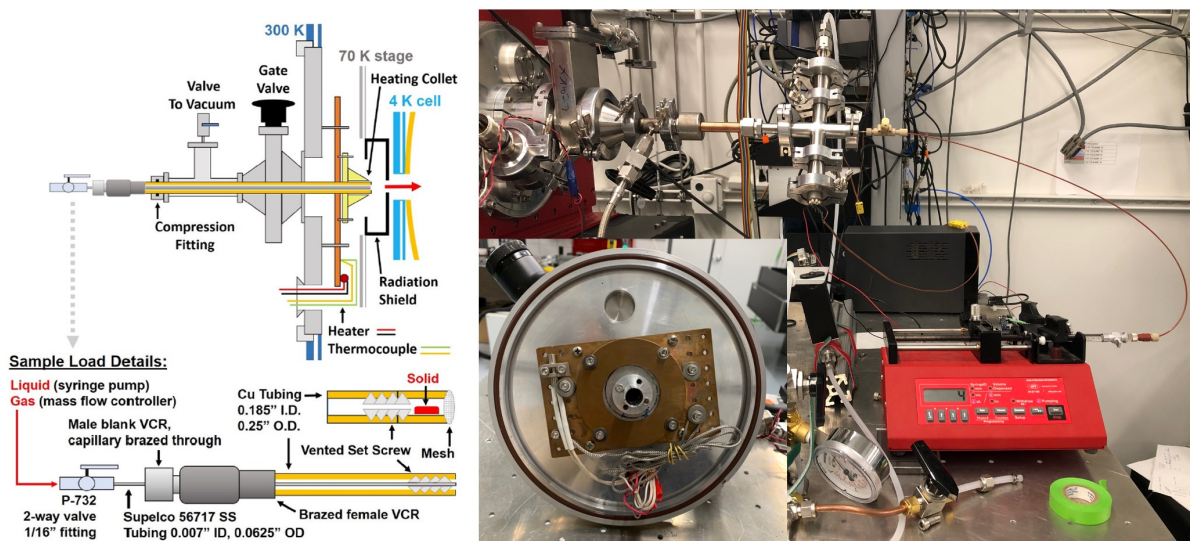


Figure 2.4: ((left) Schematic of the capillary input manifold. Figure was adopted from [17]. (right) Image of capillary injection setup. The sample is deposited inside a syringe placed in a syringe pump station. Standard liquid chromatography capillaries and fittings are used to transfer the sample from the syringe within the heated copper tube and then into the cell as molecules in the gas phase.

## 2.4.2 Glasswool deposition method

The heated capillary method, used in previous experiments [17], caused signal fluctuations. As a result, the signal amplitude of our microwave signals would vary randomly over time as a result of events that also caused temperature spikes on the experiment's temperature log, as the ones seen at the bottom graph of Figure 2.5. We soon figured out that these spikes were caused by random vaporization events and the solution involved incorporating a material with high surface area and high heat capacity for smoother vaporization.

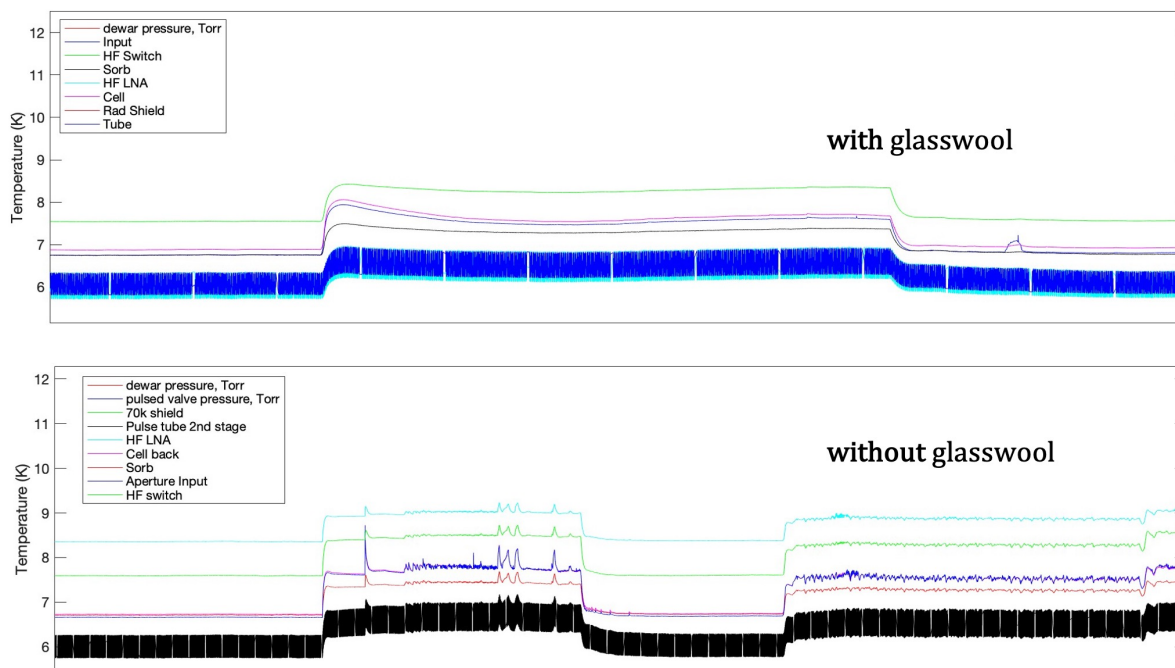


Figure 2.5: Temperature logs of the experiment before and after the use of glasswool. Poor sample reproducibility could be monitored by spurious temperature spikes(top). After introducing glasswool, the spikes are gone.

In gas chromatography, the liquid samples are also injected and being vaporized before analysis. According to [21, 22], in some cases the aerosol enters the chromatographic column without being fully vaporized leading to poor sample transfer and non-reproducible results, with the main reason being rapid temperature changes at the point of injection.



In our case, hot droplets failing to vaporize on time falling onto the the 6K surface and leading to uncontrolled vaporization events could also be the cause of the spikes and high signal fluctuation. The chromatography community solved this by using injection liners with packing materials, such as glasswool. Glasswool has high surface area and high heat capacity. It can minimize the temperature drop while ensuring the sample has enough time to be vaporized gently. [22, 23, 24, 25]

As seen in Figure 2.7, we initially packed glasswool at the tip of the copper tube where the liquid exited the capillary. Heaters were also added closer to the tip of the capillary and the glasswool. As seen in the bottom of Figure 2.5, adding glasswool solved the spikes issue and resulted in more effective and gentle evaporation. It is also a much simpler design since it does not require the use of capillary tubes to transfer the sample. The liquid sample is directly deposited onto the glasswool inside a small volume separated from the cell via a valve (Edwards SP10K Speedivalve). Alternatively, it can be injected via a septum, without breaking vacuum, as seen in Figure 2.7. The amount of molecules entering the cell can be monitored via their heatload effect to the cell temperature and be easily controlled by adjusting the speedivalve. This way, we are able to introduce as many molecules we want per unit time, with the only limitation being the cryogenics and the thermalization rate (cold helium density).

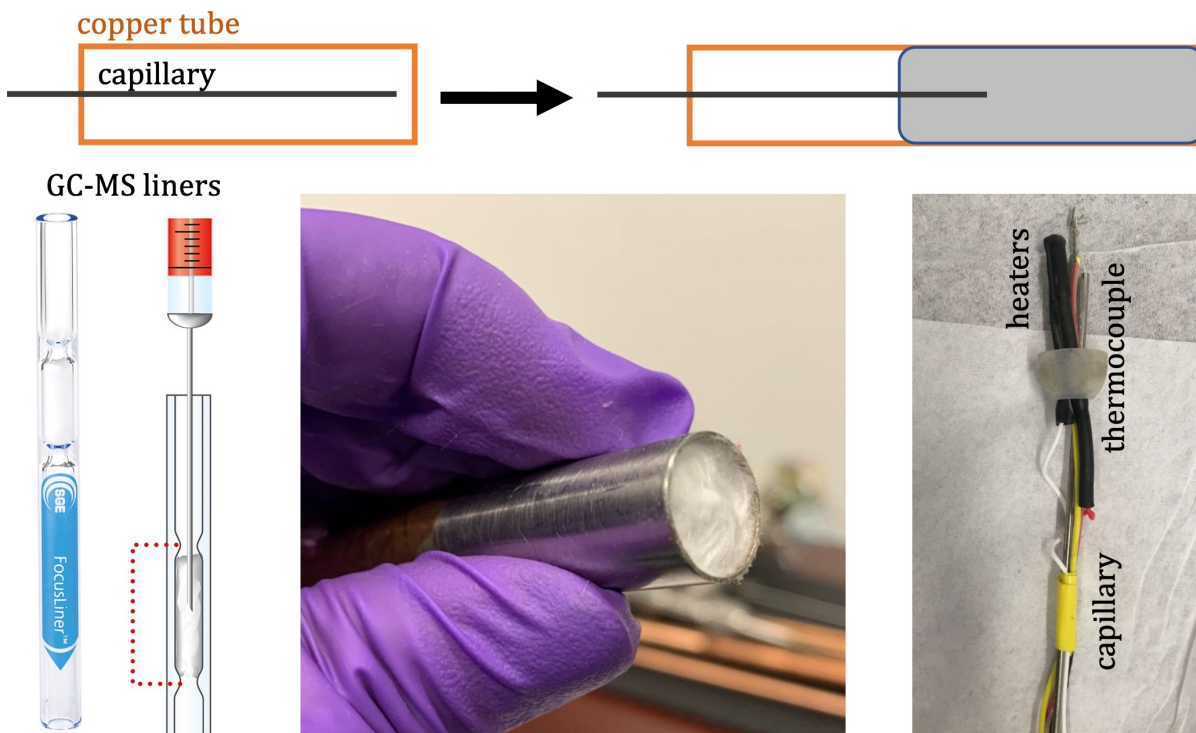


Figure 2.6: Schematic of sample introduction design with and without the glasswool packing material. The design was inspired by the gas chromatography liners. For the initial design, we loosely packed glasswool at the front of the copper tube and added heater close to the exit of the stainless capillary tube.

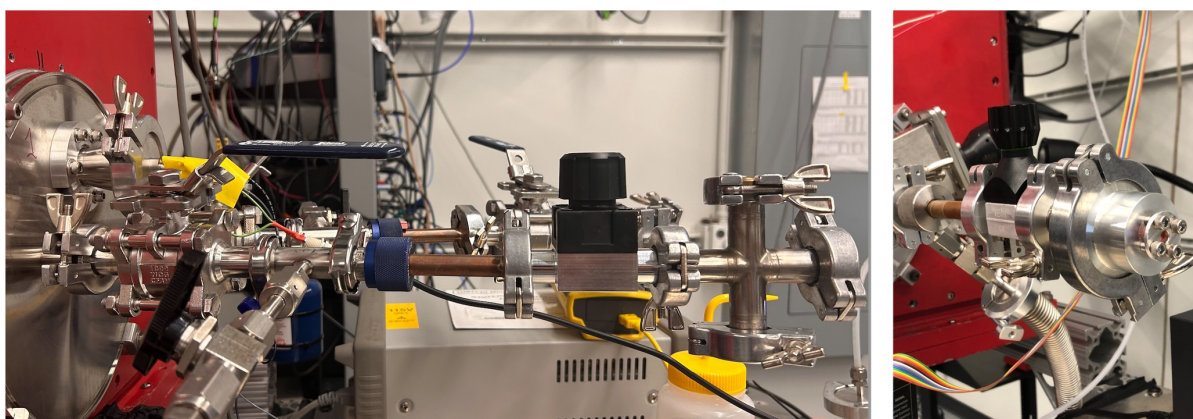


Figure 2.7: Image of glasswool-KF sample introduction setup. Sample can also be introduced through injection via a septum without breaking vacuum

### 2.4.3 Multiple and pulsed sample introduction

With the development of the next generation of buffer gas cell with larger volume, we wanted to study reactions or clusters formed inside the cell. For these experiments, we designed a new flange with four different sample inputs. Each of them is independently pumped and heated to keep reactants separate till they are introduced into the buffer gas cell. The four-input setup is compatible with any of the other sources such as the capillary, glasswool or a standard Parker 9 series pulsed valve. For the setup seen in Figure 2.8 used for the dimer formation experiments, explained in detail in following chapters, we used a Parker 9 series pulsed valve.

The next generation of this setup is a double-input angled version, as seen in Figures ???. The two copper tubes, loaded with different samples, enter the cell at an angle of 12 °for increased interaction volume between two reactants. This input is built and coupled to the standard buffer gas cell for measuring induced enantiomeric excess upon chiral dimer formation, as described more in detail in the Future Directions chapter.

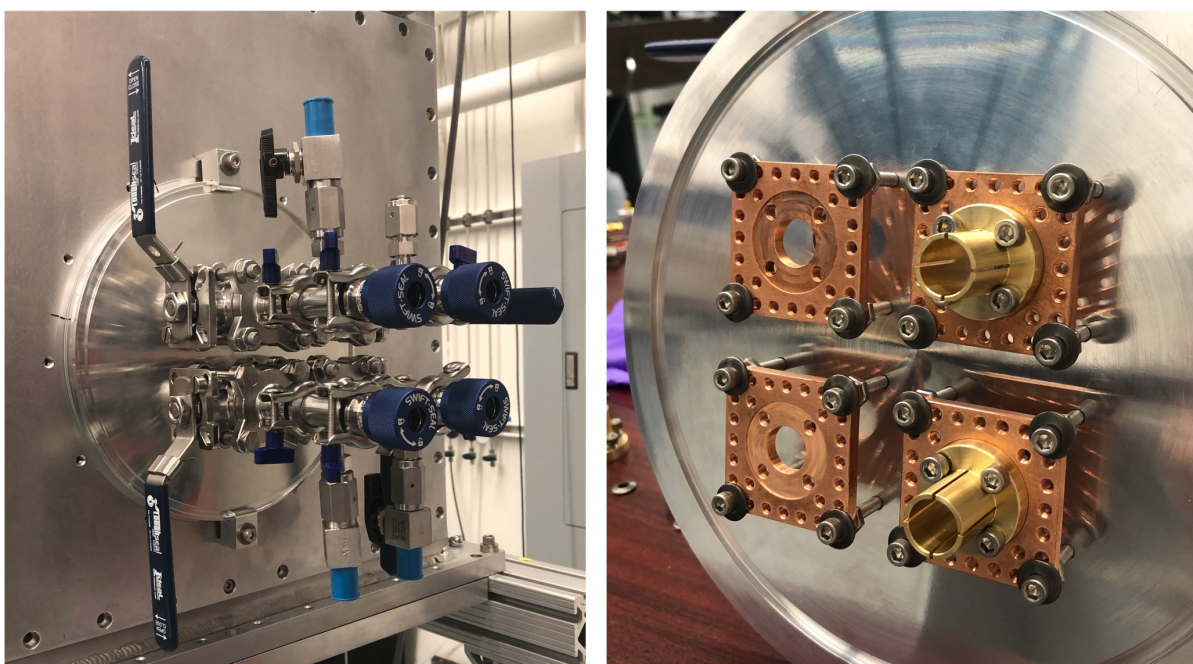


Figure 2.8: Four-input sample introduction setup. Each input has an independent vacuum interlock and heating system (brass sleeve) to keep reactants separate till they are introduced into the buffer gas cell. This setup was used for the low temperature dimer formation kinetic experiments.

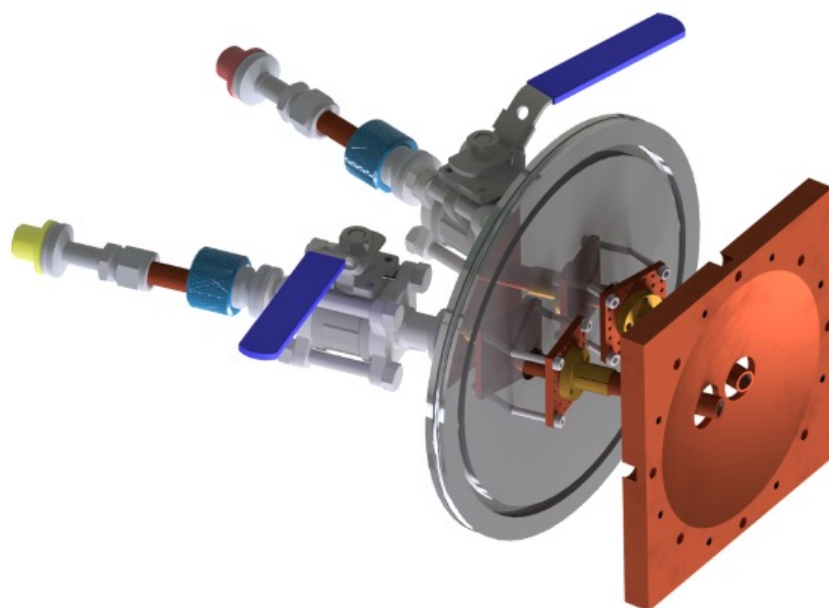


Figure 2.9: Double-input angled sample introduction setup for larger cross-section between two reactants entering the buffer gas cell. This input was built for the proposed chiral imprinting experiment described more in detail in the Future Directions chapter.

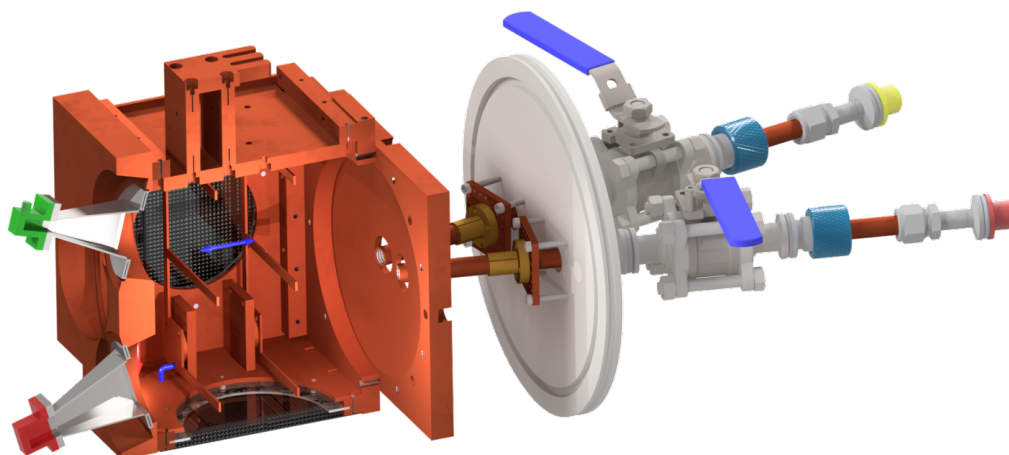


Figure 2.10: Double-input angled sample introduction setup coupled to the buffer gas cell for chiral analysis.

## 2.5 Electronics

The electronics for operating a microwave spectrometer in a cryogenic buffer gas cell perform three main operations: (1) TTL control, (2) production and manipulation of microwave sources, and (3) digitization and rapid data acquisition.

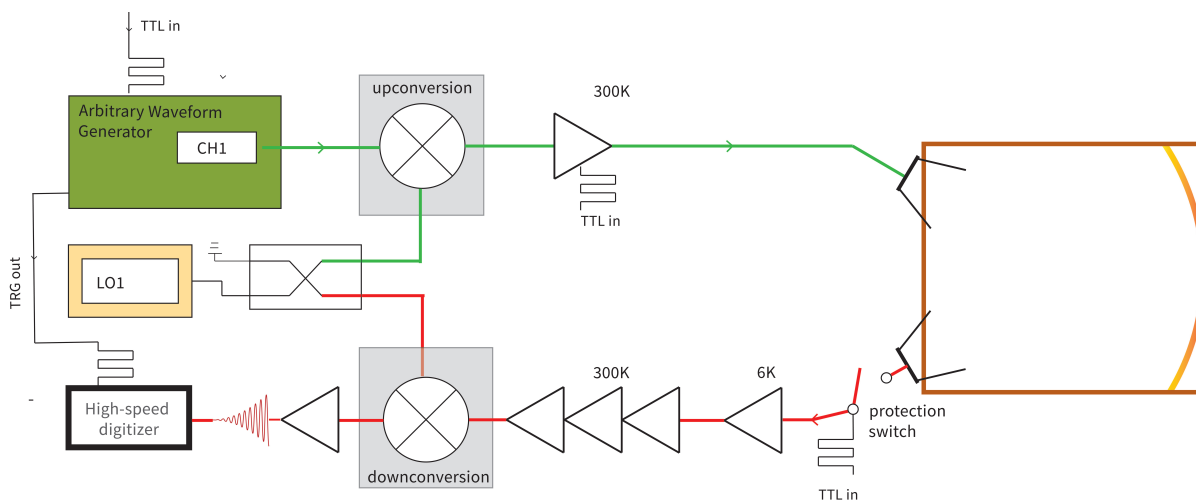


Figure 2.11: Microwave electronic circuit diagram for performing microwave spectroscopy in a buffer gas cell. Main components such as microwave sources, synthesizers, mixers and amplifiers are shown by their standard symbols.

A simplified schematic of the microwave circuit is presented in Figure 2.11, and specific details of all parts are included in Table 2.1. The spectrometer can be operated in two frequency regimes 11-18 GHz and 18-26 GHz. The circuit configuration for both cases is the same but each frequency range requires the equivalent microwave components rated for that frequency range. These ranges were chosen for three main reasons: cost-effectiveness, size and convenience. In this frequency range, most polyatomic molecules display hundreds of transitions, while the microwave components such as the horn antennas are small in size (order of five-ten centimeters) and can easily fit to the buffer gas cell. Electronic components such as amplifiers and cables are also much more affordable and outweigh the advantages of working at higher frequencies.

Table 2.1: Table of standard components used for microwave spectroscopy experiments in a buffer gas cell.

<b>Component</b>	<b>Part details</b>
Arbitrary waveform generator	Siglent SDG6052X 250 MHz
TTL pulse generator	Doyle Event Generator (DEG) custom-built
Event delay generator	SRS 4 channel delay generator, DG645
Synthesizer	Local oscillator Hewlett-Packard-8673D
Cryogenic Amplifier, 6-20 GHz	Low Noise Factory, LNF-LNC6 20C
Cryogenic Amplifier, 15-29 GHz	Low Noise Factory, LNF-LNC15 29B
Protection switch	Analog Devices, HMC547ALC3, DC-28 GHz
Drive Amplifier, 12-18 GHz	Mercury systems power amplifier LL1218-32-T325
Drive Amplifier, 18-26 GHz	Mercury systems power amplifier L1826-32-T325
Data acquisition card	Keysight U1084A
Gain horn antenna, 12-18 GHz	Pasternak (PE9854/SF-20)
Gain horn antenna, 18-26 GHz	Pasternak (PE9852/2F-20)
Other amplifiers	Narda-MITEQ Amplifier JS4-00102600-30-10P, Analog Devices HMC962LC4

The overall timing of the experiment is controlled by a homemade programmable transistor-transistor logic (TTL) pulse generator, triggering the generation of a chirp pulse from the Arbitrary Waveform Generator (AWG). The AWG triggers a delay pulse generator which further controls the timings of the power amplifiers and the cryogenic protection switch. A typical timing diagram of a microwave spectroscopy experiment is shown in Figure 2.12, highlighting the timing sequence of main events. During excitation of the microwave chirped pulse, that typically lasts 1-4  $\mu$ seconds, a safety switch remains on for 0.5  $\mu$ seconds before and after for protecting the sensitive detection electronics. Broadband microwave pulses are generated by mixing the chirp from the AWG with the output of a tunable synthesizer (10-26 GHz range). Upon mixing, the upconverted chirp, at the desired frequency, is further amplified in room temperature and broadcasted by a horn antenna. The microwave molecular signal emitted following excitation is collected by a receiver horn antenna. It passes through the protection switch and is amplified by a

cryogenic low noise amplifier (LNA) and a series of room temperature amplifiers before getting downconverted. During downconversion, the microwave signal is mixed down with the same output of a tunable synthesizer to lower frequencies and fed into a high speed acquisition card. Many individual FIDs are combined in the time-domain prior to the Fourier transform that produces the spectrum. A typical experiment consists of 15 averages each of which consists of the sum of 30000 waveforms. This is possible due to the continuous nature of the buffer gas cooling method allowing for data acquisition as fast as every 30  $\mu$ seconds. This allows for higher data acquisition speed than experiments with pulsed sources with repetition rates of 10 Hz. [17]

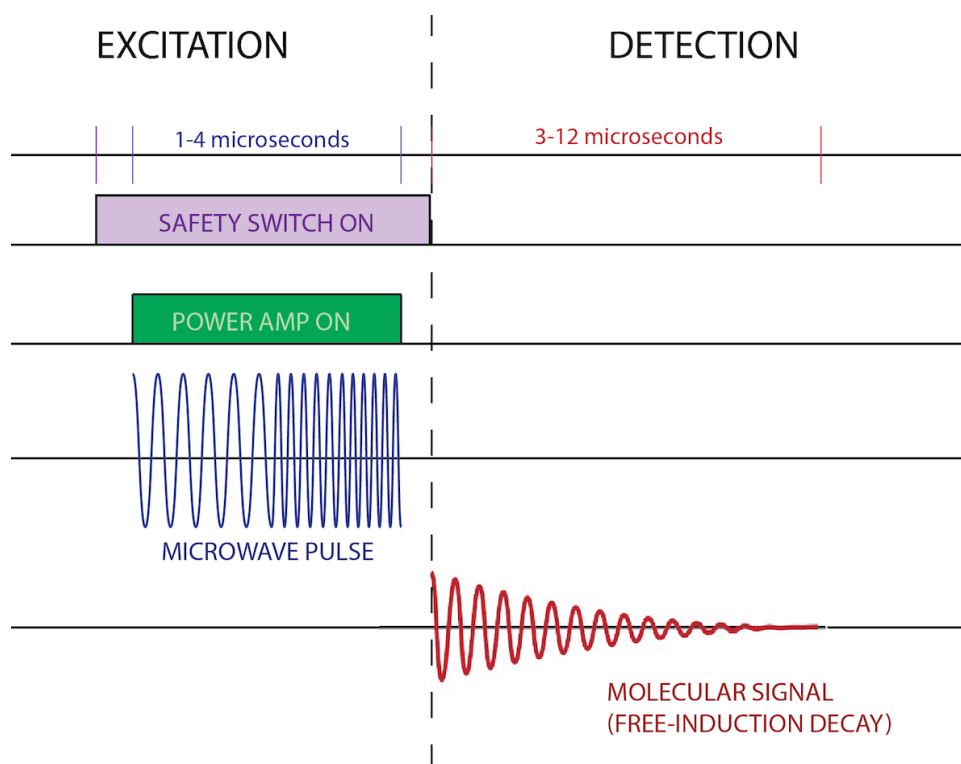


Figure 2.12: A typical timing diagram of a microwave spectroscopy experiment. During excitation of the microwave chirped pulse that typically lasts 1-4  $\mu$ seconds, a safety switch protects the sensitive detection electronics. Following the excitation, the molecules emit a coherent molecular signal, called free induction decay. It usually lasts 2-12  $\mu$ seconds and its duration is transition-dependent and buffer gas density-dependent. This pulse sequency limits the repetition rate to a typical experimental to roughly 50 KHz.



# Chapter 3

## Chirality detection with microwave three-wave mixing

This chapter describes in more detail, the work in reference, “Assignment-free chirality detection in unknown samples via microwave three-wave mixing (2022). **G. Koumari-anou**, I. Wang, L. Satterthwaite, D. Patterson. *Commun Chem* 5, 31.”

### 3.1 Introduction to chirality

Chiral molecules can exist in two versions that are non-superimposable mirror images of one another, called enantiomers. It is impossible to transform one enantiomer into the other without breaking a chemical bond. Chirality is also described as the property of handedness, since we can refer to the two versions as the right-handed version and the left-handed one.

A very important chirality measurement is the percent of enantiomeric excess (% of ee), which describes the ratio between the right and left versions. This is a key property since chiral biomolecules such as DNA, proteins, amino acids exist only in one version in

living organisms. Enantiomeric excess is a unique signature of biological activity. Therefore, it is quintessential for answering open questions about the origins of life, looking for life as we know it on other planets and design methods to accelerate the synthesis of chiral pharmaceuticals. Developing new analytical methods for reliably measuring enantiomeric excess and determining the absolute configuration in samples such as real-life complex mixtures and pharmaceuticals is of great importance. Drug development relies heavily on the design of asymmetric synthetic methods to produce one of the enantiomers to minimize drug side effects, while measuring enantiomeric excess in planetary samples can provide invaluable insights on life.<sup>2</sup>

## 3.2 Measuring chirality using electric dipole interactions

It is generally true that one can distinguish a chiral object via interacting with another chiral object. In the case of Absorption Circular Dichroism, circularly polarized light, which is chiral light, interacts differently with the two enantiomers of a chiral molecule. The interaction with the magnetic field leads to a chiral discriminating response, but the signal is weak since it is proportional to the size of the molecule in comparison with the pitch of the helix of the light which is usually at the UV-VIS region, within the electric dipole approximation.

Microwave three-wave mixing (M3WM) is a chirality detection method based on electric-dipole interactions, with an underlying mechanism different than common methods such as Circular Dichroism (CD), Vibrational Circular Dichroism (VCD) and Raman Optical Activity (ROA). It exclusively uses electric-dipole allowed interactions leading to much stronger chiral response within the electric dipole approximation. This is also

related to one of the most common questions about M3WM, which is how does it measure enantiomeric excess without circularly polarized light. A thorough perspective on this was described by A.F Ordonez et al. [26] using the idea of chiral setups, which are experimental setups with defined handedness to describe how electric-dipole methods are able to measure chirality in isotropic molecular samples. The handedness of the setup acts as the second chiral object needed to probe the chirality of the molecules. Other popular electric-dipole methods are 1) Photoelectron Circular Dichroism (PECD), 2) Photoexcitation Circular Dichroism (PXCD) and 3) Photoexcitation Photoelectron Circular Dichroism (PXECD). A.F Ordonez et al. discuss thoroughly the similarities on the theory behind these methods, with a main emphasis on PECD, which has been studied more extensively both theoretically and experimentally[27, 28] than M3WM.[26]

### **Chirality detection using microwave spectroscopy**

Microwave spectroscopy probes rotational transitions which are the most accurate spectroscopic measurements of chemical structure. There are three types of rotational transitions seen in microwave spectra, the a-, b-, c-type that are associated with the three rotational axes A, B, and C in three dimensions.

The majority of chiral molecules are completely asymmetric ( $C_1$ ) and their rotational spectrum can be described by the asymmetric top Hamiltonian. Chiral molecules of  $C_1$  symmetry have non-zero dipole moments along A,B and C axes which means that they display all three types of rotational transitions.

In 2012, Eizi Hirota proposed theoretically a new enantiospecific spectroscopic method based on a triple resonance experiment between rotational levels.[29] He suggested an excitation scheme that combines an a-type, b-type and c-type rotational transition to differentiate between enantiomers and measure enantiomeric excess. This experiment, now known as Microwave Three-Wave Mixing (M3WM), was later realized experimentally by Patterson et al.[30] using enantiopure samples of 1,2-propanediol.

Microwave Three-Wave Mixing (M3WM) [30, 2] is a polarization and phase sensitive method. The three transitions form a closed loop (or triangle) like the one shown in Figure 3.1. We refer to the first excitation pulse as the **drive** pulse and the second excitation pulse as the **twist** pulse. The detected molecular coherent signal produced is the **listen** pulse. The drive and listen pulses are linearly-polarized and perpendicular to one another. The listen pulse, which is the coherent molecular signal, is detected as a free-induction decay (FID) with polarization that is mutually orthogonal to the first two orthogonal fields and differs by  $\pi$  radians for the two enantiomers. This scheme forms a chiral setup as the ones described previously by Ordonez et al.[26]

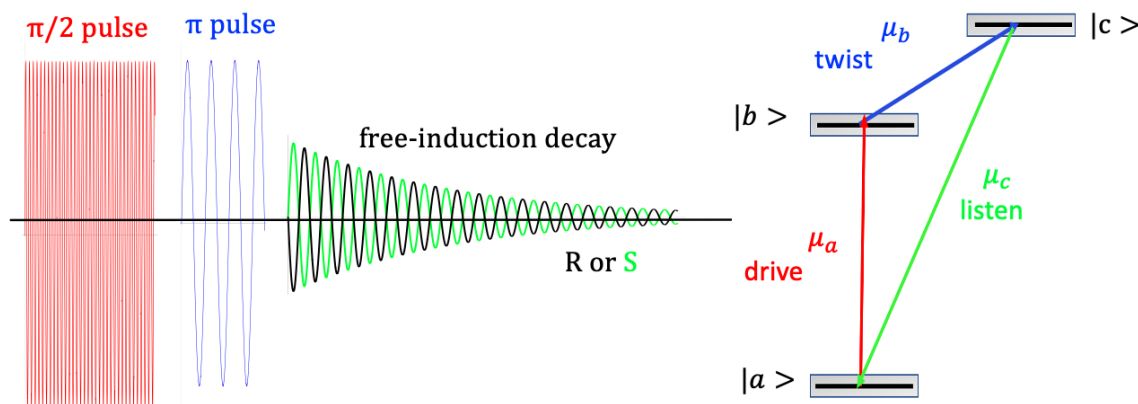


Figure 3.1: Pulse sequence and energy level schematic of a M3WM experiment. The drive transition is  $\pi/2$  pulse, followed by the twist  $\pi$  pulse. The rotational signal is obtained as a free-induction decay (FID) mutually orthogonal to the first two orthogonal fields and with a phase difference of  $\pi$  between the two enantiomers.

The transition matrix elements for the rotational transitions associated with each of those axes are proportional to  $\langle \Psi_1 | \mu_a | \Psi_2 \rangle$ ,  $\langle \Psi_1 | \mu_b | \Psi_2 \rangle$ ,  $\langle \Psi_1 | \mu_c | \Psi_2 \rangle$  where  $\mu_a$ ,  $\mu_b$  and  $\mu_c$  are the corresponding dipole moments.[31]. In the example shown in Figure 3.1, the drive is  $\pi/2$  pulse a-type transition that creates a coherent superposition between states  $|a\rangle$  and  $|b\rangle$ . The twist pulse is  $\pi$  pulse b-type transition that employs a coherence transfer between states  $|b\rangle$  and  $|c\rangle$ . The listen pulse is the c-type transition connecting  $|b\rangle$  and

$|c\rangle$  that has a phase difference of  $\pi$  due to the sign of the dipole triple product. The sign of any of two electric dipole components is arbitrary but the sign of the triple product  $|\mu_a\mu_b\mu_c|$  is independent of axis selection and changes sign under spatial inversion. This quantity can be used for chiral discrimination since it is opposite for enantiomers of the same chiral molecule and zero for a non chiral molecule.

From all rotational transitions of a given molecule, most of them do not have a pair of other two transitions at the right frequencies in our range to be able to form the closed 3WM triangles. For example, a chiral triangle for 1,2 propanediol consists of the  $|2_{11}\rangle \rightarrow |2_{21}\rangle$  transition at 14795.72 MHz, the  $|2_{21}\rangle \rightarrow |2_{10}\rangle$  at 100.5 MHz and the  $|2_{20}\rangle \rightarrow |2_{11}\rangle$  at 14896.22 MHz. To determine the 3WM transitions for a new molecule, calculated transitions from a simulated spectrum are sorted and checked for this frequency requirement between a-, b- and c-type transitions.

The relationship between the triple dipole product and the induced listen field with polarization  $P$  can be understood better via the following equation in the weak field limit [6, 32]:

$$\hat{P}_{listen}(t) \propto ee \cdot |\mu_a\mu_b\mu_c| \cdot \cos\left(2\pi vt + \frac{\pi}{2} \frac{\mu_a\mu_b\mu_c}{|\mu_a\mu_b\mu_c|}\right) \quad (3.1)$$

where  $ee$  stands for enantiomeric excess,  $\mu_a, \mu_b, \mu_c$  are the permanent dipole components,  $v$  is the listen frequency. The signal amplitude is proportional to the enantiomeric excess ( $ee$ ). The signal is zero for any molecules with zero dipole moment along any of the three rotational axes and the net signal is zero for racemic mixtures. Signal can be calibrated to known  $ee$ , to get specific  $ee$  information. The phase of the induced signal changes sign with enantiomer and its amplitude is a quantitative measurement of enantiomeric excess. This signal is also of comparable order of magnitude as conventional Fourier transform microwave spectroscopy (FTMW). [6]

There is a second type of chirality, known as axial chirality. These molecules exhibit  $C_2$  symmetry which is the symmetry of a threaded rod seen in molecules such as hydrogen peroxide ( $H_2O_2$ ) and ethanol ( $CH_3CH_2OH$ ). The three-wave mixing scheme can't be employed to  $C_2$  molecules because the dipole moment along their main symmetry axis is zero by definition.

### Other M3WM experiments

Even though M3WM was first demonstrated using buffer gas cooled molecules as the cold molecular source, it has also been shown in molecular beam setups.

Shubert et al. [4, 5] measured M3WM on two different conformers of carvone and 4-carvomenthenol determining enantiomeric excess and absolute configuration. The apparatus used was a conventional CP-FTWM spectrometer with minor modifications. In 2015, Lobsinger et al. [3], reported a new modification on the CP-FTWM spectrometer using four antennas instead of the RF electrode. In this way, one could take advantage of larger frequency ranges but also better optimization control of the chiral signal. The molecule under study was solketal.

Domingos et al. [6] expanded the M3WM capabilities to menthone, which is a chiral molecule with two stereogenic centers and one of the main component of peppermint essential oil. They demonstrated M3WM for menthone and isomenthone chiral species in the commercially available sample of the oil and calculated ee based on calibrating with enantiopure samples.

A different direction towards exploring M3WM capabilities into purifying chiral samples was shown by Eibenberger et al.[33] and Perez et al.[34] in a buffer gas cell and molecular beam setup, respectively. To achieve enantiomer-specific population transfer, an additional microwave pulse at the same frequency as the listen is applied. This pulse must be orthogonal and phase coherent to the drive and the twist. The phase of the third pulse is varied between  $-\pi$  and  $\pi$  and at certain phase, one of the enantiomers is

selectively transferred to a specific state. A fourth transition connected to the state was used as the readout.

Recently, Moon et al.[35] from Missouri University of Science and Technology constructed a working microwave three-wave mixing (M3WM) experiment with multiple arbitrary waveform generators. They demonstrated three-wave mixing for carvone and are planning to expand the method for studying nuclear quadrupole coupling effects in chiral molecules.

## 3.3 Assignment-free chirality detection in unknown samples

### 3.3.1 Introduction

Despite the broad applications of chiral molecules in the pharmaceutical, food, agriculture, and fragrances industry, a general method for detecting and measuring enantiomeric excess remains elusive. While notable progress has been made towards detection of slight enantiomeric excess on the 0.4% level [36], detection of enantiomeric excess in unknown complex samples has proven challenging. Chromatography has long been the go-to method for enantiomeric analysis among synthetic chemists, however, as detection is based on chemical interactions, it cannot be generalized to unknown samples. Mass spectrometry and Nuclear Magnetic resonance (NMR) rely on chiral derivitization reagents and can be sensitive to contaminants[37, 38, 39, 40, 41]. For unknown multi-component mixtures, polarimetry can be inconclusive, as the calculation of specific rotation requires knowledge of concentration and it is often referenced to neat samples[42, 43, 44].

Spectroscopic methods such as vibrational, photoelectron circular dichroism[45, 46, 47, 48, 49], and microwave spectroscopy [50, 51, 52, 53, 54, 55, 56, 57, 58] can be mixture compatible and provide highly accurate information on species identity. So far, these methods have been limited by spectral assignment; prior to any chirality experiment, the spectrum of the molecule had first to be collected and fully assigned.

Spectral assignment is the process of extracting information out of a spectrum by assigning its transitions. For a rotational spectrum, it involves the determination of A, B, C rotational constants, centrifugal distortion constants and more subtle effects depending on the molecular species. An assigned microwave spectrum provides extremely accurate information on the molecular structure at the conformer, isotopomer, diastereomer level.



However, it is a challenging and time-consuming process even for trained spectroscopists, even though there are active efforts to automate and simplify the assignment process [59, 60, 61, 62]. That is one of the main reason that microwave spectroscopy, even though information-rich, is not a method widely used for chemical analysis.

In this work, we demonstrate a generalized assignment-free version of microwave three-wave mixing (M3WM)[30, 2, 6] that can identify chiral species in enantiomeric excess in unknown complex samples. We achieve this by exploiting our high sensitivity and employing broadband excitation pulses to search experimentally for transitions in a three-level system, along with implementation of careful cancellation schemes to ensure that signals from species not in enantiomeric excess are subtracted. The resulting spectra, referred to here as “three-wave mixing spectra”, can provide direct proof on the existence of chiral species in enantiomeric excess and can be used for the study of previously hard-to-analyze samples: unassigned species and unknown complex mixtures. While the samples used in this work were not prepared by an outside team and were thus strictly speaking ‘known’ to our team, M3WM and proof of enantiomeric excess was demonstrated on these samples with no sample-dependent settings.

### **Broadband three-wave mixing**

Our broadband assignment-free three-wave mixing uses broadband microwave and RF excitation combined with careful cancellation schemes. Polarization and phase controllability for broadband pulses are achieved with an updated experimental setup and microwave circuit (discussed more in detail under Methods). While knowing the exact phase of the relevant component of each chirp is challenging, the repeatability of this phase is excellent, as it must be in all chirp pulse microwave three wave mixing experiments, and it can be accurately reversed by changing the phase of the signal coming from the arbitrary waveform generators. The resulting three-wave mixing spectra include numerous transitions from each chiral molecule that is present in enantiomeric excess. Each

of those transitions stem from a M3WM excitation scheme, an example of which is shown in Figure 3.2(b). It is a three-level system of rotational energy levels that are connected via an *a*-type transition, a *b*-type transition, and a *c*-type transition, along each of three rotational axes. Two of these transitions are typically in the GHz frequency range, and the third transition is on the order of 100 MHz. Following the notation in [30], the stimulated microwave transition (with frequency  $\sim 10$  GHz) is referred to as the “drive” transition and the stimulated RF transition (with frequency  $\sim 100$  MHz) is referred to as the “twist” transition. The molecular ensemble emits radiation coherently at the “listen” frequency, which is detected and plotted as a spectrum. Previous M3WM experiments were limited to assigned, known species, required prior knowledge of the transitions, and reported enantiomeric excess based on a single excitation scheme like the one shown in Figure 3.2(b)[63, 64, 65, 30, 2].

### 3.3.2 Experimental

#### Buffer gas cell design for chiral detection

Molecules flow continuously through a copper tube heated at 40° C into the buffer gas cell held at 5-7 K. A schematic of the apparatus is shown in Figure 3.2. Microwave horns are oriented with polarizations of  $\hat{x}$  and  $\hat{y}$  for excitation and detection, respectively. For this experiment, we used the microwave circuit for frequencies between 10-19 GHz. Two equally spaced copper electrodes are attached to the cell through 1” sapphire insulators to produce an electric field in  $\hat{z}$  direction. As in traditional M3WM, the “drive” and “listen” microwave horns are placed at 90°. For additional polarization control while maintaining the cold environment inside the cell, sapphire windows (4 inches diameter) were added on two sides of the cell and microwave absorber foam was placed on the outside, as shown in Figure 3.2(a). We observed that covering the inside of the buffer

gas cell with microwave absorber significantly increased the gas temperature.

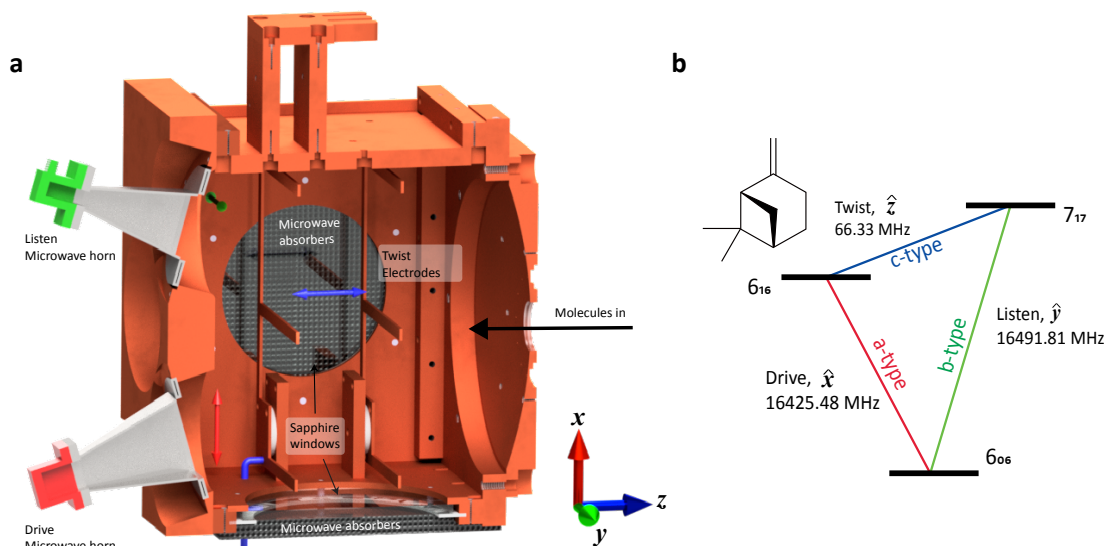


Figure 3.2: **Three-wave mixing spectra in a buffer gas cell** (a) Cut-away of the buffer gas cell used for acquiring three-wave mixing spectra. Arrows colored in red, blue, and green indicate the polarization of the drive, twist, and listen pulses. The back and bottom side of the cell have sapphire windows covered on the outside with microwave absorbers. (b) A typical M3WM excitation scheme for  $\beta$ -pinene. The three transitions are polarized perpendicular to one another and form a triangle that consists of an a-type, a b-type, and c-type transition.

The sample input consists of three main parts: a copper tube, a diaphragm valve, and a nipple loosely packed with glasswool. Depositing the sample on glasswool results in even evaporation and significantly reduces signal fluctuations over time, leading to highly repeatable measurements.

There were a few challenges to consider while designing a broadband three-wave mixing microwave experiment. In Table 3.1, I summarize the main requirements necessary for the broadband three-wave mixing experiment. To observe three-wave mixing signals with broadband fields, we had to increase experiment's reproducibility and sensitivity while maintaining the cold cryogenic environment. We also had to translate the polar-

ization and phase control needed from single frequency to the full microwave spectrum.

Table 3.1: Summary of requirements for the broadband microwave three-wave mixing experiment with the associated parts from the apparatus.

Requirements	
Higher sensitivity for broadband excitation	Sample Introduction, Electronics
Cell temperature to 5 K (base)	Vacuum, Cryogenics
Signal stability over experimental time	Sample introduction
Polarization control	Hardware
Phase control	Electronics, Timing

### Updating the sample introduction

Using broadband fields instead of resonant transitions for detection requires increased sensitivity and higher signal repeatability. Microwave three-wave mixing is a differential experiment, in which we do a measurement with phase  $\phi = 0$  and one with phase  $\phi = \pi$  and subtract the two measurements to get the value of enantiomeric excess. For this reason, shot-to-shot repeatability is important. The heated capillary method, used in previous experiments [17] resulted in random signal fluctuations that lead to false positive signals upon subtraction. The solution, which is further explained in the Experimental chapter, involved depositing the sample onto glaswool, which is a material with high surface area and high heat capacity.

### Data acquisition

All spectra were collected with similar conditions to demonstrate the applicability of the method to a wide variety of species without selective optimization. A  $4\mu\text{s}$  long 35MHz broadband microwave pulse is used as the “drive” pulse followed by  $2\mu\text{s}$  long RF twist pulse with a frequency chirp of 60-105 MHz. The “twist” pulse is overlapped with the drive pulse by  $1\mu\text{s}$ . The resultant coherent molecular signal (or “free induction decay” (FID)) following the double excitation is collected by a second orthogonally polarized horn

and digitized to form the spectra measured such as in figure 3.10(b). Three-wave mixing spectra combine a non-linear detection method (M3WM) with broadband excitation. Since we necessarily don't know transition dipole moments for unknown species, we operate at a pulse strength which is significantly underpowered for typical transitions. This results in typical signals that are 2-10 times weaker than typical M3WM signals under conditions optimized for maximum signal. These conditions were chosen to provide observable signal while not overdriving transitions, which would typically lead to larger false positives from non-chiral spectral lines.

For standard microwave experiments, the repetition rate and resolution of the experiment is a function of buffer gas density and chirp conditions. The FID lifetime is set by collisions inside the cell. FID lifetime varies dependent on molecular size and transition.

**Chemicals** Commercial (R)-(-)-1,2 -propanediol (96% purity) , anhydrous benzyl alcohol (99.8% purity), (1R)-(-)-myrtenal (98% purity), (1R)-(-)-fenchone (98% purity), (R)-(-)-carvone (98% purity), (-)- $\beta$ -pinene (99% purity) were purchased from Sigma-Aldrich.

### Elimination of unwanted signals

The most vital part of the experiment is to ensure that all non-zero signals stem from chiral species in enantiomeric excess. The distinction between the properties of real vs false non-chiral signals is presented in Figure 3.3. The real three-wave mixing signals stem for the three-level excitation schemes, have specific linear polarization and change sign with phase. The false signals are one photon rotational transitions, are emitted at all polarizations and do not change sign with phase. The 1D signals are at least 1000x stronger than the non-linear 3WM excitations.

We used three different methods to successfully eliminate all non-chiral signals: a) Polarization control, b) Fast and symmetric subtractions, c) an updated microwave circuit

design which rapidly and simultaneously changes the sign of the “drive” and “twist” pulses ensuring phase controllability and accurate reversibility for broadband chirps.

	Real signal	False signal
Transition type	3WM transition	1D transition
Polarization	Z polarized	X,Y polarized
Phase ( $\phi$ )	Changes sign with $\phi$	Does <b>NOT</b> Change sign with $\phi$
Intensity	Order of 0.001	Order of 1

Figure 3.3: Summary of the differences between real and false signals on the broadband microwave three-wave mixing experiment. Non-perfect polarization and phase conditions lead to false positive signals that survive cancellation that do not stem from chiral species in enantiomeric excess.

### Controlling Microwave Scattering

A significant issue we encountered during the initial troubleshooting for the broadband three-wave mixing is that rotational transitions which were not part of three-wave mixing triangles appeared at the spectra as “false” M3WM signals. We realized that they were potentially caused by microwave scattering from the cell walls.

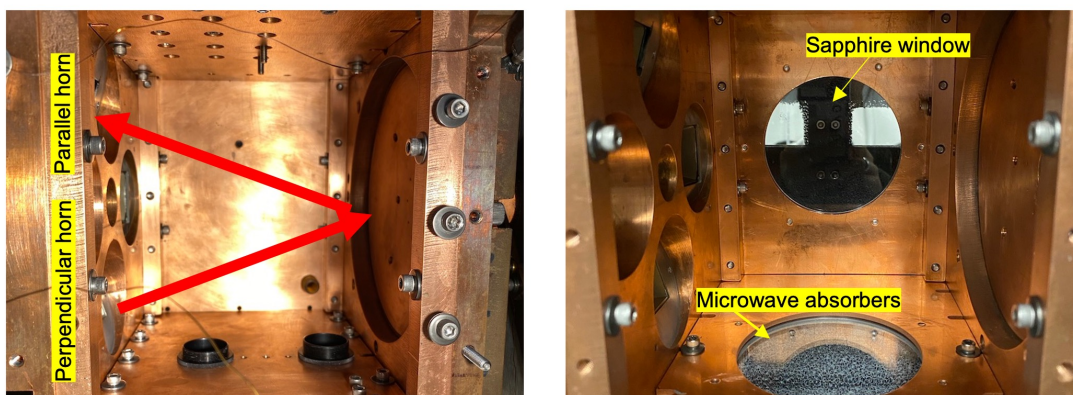


Figure 3.4: Controlling microwave scattering for polarization control. Red arrows show the ideal path of the microwaves inside the cell, from the drive horn to the spherical mirror and lastly to the detection horn. However, in reality, a significant portion of the microwaves travel all around the cell, scatter from the copper walls and can acquire random polarization that causes false positive signals to the broadband 3WM experiment. Sapphire windows were added on two sides of the cell and microwave absorber foam was placed on the outside to solve this issue while maintaining the cold environment inside the cell.

As shown on the left of Figure 3.4, polarization would be ideally preserved along the path of the microwaves from the drive horn to the spherical mirror to the listen horn which is placed at  $90^\circ$ . However, this is not the case. The microwaves travel all around the cell, scatter from the copper walls and then acquire random direction and polarization. In some cases, the polarization acquired is accidentally the right one and passes through the perpendicular listen horn. To test the theory, we placed microwave

absorbers (Laird Technologies, EMI Absorber PN 4106, RFRET 0.50”) inside the cell, as shown in Figure 3.5. These absorbers, which are similar to foam used for acoustic insulation, are widely used in the microwave community. The false positives significantly decreased after placing the absorbers. However, after a few months we realized that placing the absorbers inside the cell, increased the gas temperature. For additional polarization control while maintaining the cold environment inside the cell, sapphire windows (4 inches diameter) were added on two sides of the cell and microwave absorber foam was placed on the outside, as shown in on the right of Figure 3.4. This way, the microwaves that are not going through the preferred path and scatter all around the cell, end up passing through the window and getting absorbed.

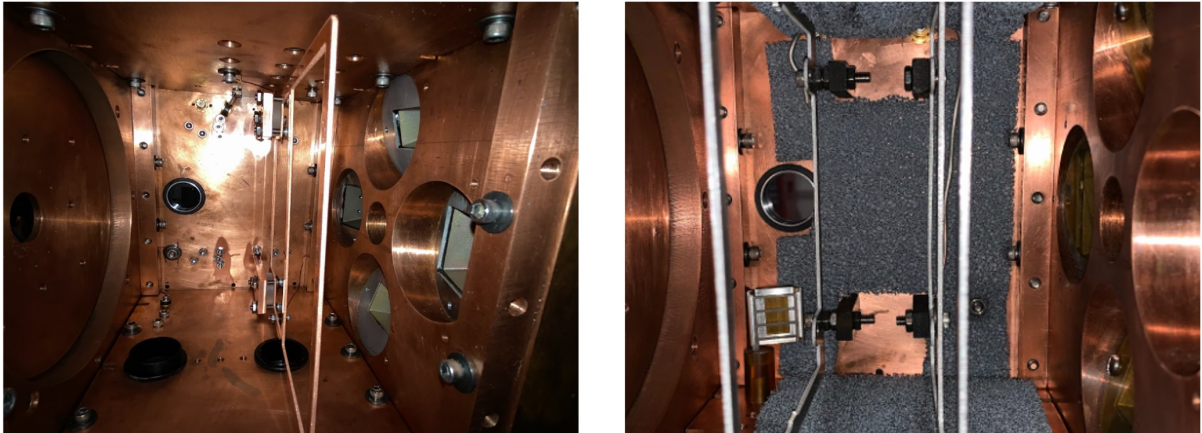


Figure 3.5: (Left) Image of the the buffer gas cell for chiral detection, showing the spherical mirror, the chiral electrode and the listen and drive horns place at opposite polarizations. (Right) Image of the the buffer gas cell for chiral detection covered with microwave absorbers for better broadband polarization control.

### Ensuring symmetric data acquisition

A key component of the success of non-linear microwave spectroscopy in a buffer gas cell is its high spectral acquisition velocity[17]. Each data point of the three-wave mixing spectrum consists of  $2.5 \times 10^6$  averages. The calm, controlled environment of the buffer gas cell enables careful subtractions between measurements of opposite twist phase every



few hundreds of  $\mu\text{s}$  for each data point of the spectrum.

This is important since we noticed that any “asymmetries” in the electronics or the data acquisition process can cause non-chiral signals to leak through. To solve this issue, we used a two-channel arbitrary waveform generator with very low time jitter (Siglent SDG6052X) to generate the “drive” and “twist” pulse. The timing window between each measurement and each experimental cycle was long enough ( $80 \mu\text{s}$ ) to prevent any signal cross-talk between measurements. A 9400 series Quantum Composer was also used to precisely control the timing between the two chirp pulses of each experimental cycle to ensure careful subtraction. It is not clear that a similar experiment could be conducted in an apparatus with pulsed valves where shot-to-shot variability is often significant and each measurement had to be taken with ms time resolution.

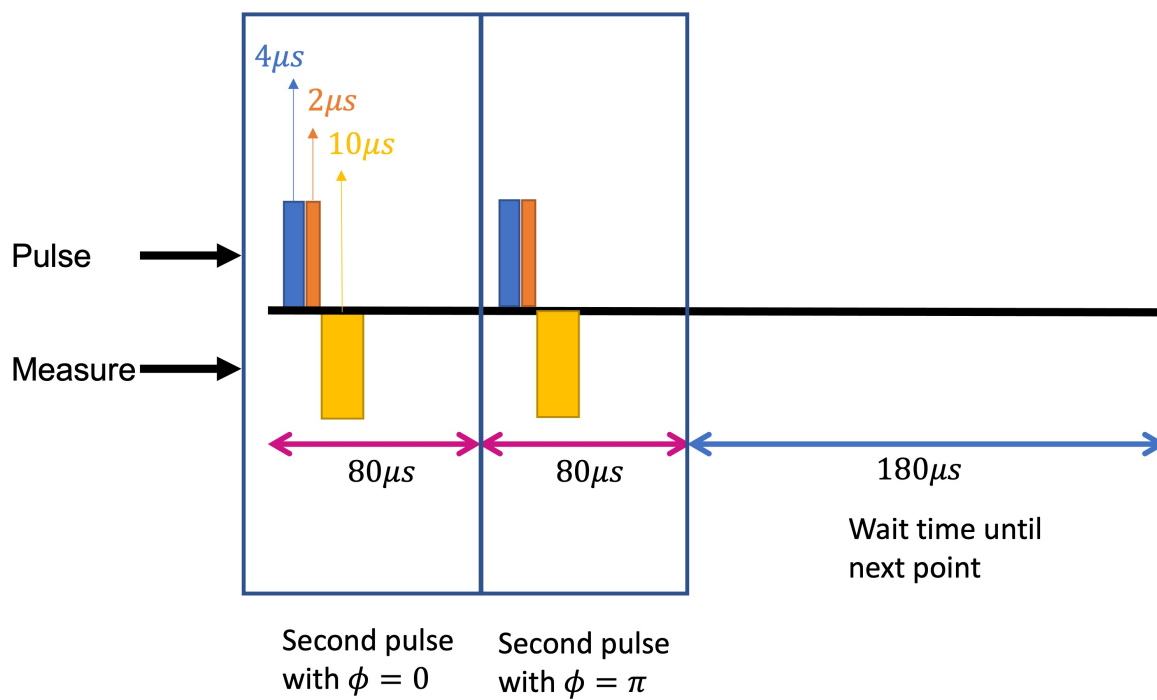


Figure 3.6: Schematic of the pulse sequence for the microwave three-wave mixing experiment. Microwave three-wave mixing is a differential experiment, in which we do a measurement with phase  $\phi = 0$  and one with phase  $\phi = \pi$  and subtract the two measurements to get the value of enantiomeric excess. While running the experiment, we realized it is extremely important for these two measurements to be identical in everything but the opposite phase to ensure only chiral signals survive the subtraction.

### Updated microwave electronics

The broadband three-wave mixing experiment uses our standard microwave circuit, described in the Experimental apparatus chapter, with a few additions for accommodating the clean and very careful subtraction necessary for the broadband phase control.

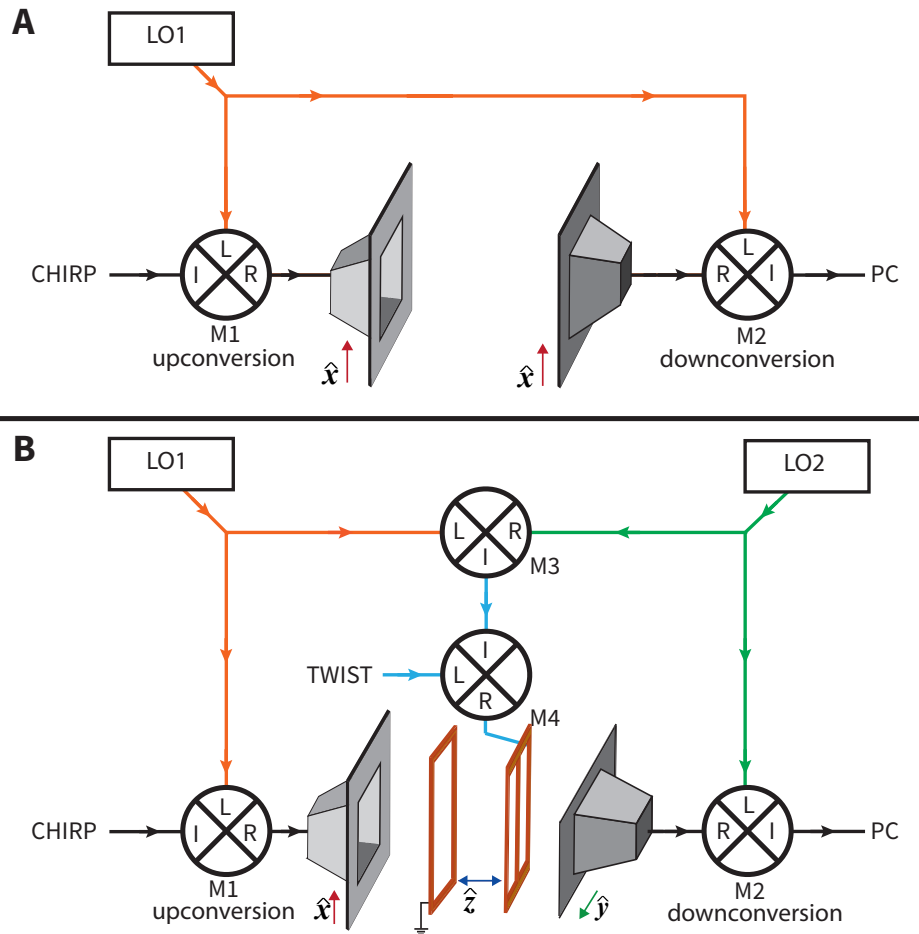


Figure 3.7: **Comparison of microwave circuit design.** (a) Schematic of the standard microwave circuit for microwave spectroscopy. (b) Schematic of the new circuit design for acquiring three-wave mixing spectra. The twist electrodes have been added for clarity. The upconversion and downconversion step are done with different local oscillators LO1 and LO2. Their beat note, 2 KHz in this work, is mixed with the twist to eliminate all non-M3WM signals.

An updated microwave circuit design ensures high phase coherence between the twist and drive pulses by mixing the twist pulse with the beat note between the upconversion

and downconversion steps. Figure 3.7 shows a comparison between the conventional circuit for microwave spectroscopy and the updated design. In the new design, two different local oscillators, LO1 and LO2, are used for the upconversion and the downconversion step and their beat frequency is mixed with the twist pulse. Specifically, mixer (M3) was added to the circuit taking LO1 and LO2 as inputs (the frequency difference between them was set to 2 KHz). This beat note is AC-coupled and amplified, then fed into mixer (M4) where it is combined with the twist pulse. The offset local oscillators cause any 1D (non chiral) signals to alternate phase with the 2 KHz beat note between the two local oscillators, and thus average to zero. The phase of the twist also alternates phase with the 2 KHz beat note between the two local oscillators, and so the M3WM signal survives and averages to a non zero value. This signal is recorded alternatively with a generated twist phase of  $\phi = 0$  and a twist phase of  $\phi = \pi$ , and signals from these two configurations are further subtracted before the spectrum is assembled. This final step removes small ( $< 30$  dB) bleedthrough of 1D signals resulting from imperfect mixing in the twist generation (M4). The new circuit design should improve the statistics of enantiomeric excess determination for single frequency M3WM experiments as well. The full electronics diagram with the updated microwave circuit integrated into our standard electronics circuit is shown in Figure 3.8.

The timings of the experiment are controlled by TTL pulses generated by the home-made programmable TTL pulse generator (Doyle Event Generator, DEG). For the broadband three-wave mixing circuit, the DEG and a 9400 series pulse generator Quantum Composer triggers the AWG that marks the beginning of the experiment.

A single trigger is used to generate the two consecutive “drive” chirp and “twist” RF pulses, as seen in blue and orange respectively in Figure 3.8. The enantiomeric excess measurement results from the careful subtraction of the two listen pulses, shown in yellow. The Quantum Composer sets the precise timing necessary between the two chirp pulses.

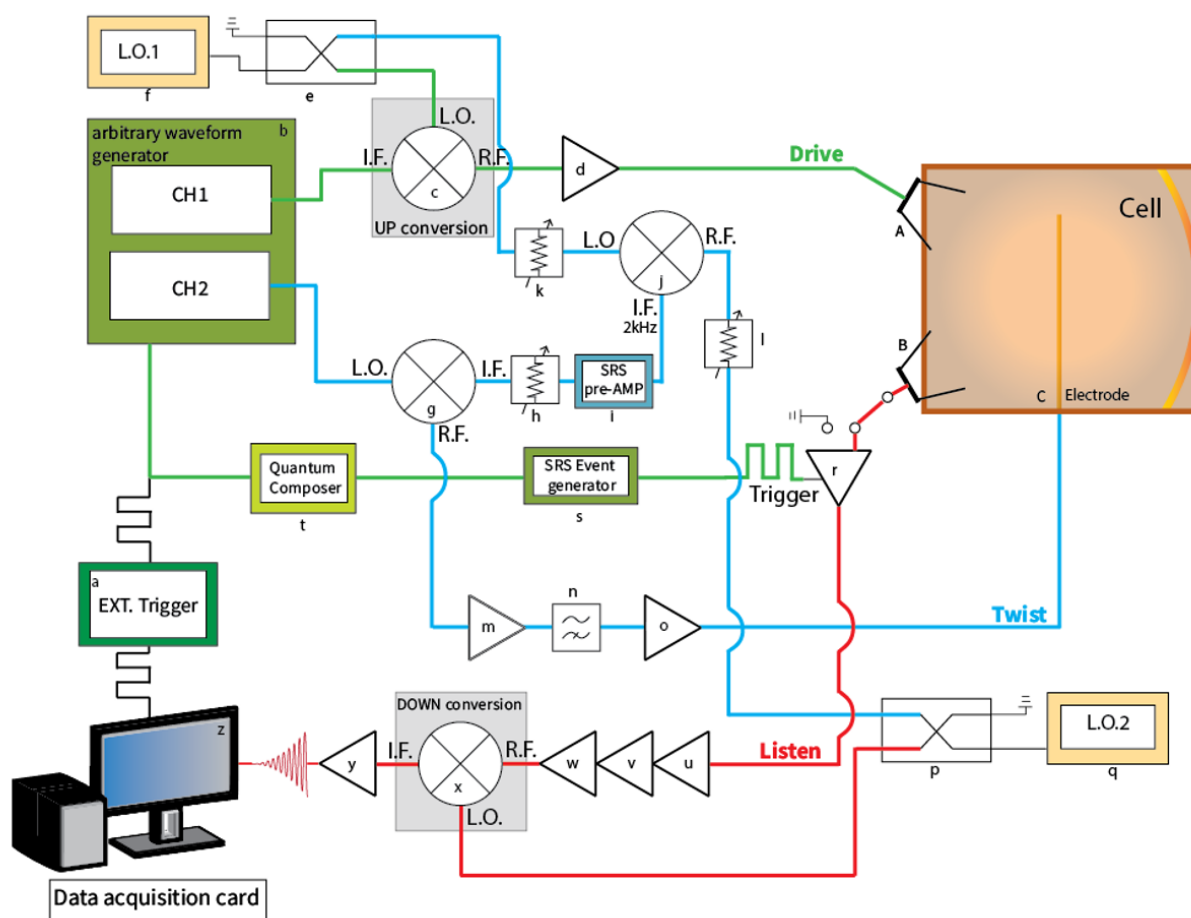


Figure 3.8: Schematic of the microwave electronics for the broadband three-wave mixing experiment.

The AWG then triggers the delay generator which in turn triggers the cryogenic amplifier and the protection switch. The U1084A data acquisition card is triggered separately by the DEG and collects the data.

### 3.3.3 Results

M3WM spectra are designed to detect species in enantiomeric excess. Figure 3.9 shows the comparison between the M3WM spectrum of an enantiopure sample of (R)-1,2-propanediol, shown in blue, plotted against the M3WM spectrum of a racemic sample of 1,2-propanediol, in red. The M3WM signal of enantiopure (R)-1,2-propanediol shows three noticeable signals corresponding to the lowest and the third-lowest in energy (0.88 kJ/mol) conformer[66]. In contrast, these three-wave mixing signals are not present in the spectrum of the racemic sample, in red, which has been shifted by -15 (a.u) on the y-axis for clarity. The details of the methods used to eliminate non-chiral signals are described in detail below.

Both spectra were recorded in the range between 14500-15100 MHz with a He buffer gas flow of 10 sccm, at 7 K. Each spectrum is assembled from 72 individual spectral segments, with 22.5 MHz local oscillator steps between them and acquired with a 35 MHz wide drive pulse and a twist pulse range of 80-105 MHz for a total integration time of 1 h. The detailed list of the M3WM transitions is given in Table 3.2.

Table 3.2: Three-wave mixing transitions for conformer 1 and conformer 3 of 1,2-propanediol.

Species	J'	K <sub>a</sub> '	K <sub>c</sub> '	J''	K <sub>a</sub> ''	K <sub>c</sub> ''	Frequency/MHz	Transition type
conf. 1	2	2	1	2	1	1	14795.79	c
	2	2	0	2	2	1	100.48	a
	2	2	0	2	1	1	14896.19	b
conf. 3	2	2	1	2	1	1	14797.7162	c
	2	2	0	2	2	1	95.1130	a
	2	2	0	2	1	1	14892.8290	b

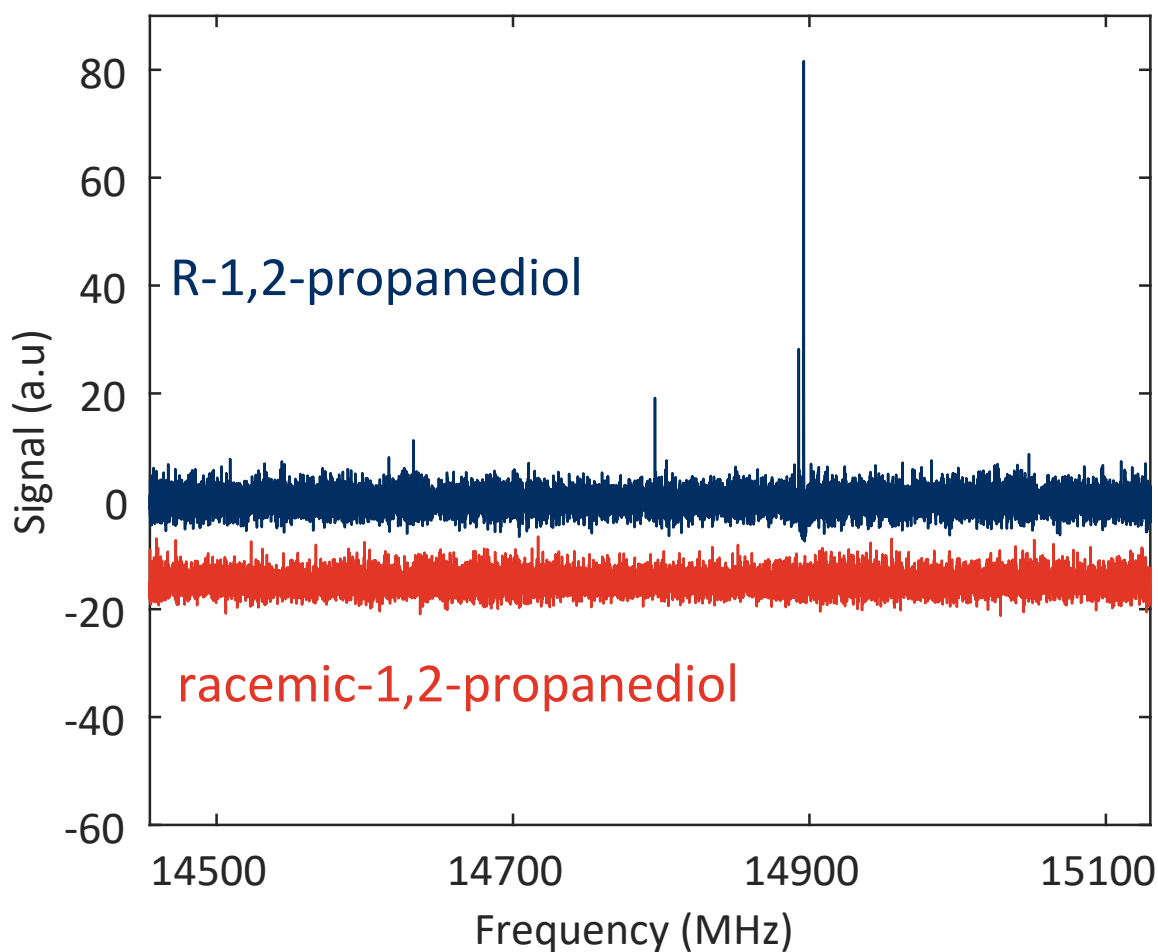


Figure 3.9: Three-wave mixing spectra of enantiopure vs racemic samples. (blue) Three-wave mixing spectrum of enantiopure (R)-1,2-propanediol. The three noticeable three-wave mixing signals belong to the two lowest energy conformers of 1,2-propanediol. (red) Three-wave mixing spectrum of racemic 1,2-propanediol. An offset of -15 (a.u) on the y-axis has been added to the racemic spectrum for clarity to show that no signal survives subtraction as expected.

**M3WM spectra of chiral and non-chiral species.** Figure 3.10 highlights the difference between microwave spectra and three-wave mixing spectra. Figure 3.10(a) shows the microwave spectrum of a mixture of a chiral molecule ((R)-myrtenal) and a non-chiral molecule (benzyl alcohol), compared to spectra of the individual components. In this frequency range, numerous rotational transitions from both species are present. Figure 3.10(b) shows the three-wave mixing spectrum of the same mixture, taken under similar conditions. Three-wave mixing spectra are non-zero only for chiral molecules in enantiomeric excess. Only transitions from enantiopure R-myrtanal are observed, as transitions from the non-chiral benzyl alcohol do not survive subtraction. It is noticeable that the transitions in the three-wave mixing spectrum are significantly fewer in number than the lines in the microwave spectrum of myrtenal, which is expected as not all transitions can participate in a M3WM chirality detection scheme, like the one showed in Figure 3.2(b).

Both spectra were recorded at 7 K, from 13000-18250 MHz and a He buffer gas flow of 10 sccm. The M3WM spectrum is assembled from 485 individual spectral segments, with 22.5 MHz local oscillator steps between them and acquired with a 35 MHz broadband drive pulse and an RF pulse with a range of 60-105 MHz for a total integration time of 3.5 h. The detailed list of the M3WM transitions is given in Table 3.3.



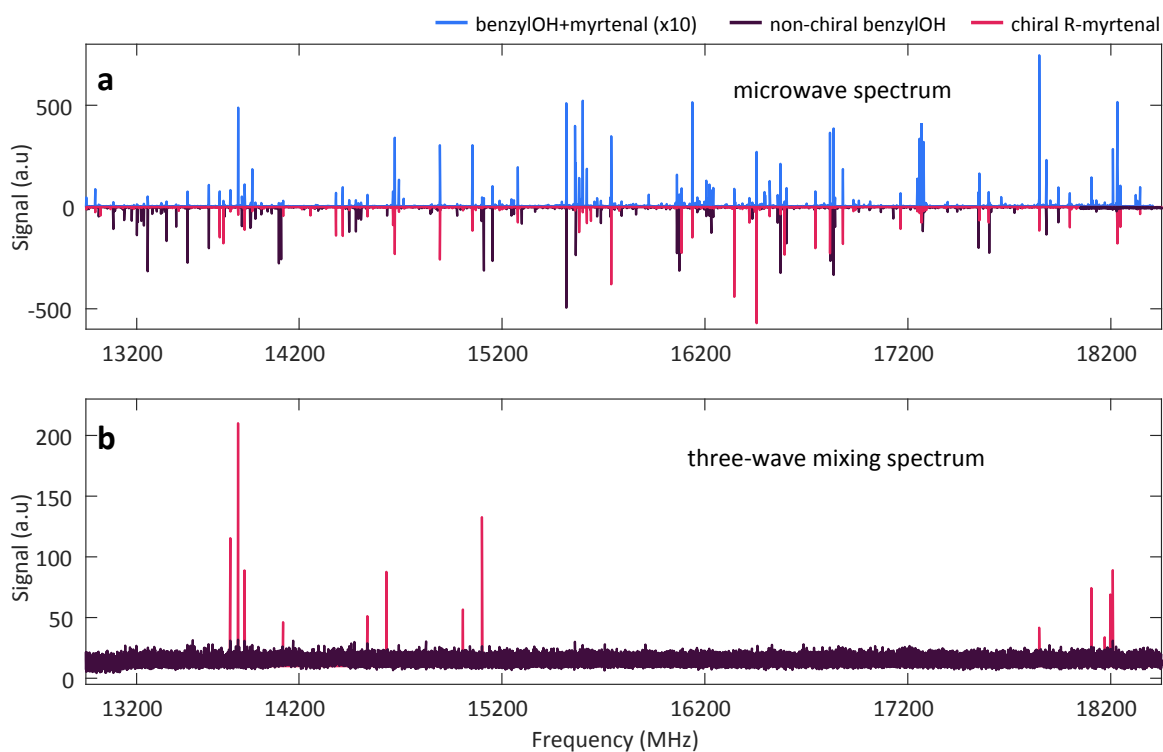


Figure 3.10: **Comparison between microwave spectra and three-wave mixing spectra.** (a) Top in light blue, microwave spectrum of the mixture of (R)-myrtenal (chiral) and benzyl alcohol (non-chiral). Amplitudes are multiplied by a factor of 10 for better visibility. Inverted, in dark purple and pink, the microwave spectra of the individual species, benzyl alcohol and myrtenal respectively. (b) Three-wave mixing spectrum of the mixture of (R)-myrtenal and benzyl alcohol. Each transition belongs to a chiral species in enantiomeric excess. In pink, only transitions from enantiopure (R)-myrtenal survive cancellation.

Table 3.3: Three-wave mixing transitions, corresponding to Figure 3.10

	$J'$	$K_a'$	$K_c'$	$J''$	$K_a''$	$K_c''$	Frequency/MHz	Transition type
1	8	0	8	7	1	7	13661.859	b
	7	1	7	7	0	7	69.641	c
	8	0	8	7	0	7	13731.500	a
2	8	0	8	7	1	7	13661.858	b
	8	1	8	8	0	8	38.086	c
	8	1	8	7	1	7	13699.944	a
3	10	3	7	9	4	5	13833.895	c
	9	4	5	9	4	6	88.331	a
	10	3	7	9	4	6	13921.807	b
4	6	3	4	5	2	3	14337.090	b
	6	3	3	6	3	4	93.689	a
	6	3	3	5	2	3	14430.779	c
5	6	3	3	5	2	4	14901.544	b
	6	3	3	6	3	4	93.669	a
	6	3	4	5	2	4	14807.855	c
6	10	1	9	9	2	8	17398.517	b
	10	2	9	10	1	9	248.754	c
	10	2	9	9	2	8	17647.271	a
7	7	4	4	6	3	3	17904.473	b
	6	3	3	6	3	4	93.628	a
	7	4	4	6	3	4	17998.102	c
8	7	4	3	6	3	4	18010.125	b
	6	3	3	6	3	4	93.628	a
	7	4	3	6	3	3	17916.497	c
9	13	4	9	12	5	7	17895.985	c
	12	5	7	12	5	8	74.228	a
	13	4	9	12	5	8	17970.215	b

**M3WM spectrum of multi-component mixtures.** Three-wave mixing spectra can provide useful chirality information of multi-component mixtures without any prior chemical processing, separation, or spectral assignment. This capability is relevant to asymmetric synthesis and chemical analysis of complex real life samples. In Figure 3.11, we show the three-wave mixing spectrum for a mixture of terpenes. Terpenes are naturally occurring chiral building blocks that have been used for decades as starting materials for the synthesis of natural products and active ingredients in pharmaceuticals, due to their abundance and low cost[67, 68, 69].

All transitions in Figure 3.11 belong to enantiopure (-)- $\beta$ -pinene, (R)-fenchone, and (R)-carvone. The inset zooms into the transition around 16492 MHz which consists of two separate M3WM signals: a  $\beta$ -pinene M3WM signal at 16491.7 MHz and a second one from fenchone at 16492.5 MHz. For such mixtures, even polarimetry measurements can be inconclusive, as the sum of the angles for multiple components can cancel each other out. Equal amounts of neat (-)- $\beta$ -pinene, (S)-carvone, and (R)-fenchone would have a total specific rotation  $[\alpha]_{20}^D$  of +7 the sum of each component, which carries significantly less chemical information than a spectrum. On the contrary, the three-wave mixing spectrum of such mixture, as seen in Figure 3.11, shows distinct transitions for each separate species. If microwave spectra of the species are available, even if unassigned, then no additional measurements are required to determine the exact identity of the species. For readily available chiral building blocks like the ones used here, species were easily and accurately identified. The spectrum of the mixture was recorded in the range between 16200-18000 MHz with a He buffer gas flow of 10 sccm, at 7 K. Each of the 150 spectral segments was recorded with a drive pulse of 35 MHz bandwidth. The total acquisition time was 2 h. Two separate twist ranges of 65-85MHz and 85-105MHz were used for increased RF power to assure transitions of less polar species are sufficiently driven. The detailed list of the M3WM transitions is given below.

Table 3.4: hree-wave mixing transitions for mixture of terpenes, corresponding to Figure 3.11

Species	J'	K <sub>a</sub> '	K <sub>c</sub> '	J''	K <sub>a</sub> ''	K <sub>c</sub> ''	Frequency/MHz	Transition type
<i>β</i> -pinene	7	1	7	6	0	6	16491.73	b
	6	1	6	6	0	6	66.310	c
	7	1	7	6	1	6	16425.42	a
<i>β</i> -pinene	7	0	7	6	1	6	16392.042	b
	6	1	6	6	0	6	66.26	c
	7	0	7	6	0	6	16458.30	a
fenchone	8	2	7	7	1	6	16492.52	b
	8	2	7	8	1	7	26.660	c
	8	1	7	7	1	6	16465.87	a
carvone	15	1	15	14	0	14	17856.79	b
	15	1	15	15	0	15	90.71	c
	15	0	15	14	0	14	17766.08	a
carvone	15	0	15	14	1	14	17641.1531	b
	15	1	15	15	0	15	90.4015	c
	15	1	15	14	1	14	17731.5545	a

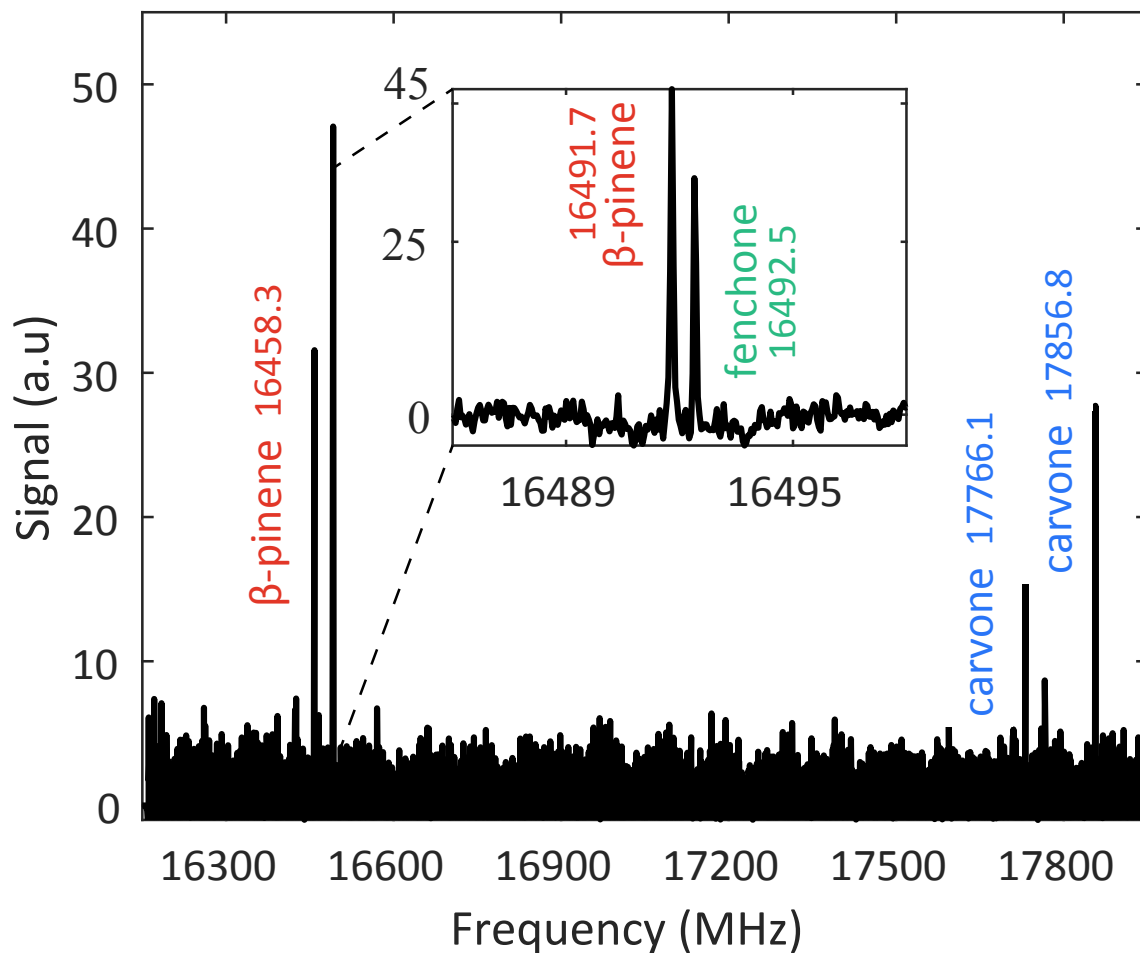


Figure 3.11: Enantiopure (-)-pinene, (R)-fenchone, and (R)-carvone were identified within the mixture with a narrow scan between 16,300–18,000 MHz and two twist ranges from 65 to 85 MHz and 85 to 105 MHz. The inset zooms into the transition around 16492 MHz which consists of two M3WM signals: a -pinene M3WM signal at 16,491.7 MHz and one from fenchone at 16492.5 MHz.

### 3.3.4 Discussion

Three-wave mixing spectra can be recorded for any sample that contains molecules that are vaporizable and have non-zero electric dipole moments across all rotational axes. Microwave spectroscopy is mixture, solvent, isomer, and isotopologue compatible meaning that no chemical processing is necessary prior to analysis[6, 3, 4]. Figures 3.12 show a variety of molecules that display three-wave mixing spectra.

Chiral information can be extracted on-the-spot as only transitions from species that are chiral and in enantiomeric excess survive cancellation. As shown in Figures 3.10 and 3.9 signals from racemic samples or non-chiral molecules average to zero.

A promising application would be the direct chiral detection of the raw constituents of one pot asymmetric synthesis reactions, similar to ones by [70, 71]. Inside this flask, there are: reactants, solvents, products, by-products, and catalysts. Even though large polyatomic molecules like catalysts can't be easily seen, a comparison between the three-wave mixing spectrum before and after the reaction can identify any new chiral products, in enantiomeric excess produced, as in figure 3.11. Even molecules very similar in structure like terpenes isomers can be unambiguously identified with microwave spectroscopy. Since any separation or purification of the sample is unnecessary for analysis, our method can act as a tool for the general search of chiral catalysts. Unlike polarimetry, once the spectra are acquired the exact transitions can be used to unambiguously identify the species produced.

Microwave three-wave mixing works best for strongly polar molecules as the matrix elements for rotational transitions depend linearly on the magnitude of the dipole moments across the A, B, and C rotational axes[30]. In this work, beta-pinene with dipole moments of  $|\mu_a| = 0.43$ ,  $|\mu_b| = 0.58$ ,  $|\mu_c| = 0.11$  Debye was the least polar molecule under study [72]. Even though enantiopure samples were used for all experiments, three-wave mixing

signals scale linearly with enantiomeric excess (ee), thus signals from species of enantiopurity above 30 percent should be sufficiently above noise level to be detected. This could be improved with straightforward electronics updates. The determination of the exact percentage of enantiomeric excess and absolute configuration from microwave three-wave mixing spectra could be performed similarly to other M3WM experiments[63] given that there are available samples of known enantiomeric excess for calibration. Without such a calibration sample, the method cannot determine the absolute configuration - that is, whether *R*- or *S*- is in excess - as this relies on absolute knowledge of the dipole moments for each enantiomer, which is not defined for an unknown sample.[5]

An important parameter of the experiment is the frequency range of the twist pulse. We know from experience that most molecules display transitions between 60-110 MHz so we chose to use this range for the “twist” pulse during all data acquisition. However, for a more complete analysis of unknown samples additional frequency ranges can be easily explored. We have encountered no chiral molecule without three-wave mixing transitions with a twist between 25-250 MHz, which is the range of our current RF amplifier: our method is thus expected to detect any common vaporizable small chiral molecule. Additionally, as molecules grow in size, their microwave spectra get more congested and they should typically exhibit richer M3WM spectra.

Three-wave mixing spectra of unknown samples are useful as preliminary scans for chiral species in enantiomeric excess. Given that the method does not require prior chemical knowledge of the sample for determination of the rotational transitions or any optimization for probing different species (as shown in Figure 4), it can be directly applied to unknown samples. However, further analysis is needed for identifying each species of an unknown mixture. To determine the identity of the species one needs to search for the transitions in available spectral libraries like splatalogue[73], CDMS[74], or published experimental and calculated spectra. For more exotic species, it is possible to perform

the experiment in reverse, going from broadband fields to resonant to identify all transitions of the three-level system. Then, double resonance experiments similar to the one performed by M.A.M Drumel et al.[75] can be conducted to determine the rotational constants and the structure of the unidentified species.

In summary, we have introduced a generalized version of M3WM that includes the capability of acquiring microwave three-wave mixing spectra in unassigned samples. M3WM spectra can provide direct evidence on enantiomeric excess on-the-spot without the need of prior spectral assignment via the combination of broadband excitation and careful signal cancellation. Our new method can be applied to particularly hard-to-analyze samples like unknown multi-component mixtures and hard-to-assign species and provides new methods for ultrasensitive phase-coherent spectroscopic detection.

Three-wave mixing spectra combine a non-linear detection method (M3WM) with broadband excitation. Even though we aimed for the highest sensitivity possible, we had to run quite underpowered given the broad fields, while keeping excitation via higher order harmonics in our chirp upconversion circuit minimal for better cancellation. Adding more chirp power (using amplifiers) increased the signal of enantiopure species but introduced non-linear components to the chirp that led to non-M3WM signals surviving cancellation. On the other hand, increasing the duration of the chirp was a cleaner way to increase the signal. Another factor that limited the overall sensitivity was that we did not want to introduce any asymmetries in the data acquisition process which limited our data acquisition velocity. Thus, optimal conditions for broadband M3WM involved the combination of controllability over phase and polarization with long and linear chirps.



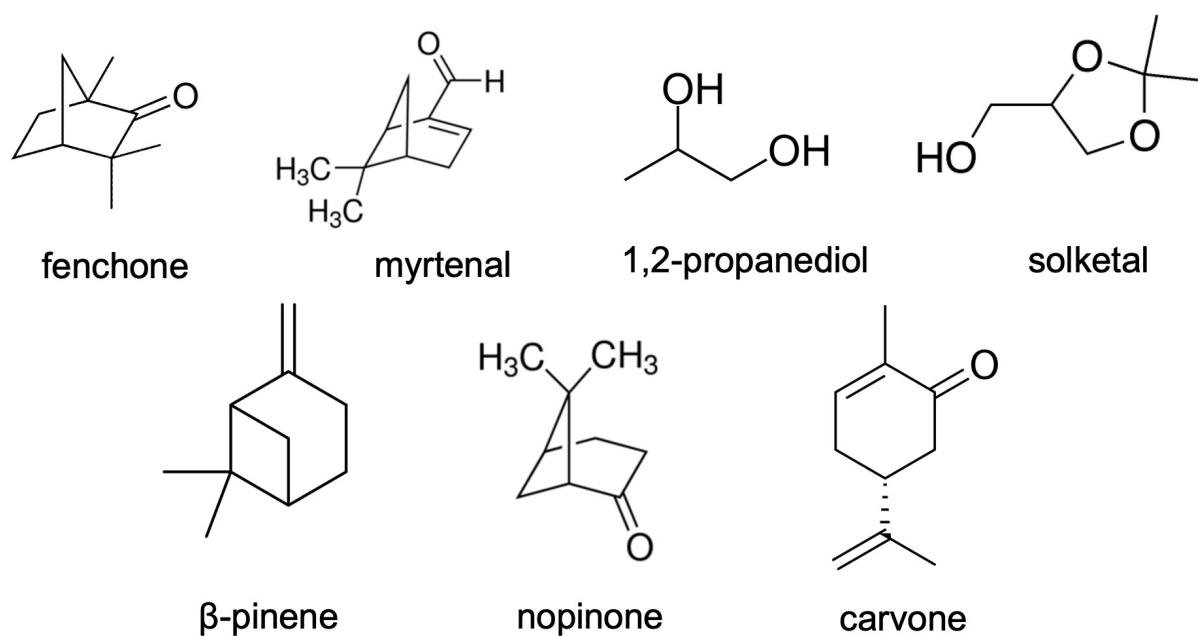


Figure 3.12: List of molecules for which we have demonstrated broadband three-wave mixing.

# Chapter 4

## Stray electric fields in the buffer gas cell

This chapter will describe the effects of stray electric fields, observed in the buffer gas cell apparatus. These fields pose significant challenges to signal optimization and troubleshooting since they introduce DC Stark splittings in our rotational transitions. I describe the experimental conditions under which these effects were observed, present diagnostic data and introduce the “Spontelectric effect” which is our current best hypothesis on the underlying cause of such effects. These electric fields, caused by a combination of molecular ice and wall effects compromise current resolution and sensitivity of the instrument, directly limiting the capabilities of future chiral detection and precision experiments.

## 4.1 Observation of stray electric fields in the buffer gas cell

The presence of stray electric fields in the buffer gas cell became most evident while conducting the microwave three-wave mixing (M3WM) experiments, discussed in the previous chapter. During optimization of the transitions that participated in the three-level excitation schemes, we noticed line splittings from the Stark effect that posed significant challenges to signal optimization and troubleshooting of the weak chiral signals.

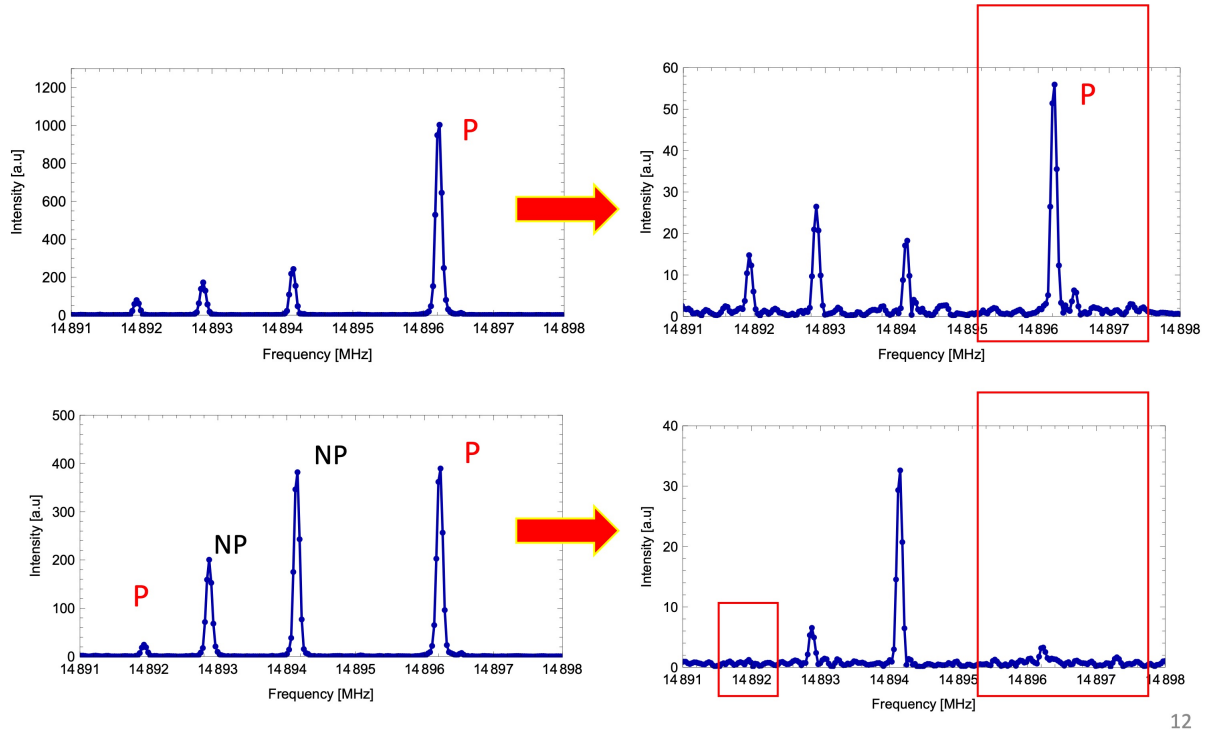


Figure 4.1: Signal progression over time, highlighting the effects of stray electric fields in the buffer gas cell. Polarizable and non-polarizable transitions are marked as P and NP, respectively. The red arrows point at the same plots at times  $t$ . Polarizable lines are split or completely obliterated due to DC Stark. This posed great challenges in experimental troubleshooting and signal optimization.

As seen in Figure 4.1, while optimizing the 14896.22 MHz line (one of the lines of the M3WM excitation scheme for 1,2 propanediol), we would observe shortened FID ringdowns indicative of line broadening resulting in an overall decrease of the signal amplitude at the center frequency. The rest of the three lines belong to different 1,2 propanediol conformers. We mark the chiral lines as P, from Polarizable, as they are part of three-level excitation schemes used for M3WM. The rest of the lines that cannot form M3WM schemes, we mark as NP, from Non-Polarizable. We noticed that the M3WM transitions appeared to be more sensitive to the effect than the rest of the lines, which hinted the presence of electric fields and the DC Stark effect. The fields would get worse over a few hours and were repeatedly observed between runs. No difference was observed between different buffer gas flows and the effect was present for various species including 1,2 propanediol, fenchone,  $\alpha$ - and  $\beta$ -pinene, carvone and solketal.

According to the Stark effect, a particle carrying an electric dipole moment will experience a splitting of its energy levels when subjected to an external electric field, described by the Stark term, where  $E$  denotes the external electric fields and  $\mu_{el}$  is the electric dipole moment:

$$H_{stark} = -\vec{E}\vec{\mu}_{el} \quad (4.1)$$

Solving equation 4.1 for the 2nd order energy correction gives the perturbative energy term 4.2, for energy states  $m$  and  $n$ :

$$E_n^{(2)} = \sum_{m \neq n} \frac{|\langle m^0 | H_{stark} | n^0 \rangle|^2}{E_n^{(0)} - E_m^{(0)}} \quad (4.2)$$

Based on 4.2, M3WM transitions are indeed more sensitive to the DC Stark effect since two of the three energy levels are connected via an RF transition[30], thus they become more susceptible than transitions between levels with energy separations at the

microwave regime.

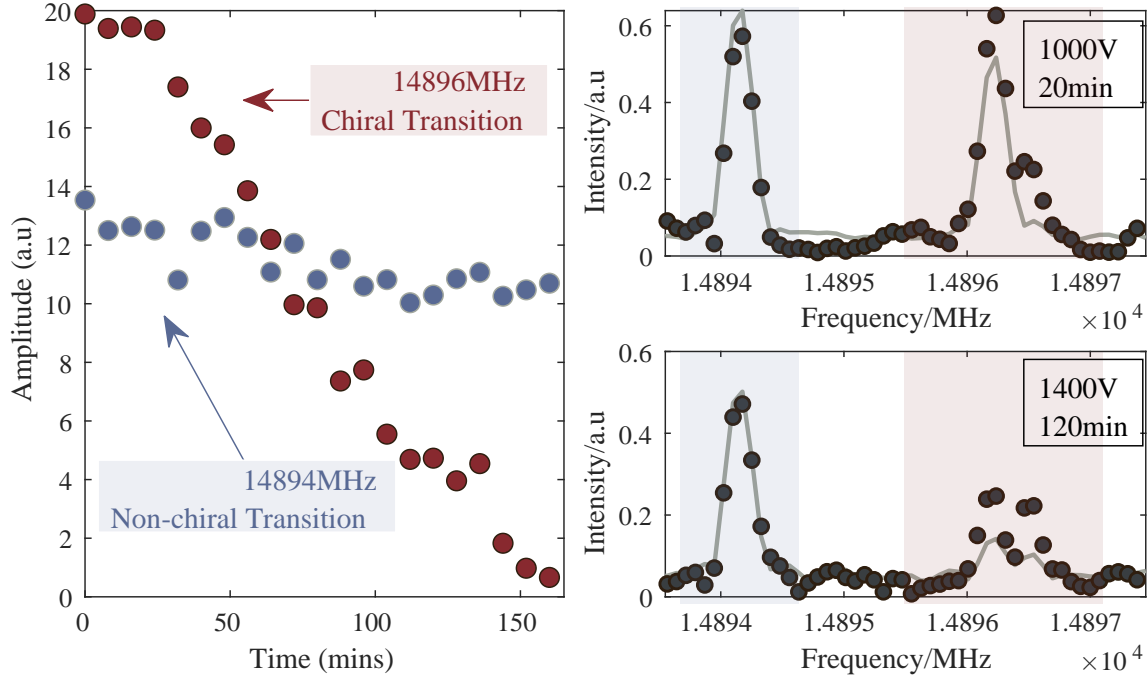


Figure 4.2: (left) Signal time progression of center frequency amplitude for a M3WM chiral transition (red) and a non-chiral one (blue). (right) The chiral (red square) and non-chiral transition (blue square) in the frequency domain at early times (top) and later times (bottom). The red transition is significantly more affected by the stray fields than the blue. The DC Stark shifts are fitted to 1000 V/m and 1400 V/m DC Stark shifts shown in grey, for the data points at 20 min and 120 mins of experimental time. The shifts were calculated using the PGOPHER package. The labels are associated with transitions that could or could not be used in a M3WM chiral detection scheme and not to an actual chiral detection measurement.

Figure 4.2 highlights the different observed effects of stray electric fields when comparing non-chiral and chiral (M3WM) rotational transitions. The labels are associated with transitions that could or could not be used in a M3WM chiral detection scheme (and not to a chiral detection measurement). On the left, we see the time progression of center frequency amplitude for both lines. Chiral transition (red) amplitude decreases with time, while the non-chiral one (blue) remains comparatively stable. To understand this, we look at the frequency domain of each transition at early times (20 minutes) and later times (120 mins). The chiral line is broadened and split by DC Stark, while the

non-chiral amplitude remains constant. We fit the splitting to DC Stark shifts at different electric field values generated by PGOPHER microwave software simulation package. A field of 1000 V/m and 1400 V/m is the best fit and shown in grey. Figure 4.3 shows the DC Stark splitting from 1400 V/m, from data with higher signal-to-noise.

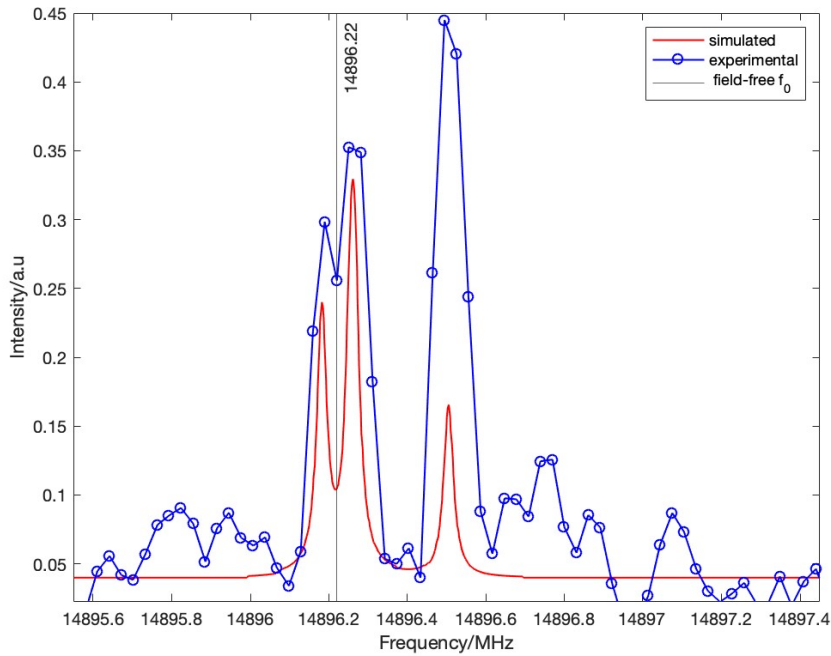


Figure 4.3: Comparison of experimental data of a 1,2-propanediol chiral line with simulated DC Stark shift equal to 1400 V/m. The field-free center frequency  $f_0$  is at 14896.22 MHz

**Finding the source: Ferroelectric Ice**

Molecules enter the cell in the gas phase, thermalize via collisions with the cold gas and then diffuse into the cell walls and freeze. After a few hours of runtime, molecular ice covers the walls as well as the inner peripheral of the aperture, as illustrated by the CAD rendering of the cell in Figure 4.4. In some rare cases, as seen on the experimental images of Figure 4.4, thick ice would form on the sapphire window located at the cell's side plate.

For the past year, we have made some progress towards understanding the source of stray electric fields and experimenting with different ways to eliminate them. By carefully studying which parameters of the experiment are the most sensitive to the stray electric fields, we believe that the electric fields main source are the molecules. Without flowing more molecules into the cell, the fields do not deteriorate over time.

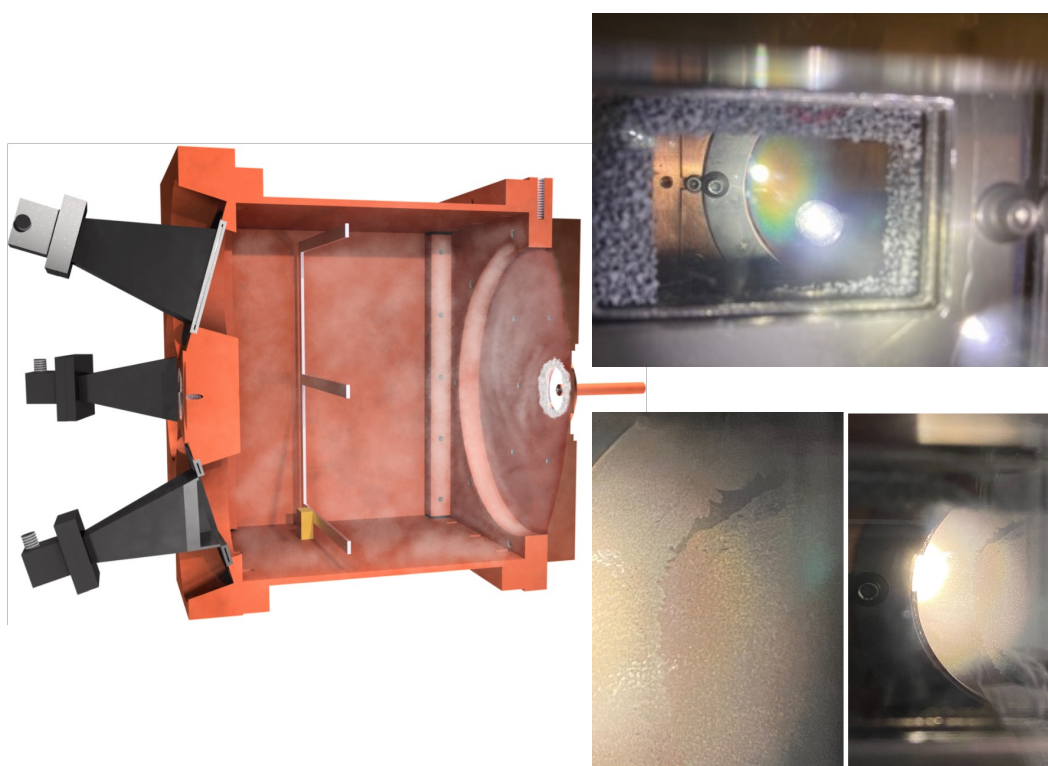


Figure 4.4: (left) CAD image of the buffer gas cell covered in molecular ice.(right) Experimental images of ice on cell's windows.



## 4.2 Spontelectrics: Effects of spontaneous polarization of cryo-deposited films in the buffer gas cell

There is extensive literature on solid ice films of polar molecules such as water that display ferroelectric behavior [76, 77]. One of the most famous examples of cryogenic ferroelectric ice is the case of Ice XI, one of the 17 solid phases of water. There have been numerous studies connecting electric fields measured on Ice XI substrates and planet formation [78, 79, 80]. There are also studies of Ice XI deposited on metal surfaces showing that orientationally disordered crystalline films are formed that can create large depolarization fields across the film [81, 82]. These studies lead me into considering the “Spontelectric Effect”, which we believe explains the cause of stray electric fields in the buffer gas cell.

According to the “Spontelectric Effect”, when polyatomic molecules are deposited on low temperature surfaces, they can freeze in different orientations that can produce a net macroscopic polarization, which can be the source of electric fields. This effect was first discovered by Prof. Field, from Aarhus University in Denmark in 2009. The spontelectric effect can also be summarized as the result of polar cold molecular deposition on cold surfaces creating a surface potential which is a function of the thickness of the film and the deposition temperature. The magnitude of the electric fields increase as the deposition temperature decreases and when the number of monolayers increases. Spontelectrics is an effect of dipole ordering in the bulk rather than a surface-adsorbate effect [83, 84].

The main relevant observed properties of spontelectrics are summarized below. The stray electric fields in the buffer gas cell seem to share very similar behavior to these properties:

- Gas-phase deposition of a spontelectric material on a metal surface would spontaneously produce a potential across the surface of the film.
- The potential can be either negative or positive depending on the material properties of the film.
- The field scales linearly with the thickness of the film.
- Field magnitude depends strongly on deposition temperature. At certain high temperatures, the spontelectric effect is not observed.
- The spontelectric effect can be stable over a period of a few hours.

Spontelectric materials display similarities with ferroelectric ones such as polarization effects created by dipole ordering and a Curie point. By analogy with ferromagnetism, the critical temperature at which the dipole alignment disappears is referred to as the Curie point. For example, the Curie point for isoprene deposited at 40K is 82 K. Typically, minimum thickness of 50-100 monolayers are needed for this effect to be observable. The discriminating factor is the lack of thermal hysteresis for spontelectrics. Cooling below the Curie point does not re-introduce the potential as seen in ferroelectrics, but above the Curie point the fields disappear. Spontelectric materials that have been observed so far include: nitrous oxide ( $\text{N}_2\text{O}$ ), carbon monoxide ( $\text{CO}$ ), toluene, freon 11-13, 2,5-dihydrofuran, ethyl formate, methyl formate, isoprene, isopentane, propane and saturated monohydroxy alcohols. [85, 83, 76]

### The solution

Our current most effective method for temporary field annihilation utilizes a laser as a source of ions and electrons. When a focused beam of a 532 nm nanosecond laser is shone upon a spot on any copper metal surface of the cell, we observe a temporary damping of the stray fields, as seen in Figure 4.5. If the laser beam hits the surface consistently at a repetition rate of 0.8-1 Hz, we can cancel out part of the existent fields and delay the effect for an extended period of time. We believe that the laser acts similarly to an anti-static gun producing ions or electrons that coat the ice temporarily. Some spontelectric experiments have also observed that irradiating the surface with an electron beam of opposite voltage polarity or significantly higher electron flux can remove the spontelectric field.[84]

At this point, we have preliminary evidence showing that the electric fields have negative polarity but it is still unclear which particles help with field cancellation. A more robust and simpler solution is definitely needed for the spectrometer to be fit for high-resolution precision experiments and the chirality detection of larger, more polarizable molecules.

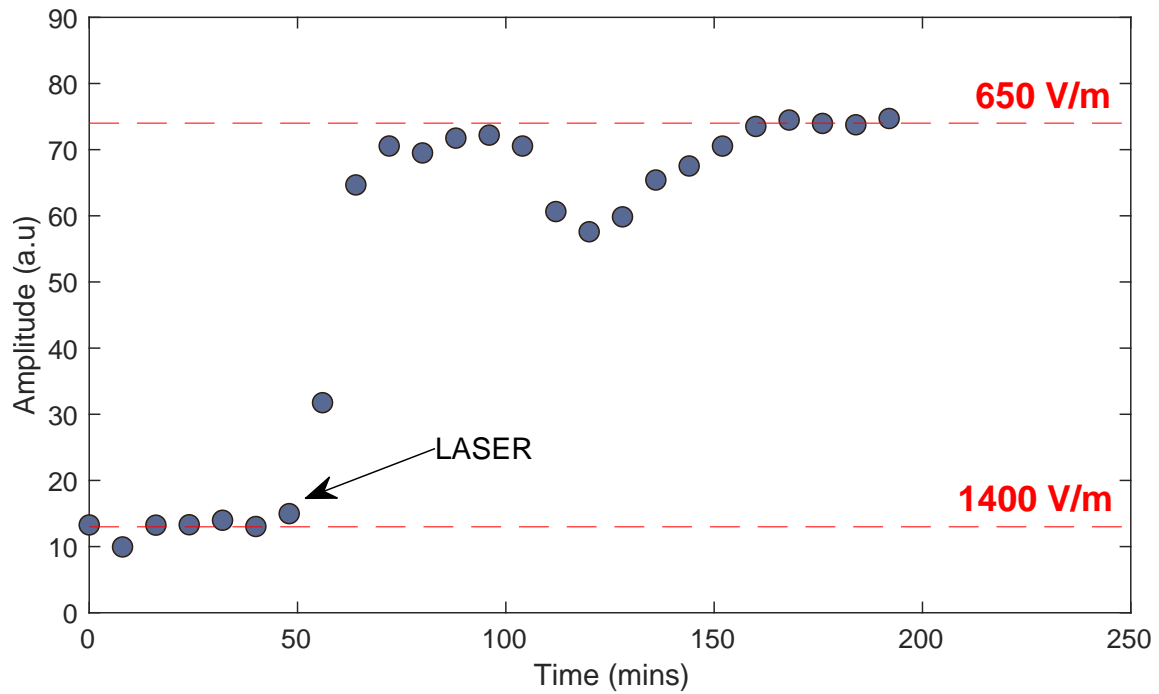


Figure 4.5: Signal amplitude over time, highlighting the effects of laser irradiation for the annihilation of stray-electric fields. A few pulses of a 532 nm focused laser on the metal surface of the cell cancel out part of the electric fields. By fitting the spectrum of the data points between 0-50 mins of runtime and after laser irradiation to simulated DC Stark shifts, we calculate that laser annihilates about 50 percent of the induced fields.

### 4.3 Discussion and current solutions

One of the challenges towards conclusively proving that spontelectric fields are indeed the source for the effect observed in the buffer gas cell is the different size and nature between the buffer gas cell apparatus experiments and the electron beam apparatus experiments used in Aarhus University. Field et al. use synchrotron radiation (h ASTRID) that enters a photoionisation source containing argon at a pressure of typically  $10^{-4}$  mbar. Photoelectrons are irradiated onto the condensed solid films at temperatures of 38K and above. The electron beam current is approximately 200 fA. The surfaces are prepared under ultra high vacuum conditions. [84, 86]

As described in detail in this thesis, buffer gas experiments are not operating at ultra high vacuum (UHV) and do not involve clean surfaces. The three-dimensional non-flat setup is also not designed for controlled chemical deposition. We believe that the electric field in the cell is not-uniform, which makes its characterization and complete elimination challenging. Microwave spectroscopy can be used as a probe of DC-Stark which is an indirect method of electric field determination, however it is not as straightforward as a direct voltage measurement.

Current and future efforts are focused on discovering a better solution for permanent field cancellation. A promising idea inspired by other spontelectric experiments in the literature is the dilution of the molecular parent gas with a non-dipolar gas to disrupt the cold temperature metal deposition. Some promising candidates are nitrous oxide ( $N_2O$ ), which has been extensively studied for its spontelectric effect and creates a positive surface potential, carbon dioxide ( $CO_2$ ) or a noble gas such as Argon.[87] The gas can be introduced before the molecules and form a non-polar ice blanket or as a mixture. Another direction would be taking advantage of the Curie point and phase transition of different gases in the mixture. Unfortunately, the Curie point for most small polar

molecules is above 80 K, which is a significant heatload for an active cryogenic experiment. An interesting way around it, would be taking advantage of the phase transition of a gas like methane that occurs at 20K [88]. By mixing our polar mixture with methane, we could potentially alter the dipole orientation of the solid ice.

## Chapter 5

# Studying parity-violation effects in chiral molecules with microwave spectroscopy

This chapter describes in more detail, the work in reference, “ Sub-Hz differential rotational spectroscopy of enantiomers (2021). L.Satterthwaite, **G. Koumarianou**, D. Sorensen, D. Patterson. *Symmetry*, 14(1), 28.”

I discuss our results in demonstrating for the first time differential precision microwave spectroscopy towards studying parity violation effects in chiral molecules. The experiment was conducted in a cryogenic buffer gas cell coupled to a microwave Fabry-Perot resonator. Differential frequency measurements were taken between alternating samples of (R)-1,2-propanediol and (S)-1,2-propanediol near 15 GHz.

Our results allowed us to probe subtle molecular structural effects and systematics at the  $10^{-10}$  level. Using a buffer gas cell apparatus produces much more controlled and repeatable spectroscopic data compared to standard pulsed-jet molecular beam methods. The dominant systematic effects at this level are discussed along with future improvements

and considerations for choosing molecular candidates.

## 5.1 Measuring parity violation effects in chiral molecules

### 5.1.1 Background

The electroweak nuclear force, one of the fundamental forces, is chiral and it can manifest as parity violating effects in atoms and molecules because of the exchange of virtual  $Z^0$  bosons between electrons and nuclei, a mechanism precisely described by standard electroweak theory. This is theoretically proposed to lift degeneracy and lead to small energy differences between the states of the two mirror image versions of a chiral molecule.[89] These effects have been experimentally observed in atoms but no experiment has yet achieved the sensitivity to observe it in molecules. [90, 91, 92, 93, 94] The scientific motivation behind such challenging experiment lies towards understanding the origins of homochirality in nature and its connection to the origins of life.[95, 96, 97] Nature displays the unique property of homochirality which describes the phenomenon seen in nature's main building blocks such as proteins, amino-acids and sugars, only naturally existing in one of the two enantiomeric forms. This exclusive preference is a key characteristic of life but its cause remains an unanswered fundamental question.

Parity-violation effects are calculated to be at the  $10^{-20}$  level for molecules consisting of light atoms such as carbon, oxygen or nitrogen found in most biomolecules that are naturally abundant.[98] These precision levels are far beyond current experimental capabilities. Theory predicts that parity-violating energy shifts scale with  $\sim Z^5$ , where  $Z$  is the nuclear charge of the heaviest atom in the molecule.[99]. Thus, ideal candidates are chiral molecules with very heavy atoms close to the chiral center, yielding shifts ideally on the order of  $\Delta_{pv}\nu/\nu = 10^{-15}$  or lower.[100, 101]The magnitude of the shifts exhibited



by transitions within a single electronic state is a fraction of the total electronic energy and is roughly proportional to the transition frequency.[102]Such shifts are calculated to be at the Hz to mHz level for transitions at  $\sim 30$  THz and approximately a factor of 1000 smaller for microwave transitions around 20 GHz, which is where our experiment operates [103, 104].

Blanchard et al. have proposed a series of NMR experiments to measure the nuclear-spin-dependent parity-nonconserving contributions to the molecular J-coupling Hamiltonian. They calculate the PNC coupling to be between  $\mu\text{Hz}$  and mHz and are planning to begin experiments with diatomics such as  $H^{19}F$  rather than chiral molecules.[105, 106]

High-resolution infrared spectroscopy has been the most promising method so far and has been implemented before to study weak fundamental effects.[107, 108] Table 5.1 describes selected previous efforts.

Chardonnet et al. has achieved the most promising effort yet with the molecule CHF-ClBr, with fractional precision of  $\Delta\nu/\nu = 5e - 14$  and absolute uncertainty of  $|\Delta\nu| \lesssim 8$  Hz. The French group has proposed since then a new experiment with a buffer gas cell apparatus aiming for two orders of magnitude sensitivity improvement[109, 103, 110]. They will be introducing the molecules within a buffer gas cell as the means of cooling before detection through a Ramsey interferometer, as seen in Figure 5.1. Our main goal for this experiment is a complimentary effort to the French approach. We are using microwave systems that are much more precise, stable and easy-to-use than tabletop infrared systems to explore the systematics at different levels of precision. This is the first precision differential measurement done in molecules in a buffer gas cell.

Table 5.1: Comparison of this work to selected previous efforts, and one proposed measurement.

Molecule	Uncertainty	Fractional precision	Method	Author
camphor	300 kHz	1.25e-8	ro-vibrational	Arimondo et al [111]
CHClFBr	8 Hz	2.5e-13	vibrational	M. Ziskind et al [112]
iron complex	45 kHz	1.2e-14	Mössbauer	A.S. Lahamer et al [113]
undetermined, heavy	0.1 Hz	1e-15 (proposed)	IR-Ramsey I/M	A. Cournol et al [110]
1,2-propanediol	0.72 Hz	9.7e-11	rotational	present work

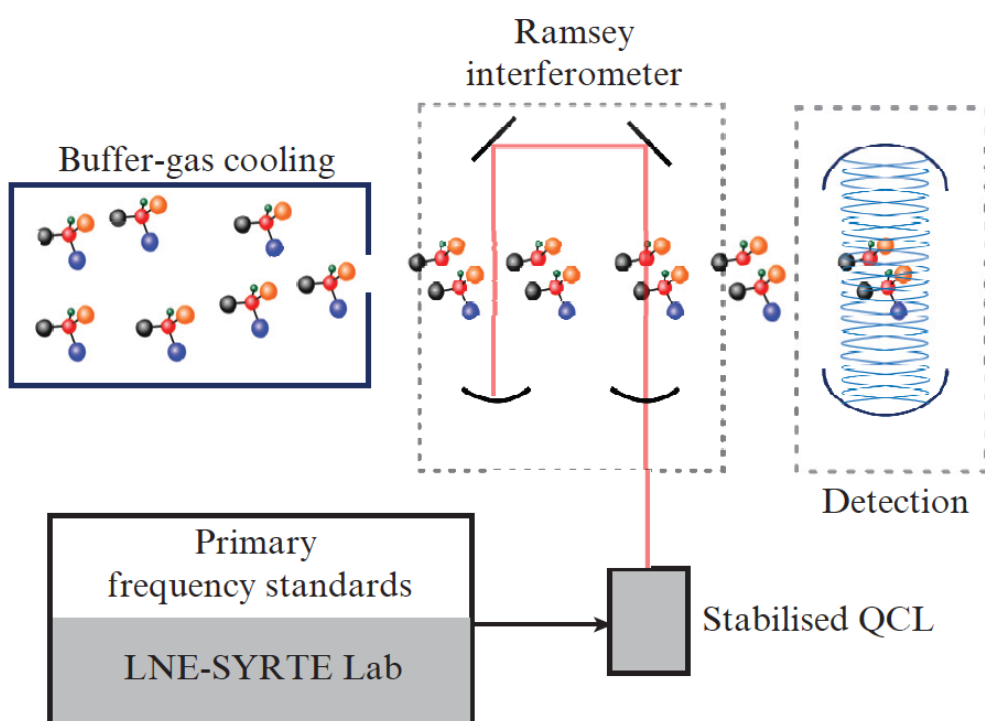


Figure 5.1: Schematic of the proposed French experiment to measure parity-violating effects in chiral molecules. Cold molecules are produced via buffer gas cooling before detection through a Ramsey interferometer. Figure taken from Ref. [110]

### 5.1.2 Buffer gas cells vs molecular beams

Molecular beams have been the state-of-the-art methods for high-resolution gas-phase microwave spectroscopy. The supersonic expansion allows for high densities at small volume, which is ideal for time-resolved experiments using focused laser beams.

For precision measurements, buffer gas cooling provides a few advantages. Because of the nature of the expansion, the shot-to-shot repeatability of a supersonic jet is low due to fluctuations in pressure and temperature. In a supersonic beam, the gas experiences many collisions near the exit aperture. The cooling mechanism of buffer gas cooling is fundamentally different. Thermalization occurs via collisions between a mixture of hot molecules and cold inert gas flowing continuously into the cell. A buffer gas beam of cold molecules forms when buffer gas and thermalized molecules escape via an orifice into a high vacuum region. These conditions are calmer, thus much more controlled and repeatable.

In the case that the molecular beam is parallel to the microwave propagation[114], each transition is split into a Doppler doublet. Doppler shifts are proportional to the velocity of the beam which is in the order of 600-1200 m/s for supersonic jets. The combination of high velocity, which limits interrogation time, with the appearance of doppler doublets, due to apparatus geometry, can significantly limit the overall sensitivity of the measurement. Buffer gas beams are much slower and continuous, thus allow for high spectral acquisition velocity exhibiting superior resolution and sensitivity. [115]

## 5.2 Experimental

### 5.2.1 Apparatus and Methods

The experiment was conducted in the larger 2nd generation buffer gas cell shown in Figure 6.1, described more in detail in the Experimental Apparatus chapter. The additional volume allows for longer free induction decays (FIDS) and thus capabilities for higher resolution. The smaller buffer gas cell routinely produced linewidths of 40-60 KHz, but in the larger cell we achieved resolution of 22 KHz with lots of room for improvement. A custom-built tunable plano-concave Fabry-Perot cavity[116, 117], the design and construction of which was led by Lincoln Satterthwaite and Daniel Sorensen, was coupled to the cell.

During the experiment, we were alternating between flowing (R)-1,2-propanediol and (S)-1,2-propanediol samples into the buffer gas cell via two identical ball valves. Samples were deposited on glasswool for gentle evaporation. Each time high signal-to-noise spectra of the  $|3_{03}\rangle - |2_{12}\rangle$  transition at 14716.9476 MHz were recorded.

The resulting free induction decays were fit to a decaying exponential function, and the frequency of this fit function was used as the center frequency of the line under observation. The envelope of the fit is used as an *in-situ* pressure measurement, allowing for pressure shift corrections as described below. A typical free induction decay and fit is shown in figure 5.3.

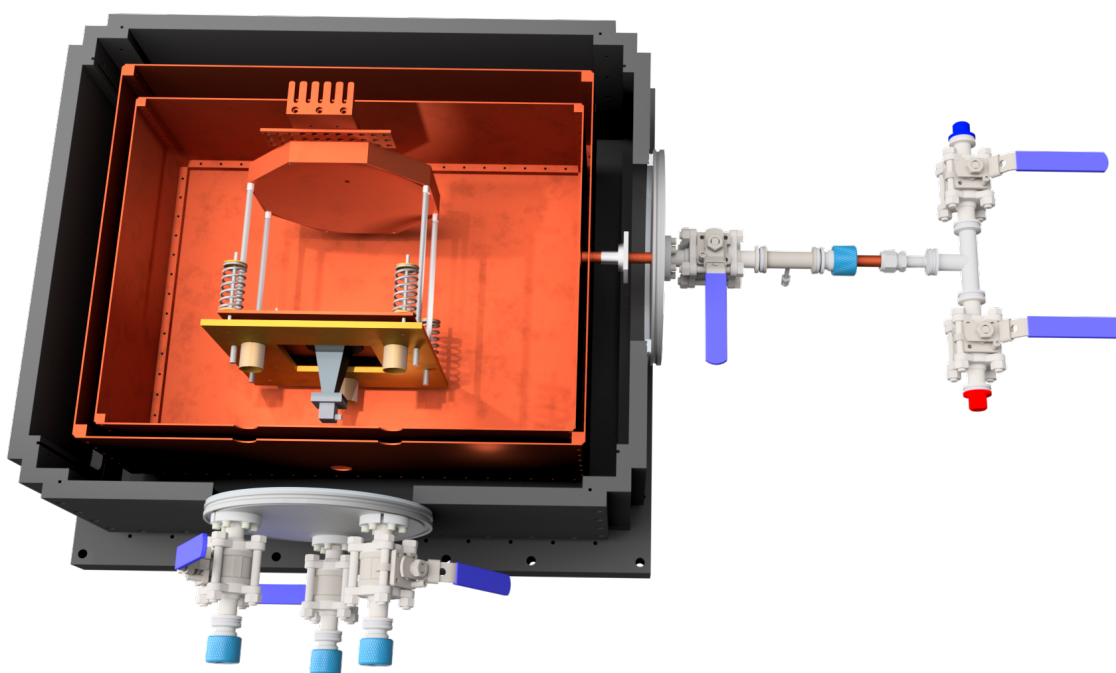


Figure 5.2: Top view of the larger second generation buffer gas cell. Within the cell, we have placed a Fabry-Perot cavity. The cavity is tuned via a screwdriver that is inserted via vacuum interlocks at three adjustment points. The two enantiomeric forms of 1,2 propanediol (shown as red and blue) are alternately introduced via a tube with fixed impedance.

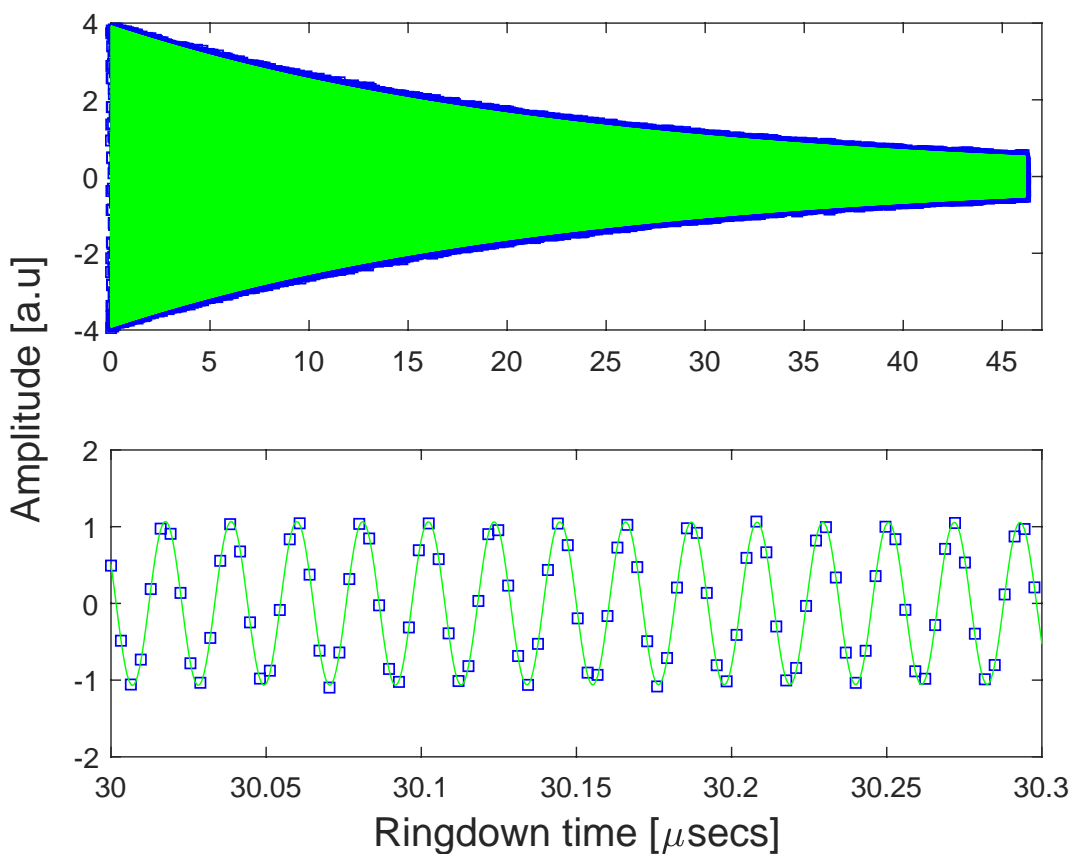


Figure 5.3: A typical free induction decay of R-1,2 propanediol. The FID is fit to the decaying exponential  $f(t) = A_0 e^{-t/\tau} \cos(f_0 t + \phi)$ .  $f_0$  is the intermediate frequency of the transition being probed, and  $\tau$  provides an in-situ measurement of the pressure. Bottom panel is an expanded view of top panel.

### 5.2.2 Cavity characteristics

Two 20 cm diameter copper mirrors are mounted 18 cm apart. One of the mirrors is a flat surface and the other has a spherical concave cutout with a 23.5 cm radius of curvature. The cavity is held and can be tuned at 6 K reducing reflective losses within the cavity. The 19th TEM<sub>00</sub> Gaussian-Hermite mode was used for the current measurements. Microwaves are coupled into the cavity from a WR62 waveguide through a sub-wavelength 0.5 cm diameter circular aperture in the concave mirror. Microwaves are coupled out through an array of circular sub-wavelength apertures in the planar mirror, designed to transmit radiation proportional to the Gaussian intensity profile of the TEM<sub>00</sub> resonant modes of the cavity. An unloaded Q factor of up to  $1.4 \times 10^5$  was measured, although the planar mirror was modified for improved signal and tunability yielding operational Q factors of approximately  $3 \times 10^4$ . Our molecular signals typically exhibit  $Q \approx 5 \times 10^5$ .

Circulating power in an off-resonant cavity can pull a molecular resonance towards the cavity resonance [118, 119, 120]. To explore this, we detuned our cavity by 200 kHz, and saw a pull of  $\Delta f_0 = 30$  Hz. The ringdown of the cavity is recorded with every signal acquisition plotted in figure 5.4, and the cavity frequency remained unchanged at the 1 kHz level over the course of the 2.5 hours of measurement, which corresponds to a pulling of approximately 0.15 Hz. However, because this is a differential measurement, the relevant figure is the shot-to-shot cavity stability.



## 5.3 Results

For our precision measurement, we measured the  $|303\rangle - |212\rangle$  rotational transition of 1,2 propanediol at 14716.9476 MHz. This is a differential measurement for which we alternated samples of (R)-1,2-propanediol and (S)-1,2-propanediol. In Figure 5.4, we show the residuals of the repeated frequency measurements for (R)-1,2-propanediol (blue squares) and (S)-1,2-propanediol (red squares). The top panel shows raw differential precision data and the bottom panel shows the corrected data after pressure shift systematic is subtracted. The red and blue rectangles indicate the frequency spread within each enantiopure sample.

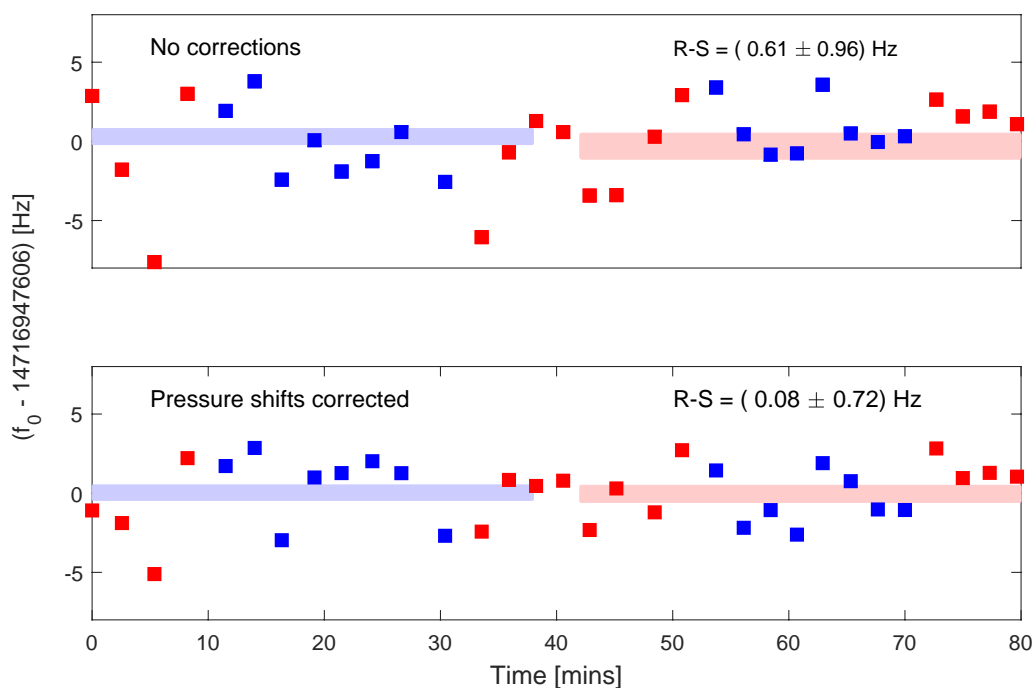


Figure 5.4: Repeated measurements of  $f_0$  of (R)-1,2-propanediol (blue squares) and (S)-1,2-propanediol (red squares). Top: uncorrected measurements. Bottom: Pressure shift corrected measurements. The measured precision is  $(0.08 \pm 0.72)$  Hz for the differential measurement of two enantiomers of the chiral molecule, 1,2-propanediol using microwave spectroscopy.

The molecular transition and timing of the cryogenic run were selected based of our knowledge of the spontelectric effect within the buffer gas cell, which was another systematic we were aware of. Stray electric fields in the buffer gas cell and Spontelectrics are discussed more in detail in the previous Chapter and under the systematics section below.

Small ( $\sim$ few Hz) corrections to these frequency were made by using the exponential decay coefficient as an in-situ pressure measurement. Table 1 summarizes the systematic error budget. We report precision of  $(0.08 \pm 0.72)$  Hz for the differential measurement of two enantiomers of the chiral molecule, 1,2-propanediol. This tight limit is realized in about 2.5 hours of data acquisition.

## 5.4 Systematics

The main goal of this experiment was the exploration of systematics at a certain level of precision for a differential precision measurement in a buffer gas cell. We encountered frequency drifts from a) Pressure effects and, b) Stray electric fields. Both these effects would be expected to exist in a microwave and in an infrared (vibrational) spectroscopic search for parity violation. Because of the similar absolute magnitude and smaller absolute uncertainty of a microwave measurement, a microwave measurement is more sensitive to these systematic effects than a higher frequency measurement. Table 5.2 provides an overview of the effects and their magnitude that they will be described below.

Systematic effect	Error budget (Hz)
uncorrected	$(0.61 \pm 0.93)$
DC stark shift	$< 0.5$ (see discussion)
pressure shift	$(0.53 \pm 0.24)$
amplitude shift	$< 0.1$ (see discussion)
statistical error	$(0.08 \pm 0.72)$

Table 5.2: Experimental error budget for the differential precision measurement of (R)- and (S)-1,2-propanediol.

### 5.4.1 DC Stark shifts

The frequency  $f_0$  varies with time, and we have strong evidence that this shift arises from slowly varying electric fields within the cell. This shift was small ( $\leq 0.5$  Hz) in the data run shown in Figure 5.4, and we did not correct for it. However, after many hours of running, the drift can accelerate to  $\sim 100$  Hz/hour. Even in this regime, the effect of this drift on our differential spectroscopy is largely mitigated by switching enantiomers rapidly compared to any change in the dynamics of this effect, and subtracting the drift from our measured frequencies. Figure 5.5 highlights the effect of those Stark shifts over

a longer time period, on an earlier experimental run. Subtracting the smoothly varying drift resulted in a net differential measurement error of less than 2 Hz even on runs where the Stark shift varied by  $\sim 200$  Hz over the course of the run.

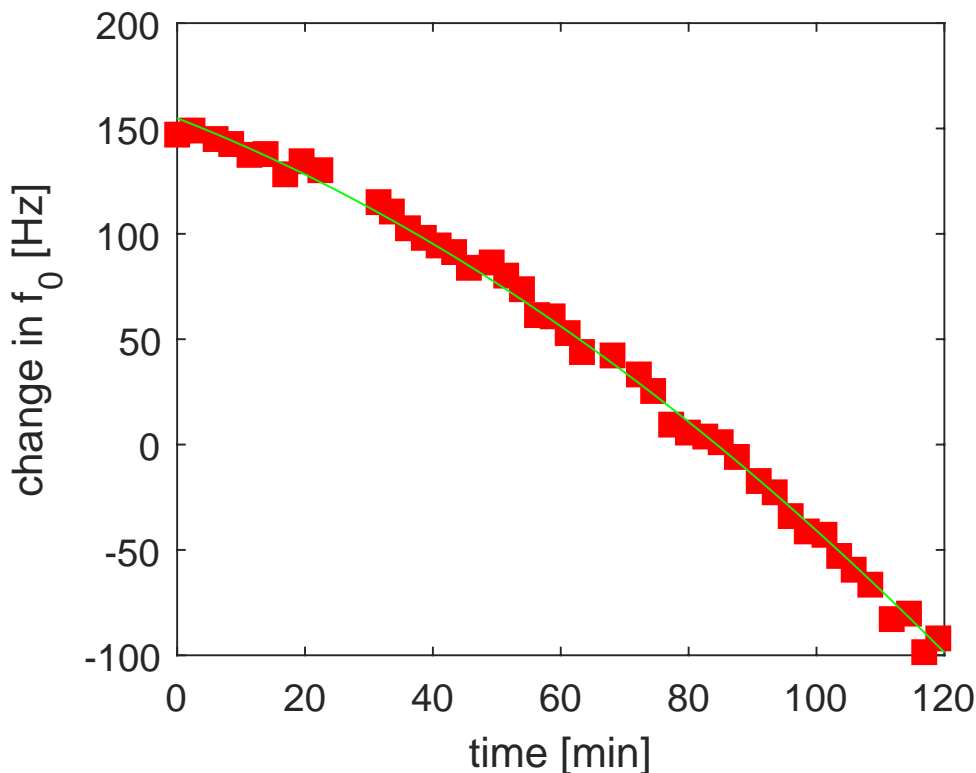


Figure 5.5: Repeated measurements of  $f_0$  of R-1,2 propanediol showing the drift of  $f_0$  over time. Although the uncorrected data shows a significant uncontrolled shift of  $\sim 200$  Hz, residual measurements of  $f_0$  show a standard deviation of  $\sim 2$  Hz when the overall drift and measured pressure shifts are subtracted. The data used for our primary result, taken early in a cryogenic run, showed a drift about 100 times smaller than what is shown here.

We first became aware of this effect while studying transitions with anomalously high Stark shifts involved in microwave three-wave mixing [121], where lineshapes consistent with the presence of a strong DC field appeared. This effect has been observed in polarizable transitions of 1,2-propanediol, fenchone, and a number of other chiral molecules. The effect is much stronger in highly polarizable transitions (transitions with large Stark

shifts), and can be partially, although not completely, mitigated by introducing free electrons into the chamber via laser ablation. We believe these free charges drift towards charge patches on the icy walls, much like in an anti-static gun such as those used to eliminate static charges from vinyl records.

We surmise that these fields are produced by the spontelectric effect [83, 122]. According to spontelectrics, gas-phase polar molecules deposited on to a cryogenic surface tend to align dipoles with already deposited molecules, yielding a net polarization which results in a strong, non-uniform electric field. These fields can be positive or negative depending on the molecular species, and grow linearly with film thickness [123, 124]. Though our experimental conditions are quite different than the the conditions under which these effects were first observed, this growing net polarization seems to be consistent with the observed drift of the center frequency of our line. It takes roughly an hour of flowing sample into the buffer gas cell for this effect to become the dominant systematic effect. In our apparatus, the distribution of the monolayers is almost certainly nonuniform, thus the dc field is highly anisotropic, so we can only provide a rough estimate of the order of the electric fields. Stark shifts for various observed transitions were simulated using the PGOPHER[125] package, putting an upper bound on the spontelectric field at 1500 V/m.

### 5.4.2 Pressure shifts

We use the ringdown times of the free induction decay signals as in-situ measurements of the local pressure at each data point. The buffer gas environment is a dynamic one, in which cold buffer gas but also room-temperature molecules enter the cell at each given moment. Even though we assume that our spectroscopic signals mostly stem from properly thermalized molecules, there are changes in the buffer gas pressure that matter

at certain levels of precision. We observed small ( $\sim 2\%$ ) uncontrolled fluctuations in the ringdown time, and thus the pressure. To understand the importance of the effect, we purposefully decreased the helium buffer gas pressure by 30%. This change shifted the raw uncorrected frequencies by  $35 \pm 5$  Hz but after corrections, the spread was less than 3 Hz.

### 5.4.3 Sample introduction and purity effects

We also studied the effect of purity and sample delivery between the two enantiomeric samples as potential systematics. The 1,2-propanediol samples were “96% pure”, and purchased from Sigma-Aldrich. One can imagine that an impurity - and even a non-polar impurity, which is invisible to our microwave spectrometer - might induce a shift. For example, if one enantiomeric sample contained a more volatile contaminant, it could affect the flux of molecules and induce pressure shifts. We did observe a variation in signal amplitude in the order of 5% between S- and R- enantiomers. Again, to investigate this further we purposefully introduced a surplus of one of the samples by 200% and studied its effects. This level of adjustment induced no observable shift in the measured  $f_0$  ( $\Delta f_0 < 2$  Hz). Using a conservative model where contaminants comprise 10% of the total molecular flux into the cell, we thus limit the hypothetical shift from such an effect to  $< 0.1$  Hz.

## 5.5 Discussion

We present the first differential precision measurement using microwave spectroscopy towards measuring parity-violating effects in chiral molecules. We measure the rotational transitions of the two enantiomeric samples of the chiral molecule 1,2-propanediol and confirm that the two enantiomers are structurally identical at the  $10^{-10}$  level. While this limit is orders of magnitude below the  $\Delta_{pv}\nu/\nu = 10^{-19}$  required to measure the PV

shift of such light molecule, it is the most precise measurement done with microwave spectroscopy to date and already shed additional insights to systematics towards higher precision.

### 5.5.1 Improving Resolution

The sensitivity to parity violation is determined by the precision of distinguishing between two line centers. Since systematic effects are directly related to linewidth, it is beneficial to reach the highest resolution possible. Higher resolution translates to free induction decays with ringdowns as long as 200 microseconds with low signal amplitudes that can affect the statistical uncertainty of the measured center frequency.[108, 126]

The spectral resolution of this experiment was 22 kHz and it was limited by collisional broadening inside the buffer gas environment. A straightforward improvement would be to separate the thermalization and detection region of the experiment. This can be achieved with the use of a collimated buffer gas beam. [127, 128, 129, 130]. Cold buffer gas, either helium or neon, can be introduced into a smaller cell with an opening at the other end. Inside the smaller cell, thermalization takes place and the cold molecules exiting the aperture at the back form a diffuse buffer gas beam. The molecules from the buffer gas beam can be further collimated ensuring only the center of the beam enters the cavity, which is the detection region. Preliminary results using a buffer gas beam show that we can achieve resolutions down to 3 KHz using Ne buffer gas.

We believe that this improvement will directly address the two dominant systematics discussed above. Separating thermalization and detection should decrease the effect of pressure shifts to the actual measurement. Also, DC Stark shifts caused by spontaneous electric fields should decrease significantly since less quantity of molecules would be introduced into the cavity and subsequently freeze on the walls.

### 5.5.2 Choosing molecular candidates

The quest of the ideal molecular candidate is one of the most challenging parts of measuring parity-violation effects in chiral molecules. As mentioned in the first section, the PV energy difference scales as  $\sim Z^5$ , where  $Z$  is the nuclear charge of the heaviest atom in the molecule. For our first measurement of differential precision, we used 1,2-propanediol which is too light to produce PV shifts that can be measured within experimental capabilities of the next decade.

One of the main challenges about selecting potential candidates is the limited selection of commercially available chiral molecules that fulfill the requirements needed. Measuring parity violation effects is demanding not only precision-wise but also a challenge of asymmetric chemical synthesis. Exotic candidates such as GeHFCIBr or SeOFCI or chiral oxorhenium complexes that are methyltrioxorhenium (MTO) derivatives are commonly suggested, however the synthesis and availability of these candidates in both enantiomeric forms still remains elusive.[131, 89] The molecular candidates need to:

- Display a parity-violation frequency difference within reasonable experimental precision capabilities which is at the 0.1-10 Hz precision level. This requires at least one heavy atom near the chiral center.
- Be available in both stable enantiomeric forms, ideally commercially. High purity and overall % of enantiopurity is important for sensitivity purposes and impurities-related systematics.
- Have high enough vapor pressure to produce large enough densities for spectroscopic measurements in the gas-phase.
- Be polar and display molecular transitions at specific frequency regimes. An advantage of microwave spectroscopy is that once a molecule is chiral and polar, it is detectable



with increased sensitivity within the standard 10-22 GHz microwave setups. However, this is not the case for vibrational spectroscopy experiments using laser systems. For these efforts, the molecular candidates need to display vibrational transitions at the very narrow stable range of their laser systems which is usually at 30 THz.

- Be cost-efficient. Current experimental needs for characterizing exotic molecules include acquiring high-sensitivity spectra for assignment and lots of experimental time spent in troubleshooting and understanding systematics. This sets the sample requirements at approximately tens of grams per measurement, which can be very costly and time-consuming if the sample is not commercially synthesized.

Some commercially available candidates that I singled out are shown in Figure 5.6 and described below. These have a few of the requirements such as availability in both enantiomeric forms but they are not cost-efficient.

- **(p-Toluenesulfinyl)ferrocene** is available in both enantiomeric forms from Strem Chemicals. Ferrocene-type chiral molecules could be an interesting direction since they are known to exhibit high vapor pressure. It retails for \$670 per gram.
- **6,6'-Dibromo-1,1'-bi-2-naphthol** is available in both enantiomeric forms from Strem Chemicals and Sigma-Aldrich at \$253 for 2g. This molecule is chiral due to its geometry in 3D and does not display the traditional stereogenic carbon center. It is similar to rotor-like chiral molecules recently studied by the French group containing Ruthenium[132]

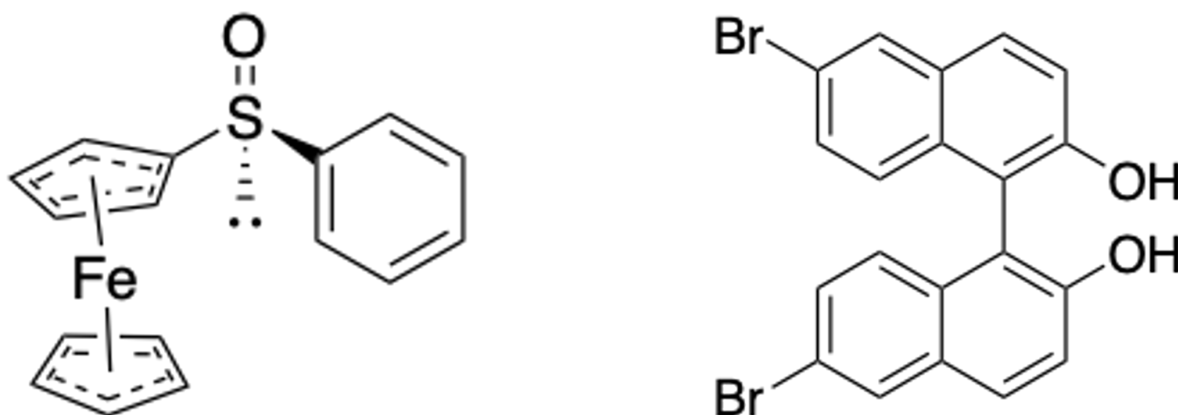


Figure 5.6: Commercially available promising candidates for measuring parity-violating effects in chiral molecules. (Left) p-Toluenesulfinylferrocene. (Right) 6,6'-Dibromo-1,1'-bi-2-naphthol

# Chapter 6

## Low temperature dimer formation

In this chapter, I will be describing our experimental results on low temperature dimer formation in a buffer gas cell. For these experiments, we are using the buffer gas environment not only as a cooling medium but also as a science medium, testing its capabilities for cold chemistry studies.

These results became possible due to two main upgrades on the main apparatus: a) the construction of the larger buffer gas cell and, 2) the multiple-input sample introduction. Van der Waals clusters have been studied for decades using supersonic molecular beams. This method precludes the observation of the formation of the cluster, as the clusters form in the uncontrolled, rapidly changing environment just after the orifice of the pulsed valve. Our separate inputs allow for independent introduction of the reactants ensuring dimerization takes place inside the buffer gas cell under cold conditions and not prior to that. This way, we are able to extract kinetic rates of formation.

For the first experiment, we formed dimers of ethanol-ethanol, ethanol-methanol and ethanol-water at 10 K. Time profiles of the concentration of reagents in the cell yielded gas-phase reaction rate constants of  $k_{Me-g} = 2.8 \pm 1.4 \times 10^{-13} \text{ cm}^3 \cdot \text{molecule}^{-1} \text{ s}^{-1}$  and  $k_{Me-t} = 1.6 \pm 0.8 \times 10^{-13} \text{ cm}^3 \cdot \text{molecule}^{-1} \text{ s}^{-1}$  for the pseudo second-order ethanol-

methanol dimerization reaction at 10 K. The relaxation cross section between the gauche and trans conformers of ethanol was also measured using the same technique. Thermodynamic relaxation between conformers of ethanol over time allowed for selection of conformer stoichiometry in the ethanol-methanol dimerization reaction, but no change in the ratio of dimer conformers was observed with changing ethanol monomer stoichiometry. These results have been submitted for publication to the Journal of Physical Chemistry A.

“Low-temperature gas-phase kinetics of ethanol-methanol heterodimer formation (2023). L.Satterthwaite, **G. Koumarianou**, P. B. Carroll, R. Sedlik, I. Wang, M. McCarthy, D. Patterson. J. Phys. Chem. A (Submitted).”

Following up these results, we also performed a study of the real-time formation of the water dimer and seven of its isotopologues. Quantum tunneling plays a major role in cold chemistry kinetics especially in the water molecule, but it is quite unexplored how specific tunneling motions affect the dynamics. Large kinetic isotope effects and reaction rate trends reveal the impact of symmetry and specific tunneling mechanisms in hydrogen dimer bond formation and present a deconstructed image of the rich dynamics of the water dimer. This is a fresh approach on understanding low temperature kinetics via quantum effects in water and other van der Waals complexes, without the cost and sample limitations present in current state-of-the art methods like CRESU.

## 6.1 Low-temperature kinetics of ethanol-methanol and ethanol-water heterodimer formation

### 6.1.1 Gas-phase monomer + monomer $\rightarrow$ dimer formation

Cold gas-phase van der Waals clusters have been studied extensively for the past decades using molecular beams. The highly collisional environment of a supersonic expansion creates the right conditions for the formation of various sizes of clusters near the exit aperture. By varying the backing pressure of the expansion, the type of noble gas used and the concentration of the sample diluted in the seeded gas, one can produce and study a variety of cluster sizes from dimers to hexamers and decamers.[133, 134, 135, 136, 137]

Microwave spectroscopy has been an essential tool for the quantitative determination of the structure of small clusters [138, 139, 140, 141, 142]. The rotational resolved spectra allow for structural studies of several cluster conformations and their isotopes. However, using supersonic jets is limited to only studying the already formed clusters excluding all information about formation.

The state-of-the art method for studying kinetics and reaction dynamics in the gas phase is the Cinétique de Réaction en Ecoulement Supersonique Uniforme (CRESU) method. This method uses a Laval nozzle to create cold, uniform, high flux beam of molecules entrained in a carrier gas. The CRESU method has provided rich insights on the kinetics of formation of many open and closed shell species at known temperature and pressure conditions. [143, 144, 145] Even though the CRESU methods has been coupled with broadband microwave spectroscopy and has the capabilities of studying conformer- and isotopologue-specific kinetics, it has some limitations. Laval nozzles require vast amounts of carrier gas and molecular sample to maintain the expansion with good concentration, typically of order  $3 \times 10^3 \text{m}^3 \text{h}^{-1}$  of carrier gas and  $<1\%$  sample[146].

Such high sample consumption precludes the use of certain samples and makes a full isotopic and conformation study very costly.

Here, we present the results of a conformational kinetic study of the formation of ethanol-methanol dimers in a cryogenic buffer gas cell. The different cooling mechanism used in buffer gas cooling allows the study of the formation process of thermalized cold monomers into dimers and the underlying kinetic mechanisms such as hydrogen bonding at low temperatures. We use two separate inputs to introduce the different monomers and take advantage of the conformational relaxation previously observed in buffer gas environments to select the lowest energy conformer for reaction.[147].

The methanol-ethanol dimer is a great candidate for such demonstration. The trans ethanol conformation is the ground state followed by the quasi-degenerate gauche+ and gauche- conformers at 56 K and 61 K above the ground state respectively (which is equivalent to roughly  $40 \text{ cm}^{-1}$ ).[148] Methanol only has a single conformation. By delaying the introduction of the second reactant, which is methanol, till ethanol is fully thermalized to its ground state conformer we study the effects of conformation to low temperature dimerization towards different reaction channels based on resulting dimer conformation. Finneran et al. characterized and provided experimental rotational constants for the lower energy conformations of the dimers such as methanol-trans-ethanol (Me-T) and methanol-gauche-ethanol (Me-G). [149, 150] The two conformations have an energy difference of  $150 \text{ cm}^{-1}$  which is equivalent to 215 K. We provide rate constants and collisions cross sections for these reactions. We also performed the same experiments to ethanol-ethanol and ethanol-water dimers.

## 6.1.2 Apparatus and Experimental Methods

### Experimental design

The apparatus used is the 45 cm  $\times$  25 cm  $\times$  27 cm buffer gas cell shown in Figure 6.1 and explained further in detail in the Experimental Setup chapter. We used a simple horn configuration with two horns facing one another operating at 10-18 GHz. The signal was fed into a low-noise cryogenic amplifier and into our standard microwave circuit. Cold helium buffer gas was continuously flowed at 10 SCCM, resulting in a steady-state helium density of roughly  $n_{He} = 10^{14} \text{cm}^{-3}$ .

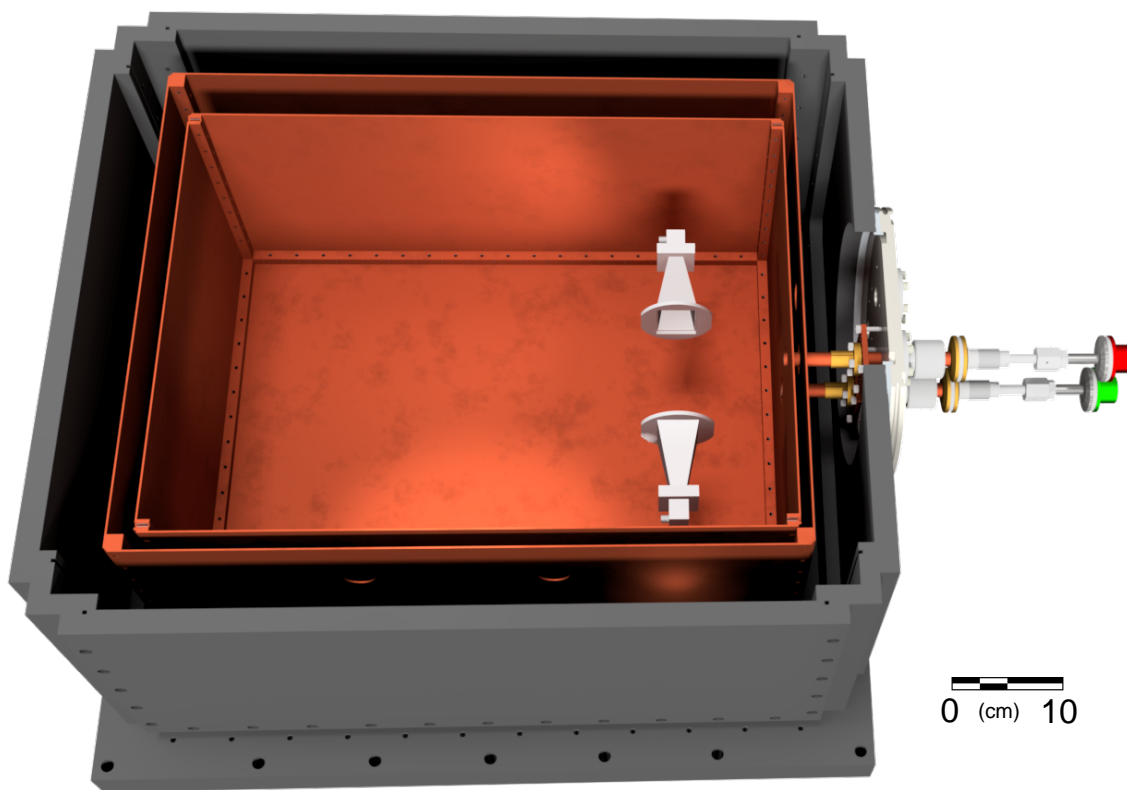


Figure 6.1: Buffer gas cell apparatus for dimer formation. Valve 1 (red) was backed by ethanol, and valve 2 (green) was backed by methanol. Horns were located to provide best overlap with the expanding gas cloud.

For ensuring separation of the molecular samples until they react within the buffer gas cell environment, two separate but identical sample input manifolds were employed. Each manifold consisted of a 4 inches copper tube connected to a Parker series 9 pulsed valve operating at 0.8 Hz. Each valve is backed by samples of ethanol (48 Torr) and methanol (102 Torr) respectively at room temperature. No carrier gas was used.

The repetition rate of the valve was optimized for obtaining the maximum signal-to-noise ratios while keeping heatloads to the minimum. The delay between the valves was set to values between 0 and 40 ms, as shown in Figure 6.2, with ethanol leading for the conformational relaxation study. The data were collected at different times since the first valve opening time at  $\tau - (T_{\text{window}}/2)$  up to time  $\tau + (T_{\text{window}}/2)$ . This allowed for a time domain picture of signal amplitudes for each species in the buffer gas cell at a given time.



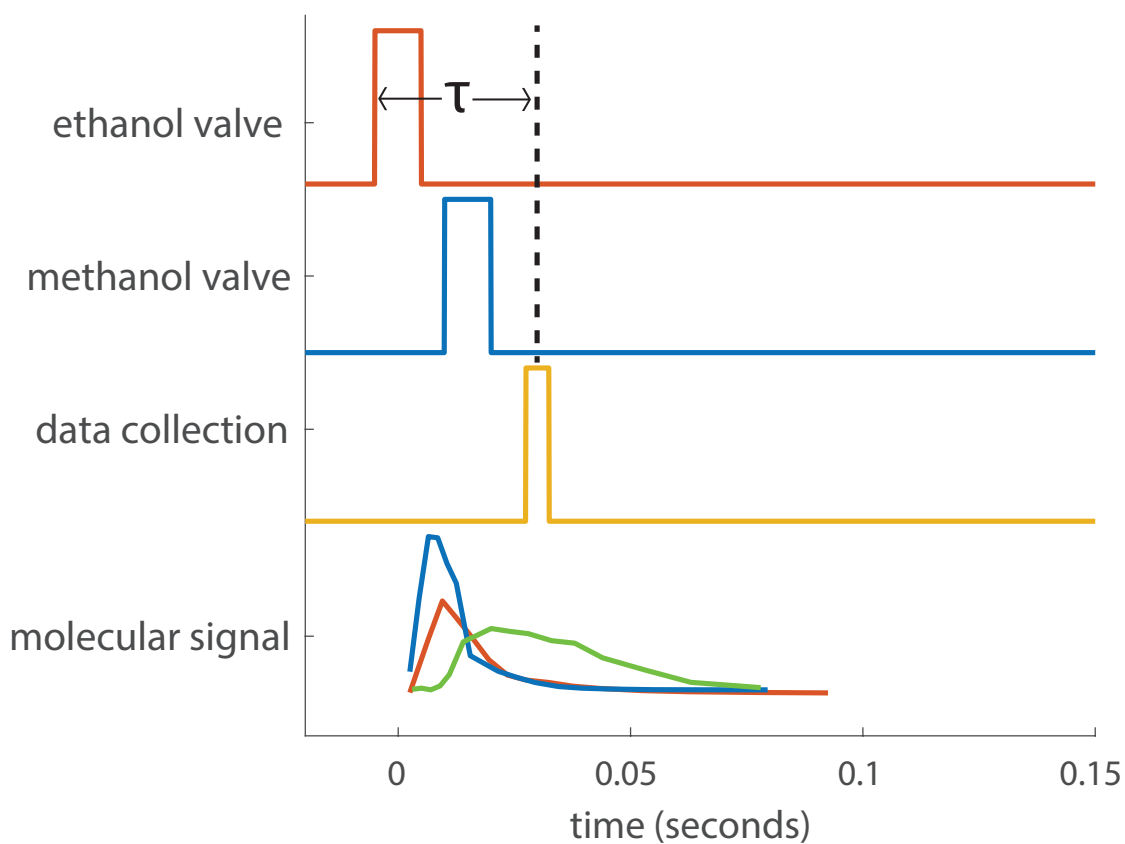


Figure 6.2: Timing diagram for the experiment. The delay between the first valve and the center of the data collection window is  $\tau$ . The delay between the ethanol valve and methanol valve is adjusted to change the effective stoichiometry of the dimer-forming reaction. The colors on the bottom trace correspond to the timing trace of the same color, with the green trace being dimer signal.

## Valve Controller Box

The Parker Series 9 Pulse valves were controlled by a custom built relay box. The relay box is a dual channel switching box that consists of four switches, a power supply, and two solid state relays. It takes one TTL input per channel. If the TTL input is more than 3V then the relay connects a Bel Power MBC201-1T30G 30V DC power supply to the output of that channel. Additionally, a manual switch can be flipped to get a 30V output without TTL input. The primary use of this is to fire a Parker Series 9 Pulse valve with a TTL signal, which allows for precise pulse valve timing and control.

## Density Calibration for rate constant derivation

In order to extract rate constants out of the experimental reaction rates measured, we need to calibrate between the raw voltage of the experiment and the density of molecules in the cell at a given time. For calibration, we performed a direct absorption measurement for the methanol  $|2_0\rangle - |3_{-1}\rangle$  transition at 12178.58 MHz. Methanol has an absorption cross section of roughly  $10^{-11}$  cm<sup>2</sup> and a dipole moment of 1.4 D.[151] The in-cell peak density was determined to be  $2 \times 10^{12}$  cm<sup>-3</sup> for methanol, and about  $5 \times 10^9$  cm<sup>-3</sup> for all dimer species. These values were used along with the reaction rates calculated from the linear fit of the rise time of the dimer signal to extract the rate constant for each dimer formation.

The value for density derived from absorption was checked by measuring valve reservoir depletion over time. The pulsed valve was backed with a 20  $\mu$ L sample of methanol, and the depletion of the reservoir as a function of number of valve pulses was measured by plotting signal amplitude over an hour of runtime, or 2880 valve pulses, as shown in Figure 6.3. From the known quantity of methanol backing the valve, and know number of valve pulses, a number of ethanol molecules per pulse was extracted. The ratio of

the number of molecules per pulse to the volume of the buffer gas cell yields a ceiling of molecule density in the cell,  $2.3 \pm 1 \times 10^{12} \text{ cm}^{-3}$ , which agrees with the absorption measurement.

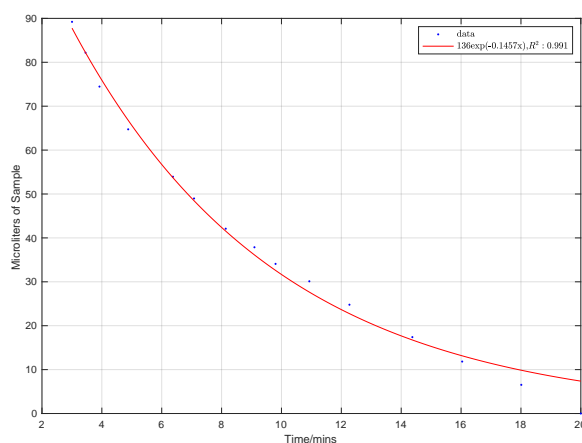


Figure 6.3: For calibration purposes, a known amount of sample was introduced into the cell for a known amount of time (pulse valve pulse duration) to calculate molecule density. The pulsed valve was backed with a 20 L sample of methanol, and the depletion of the reservoir as a function of number of valve pulses was measured by plotting signal amplitude over an hour of runtime. The ratio of the number of molecules per pulse to the volume of the buffer gas cell yields a ceiling of molecule density in the cell,  $2.3 \pm 1 \times 10^{12} \text{ cm}^{-3}$ , which agrees with the absorption measurement.

### 6.1.3 Results

#### Dimer formation in the cell

Figure 6.4 shows time-domain data of dimer formation inside the cryogenic buffer gas cell. In the top panel, we show the traces of all the monomers including ethanol g+ and g-, trans-ethanol and methanol. Peak monomer signals peak approximately between 0-20 ms. At the bottom panel, we show the traces of the ME-g and ME-t dimers formed inside the buffer gas cell. ME-g stands for methanol binding to gauche-ethanol as the hydrogen bond donor and ME-t stands for methanol binding to trans-ethanol as the hydrogen bond donor. The dimer traces peak at 20 ms and later. This is proof that the formation takes place inside the buffer gas cell.

In Figure 6.4, the temporal profile of the rising side of the curves was linearly fit and the slope was used to calculate the reaction rate or the  $\frac{d[\text{dimer}]}{dt}$  part of the rate equation:

$$\frac{d[\text{dimer}]}{dt} = k \times [\text{methanol}][\text{ethanol}] \quad (6.1)$$

where  $k$  is the rate constant, and  $[\text{methanol}]$  and  $[\text{ethanol}]$  are the concentration of the monomers in units of  $\text{cm}^{-3}$ . The methanol concentration was directly calculated from our calibration. The concentration of ethanol was calculated to be  $3.5 \times 10^{11} \text{ cm}^{-3}$ , based on  $\mu_a$  dipole moment of 1.264 D and a partition function of 0.014 measured at the  $|1_{01}\rangle$ - $|0_{00}\rangle$  transition. Combining these three quantities, we extract a rate constant of  $k_{Me-g} = 2.8 \pm 1.4 \times 10^{-13} \text{ cm}^3 \cdot \text{molecule}^{-1} \text{ s}^{-1}$  for the formation of ME-t and  $k = 1.6 \pm 0.8 \times 10^{-13} \text{ cm}^3 \cdot \text{molecule}^{-1} \text{ s}^{-1}$  for ME-g.

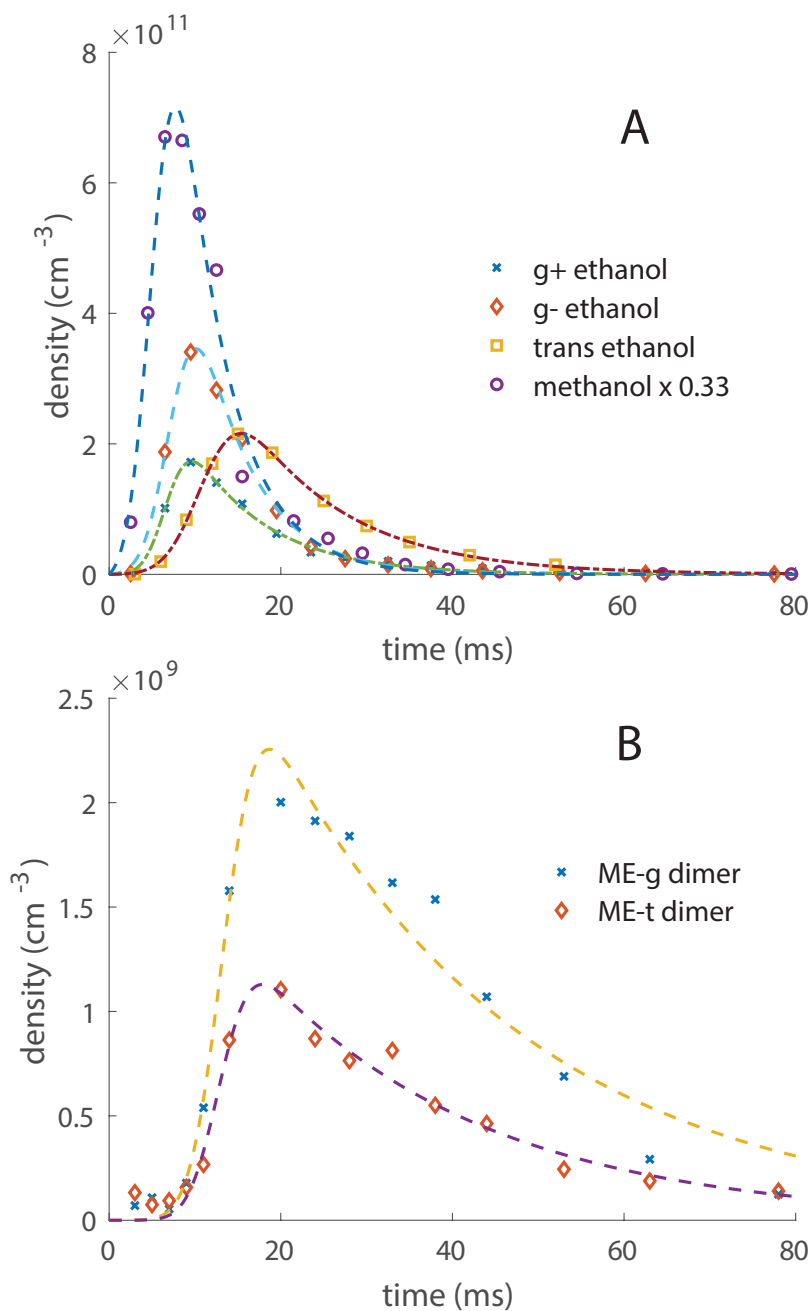


Figure 6.4: Time profile of relative populations of A) ethanol and methanol monomers and B) two lowest energy methanol-ethanol dimers. The dimer traces peak at 20 ms and later, proving that dimer formation takes place inside the buffer gas cell. The rising side of the dimer data is used to extract dimer formation reaction rates, while fits from the decaying side give diffusion rate information for processes inside the buffer gas cell. Fit parameters for diffusion are shown in Table 6.1

Table 6.1 shows experimentally derived diffusion decay times for all monomer and dimer species. These values were used to calculate diffusion and relaxation cross sections.

Quantity	symbol	value	unit
$\tau_{\text{decay}}$	$\tau_{D,MeOH}$	6.5	ms
	$\tau_{D,t-EtOH}$	14.1	ms
	$\tau_{D,g-EtOH}$	10.0	ms
	$\tau_{D,ME-g}$	26.7	ms
	$\tau_{D,ME-t}$	30.7	ms
diffusion cross section	$\sigma_{D,MeOH}$	$2.94 \times 10^{-15}$	$\text{cm}^2$
	$\sigma_{D,t-EtOH}$	$3.2 \times 10^{-15}$	$\text{cm}^2$
	$\sigma_{D,g-EtOH}$	$3.2 \times 10^{-15}$	$\text{cm}^2$
relaxation cross section	$\sigma_{D,dimer}$	$8.13 \times 10^{-15}$	$\text{cm}^2$
	$\sigma_{c,gt}$	$2.3 \times 10^{-17}$	$\text{cm}^2$

Table 6.1: Table of fit parameters and derived quantities for the exponentially decaying parts of the time domain data seen in Figure 6.4.  $\tau$  is extracted from the decaying part of the traces and was used to calculate the rest of the parameters.

### Cross section calculations

The loss rate of the molecules in the cell is dominated by diffusion. From the time-domain data, we can also extract diffusion cross sections by fitting the decaying part of the molecular time traces to a decaying exponential and use a simple diffusion model described more in detail by Drayna et al.[152]

For a helium flow  $f$  of 10 sccm ( $42 \times 10^{17} \text{ s}^{-1}$ ) and cell aperture  $A = 2 \text{ cm}^2$ , we can calculate the helium thermal velocity and helium density at 7 K given equations 6.2 and 6.3.

$$u_{He} = \sqrt{\frac{8k_B T}{\pi m_{He}}} \quad (6.2)$$

$$n_{He} = \frac{4f}{Au_{He}} \quad (6.3)$$

Assuming that the gas in the buffer gas cell is dilute so  $n_{He} + n_{molecule} \approx n_{He}$ , we can use 6.2 and the reduced mass of the helium-molecule complex for each monomer and dimer to calculate the reduced thermal velocities for each species. Using the diffusion times from the experimental fitted decay times, shown in Table 6.1, we use equation 6.4 to calculate diffusion cross sections for methanol, trans-ethanol, gauche-ethanol and the ME-t-1 dimer. The calculated values can be found in Table 6.1.

$$\sigma_D = \frac{9\pi u_{He-molecule} \tau_{decay}}{16 n_{He} L^2} \quad (6.4)$$

We can also extract the conformational relaxation cross section of ethanol from the gauche+/gauche- species to trans-ethanol, which is the energetically lowest conformational state. By using the experimental values for the time-dependent population in the excited conformational state and ground conformation state, we can use equation 6.5 to calculate the cross section.

$$\frac{N_{trans}(0) N_{gauche}(t)}{N_{gauche}(0) N_{trans}(t)} = e^{-2n_{He}\sigma_C u_{He}} \quad (6.5)$$

The decay time  $\tau_{FID}$  of the free induction decay signals can be used to calculate helium-monomer and helium-dimer collisional cross sections, from equation 6.6. We calculate collisional cross section values of approximately  $2 \times 10^{-14} \text{ cm}^2$  for both monomers and dimers.

$$\frac{1}{\tau_{FID}} = n_{He}\sigma_C u_{He-molecule} \quad (6.6)$$

### Conformer-selected dimer formation

Figure 6.5 shows our conformer-selective formation data. Ethanol trans and gauche conformers are separated by 59 K. In room temperature, this means that all three conformations occur in equal amounts, however in the cryogenic buffer gas cell environment, ethanol gauche relaxes to ethanol trans. We have calculated this relaxation cross section to be  $2.3 \times 10^{-17} \text{ cm}^2$ , from the data shown in Figure 6.4. As seen at the top of Figure 6.5, some of the gauche ethanol population relaxes into trans ethanol. The trans/gauche ratio increases over time as more molecules get thermalized.

We introduce methanol at different times so it is exposed to different stoichiometry of ethanol conformations. This way we can study the effect of conformation to the dimerization process. As shown at the bottom of Figure 6.5, we monitor trans/gauche ratio of the monomer and the ME-g/Me-t dimer ratio, where g and t stand for gauche and trans ethanol monomer respectively. No change in the dimer formation ratio is observed. This result suggests that conformation is not preserved during the dimerization process.



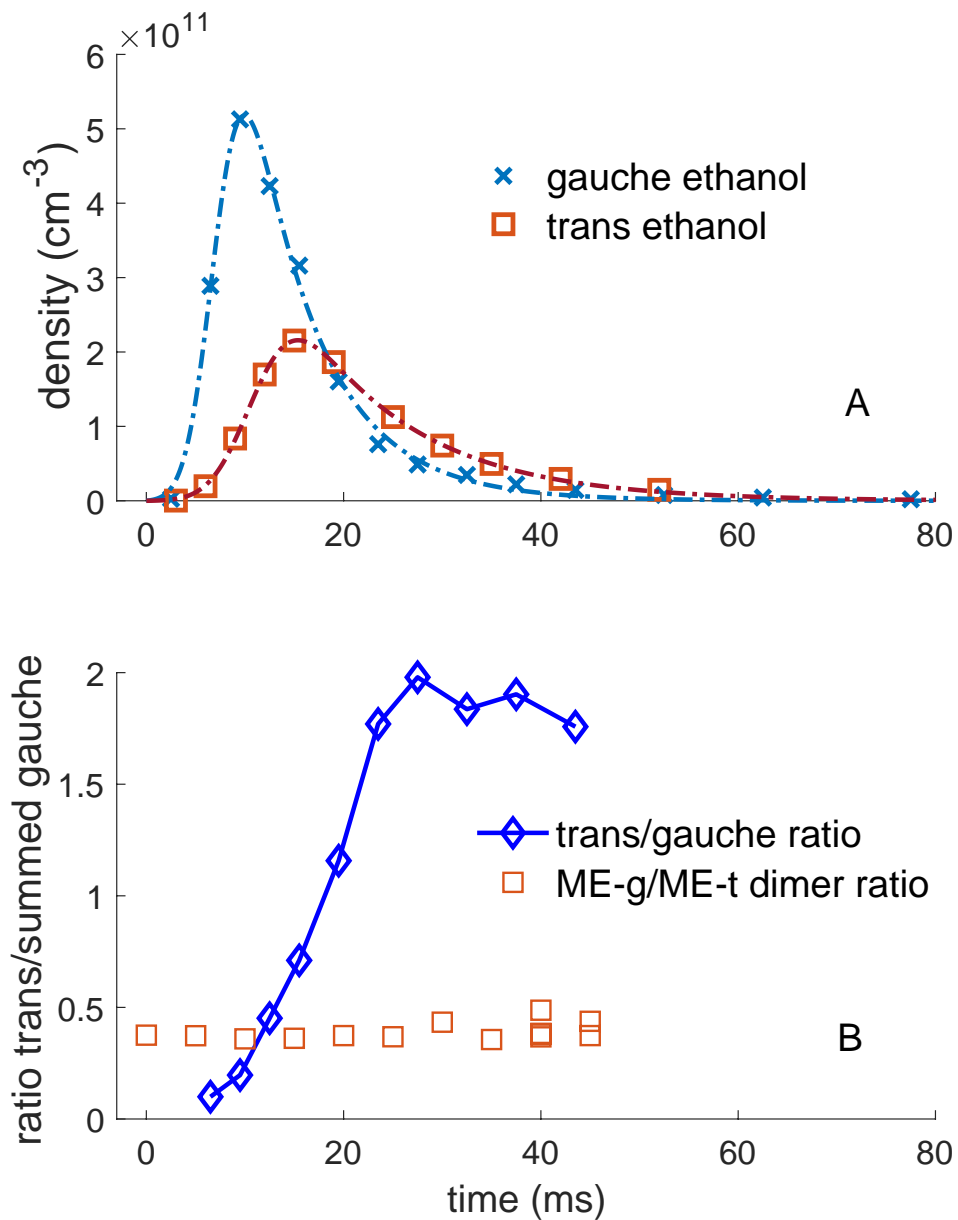


Figure 6.5: A) time-domain plot of reactants. The gauche ethanol trace represents the sum of g+ and g- conformer densities, as these conformers are quasi degenerate. Data is fit to the theoretical diffusion model described in section 3. B) As the ratio of gauche and trans ethanol monomer changes, the ratio ME-g and ME-t does not change.

### 6.1.4 Conclusion

We introduce a new method on directly observing and studying the formation of small gas-phase dimers via microwave spectroscopy in a controlled cryogenic environment. We extract gas phase reaction constants for the ethanol-methanol dimerization at 8 K and study the effect of conformation at such low temperature reactions. Thermodynamic relaxation between conformers of ethanol over time allowed for selection of conformer stoichiometry in the ethanol-methanol dimerization reaction, but no change in the ratio of dimer conformers was observed. This result suggests that conformation is not preserved during such process.

## 6.2 Kinetic Signatures of Quantum Tunneling in Water Dimer Formation

This experiment started as a follow-up idea to the ethanol dimers. Water is one of the most interesting small molecules as it is a prototypical model of the hydrogen bond but also displays very rich quantum tunneling dynamics that might dominate in low temperatures. For this low temperature kinetic study, we measured kinetic traces over time for water and seven of its isotopologues and extracted reaction rate values and rate constants. Measuring different isotopologues allowed us to explore specific insights on how the tunneling motions participate in the dynamics of the water dimer formation.

### 6.2.1 Quantum tunneling and cold chemistry

Over the past forty years, there have been extensive studies on elementary gas-phase chemical reactions at low temperatures, establishing the field of cold chemistry kinetics. The dominant contribution has been the CRESU (Cinétique de Réaction en Ecoulement Supersonique Uniforme) method. Using a Laval nozzle, absolute rate constants can be directly extracted at various temperatures and pressures.[146, 153, 154, 144, 143, 155]

Those studies have shown that cold reactions exhibit non-Arrhenius behavior manifesting as unexpectedly high reaction rates at low temperatures.[156, 157] This effect has been attributed to a suite of nuclear quantum effects (NQEs), such as zero-point energy and specifically to quantum tunneling.[158, 159, 153, 154, 160] However, there have been no studies providing any insights on how specific tunneling motions affect the reaction dynamics.

The water dimer is an excellent candidate for studying NQEs in this context.[161, 162] It is the prototypical hydrogen-bonded cluster with extensive experimental and theoret-

ical tunneling information available.[163, 164, 165, 166, 167, 168, 169] Cold reactions occurring via van der Waals intermediates have been shown to be particularly enhanced by quantum tunneling.[158, 170, 171]

Water dimers are important elements in understanding the bulk properties of water and are of great interest to atmospheric research [172]. Low-temperature spectroscopic studies of water complexes and their isotopologues have been conducted with infrared and microwave spectroscopy in molecular beams [173, 174, 175, 176, 177, 10], cryogenic rare gas matrices [178, 179] and helium nanodroplets.[178, 179]Until now, such studies have been limited to structural and spectroscopic information solely including type and magnitude of tunnelling splittings. Recent breakthroughs in computational approaches [180, 181, 182, 183, 184] provide a detailed overview of tunneling potential surface landscapes but the dynamic role of tunneling remains unexplored.

To understand the role of tunneling for the formation of the water dimer at low temperatures and further examine the relationship between tunneling effects and complexation, we performed an isotopic study of real-time water dimer formation in a cryogenic buffer gas cell at 10 K. Isotopologues are uniquely sensitive to quantum tunneling effects since substitution of specific hydrogen atoms with deuterium can selectively suppress specific motions, allowing for the deconstruction of the dynamics into simpler decoupled processes.

Isotopic studies using our microwave spectrometer are straightforward and can be easily performed for any species that can be buffer-gas cooled. Each isotopomer has a well-understood and distinct microwave spectrum, and data acquisition can be performed simultaneously for many species, similarly to our previous work [185, 186]. Our method provides an excellent complement to the kinetic data from the CRESU experiments [153, 154, 144, 143, 155] that have cost and sample limitations for performing isotopic studies.

Here, we introduce water monomers into a cryogenic buffer gas cell. Via isotopologue-specific microwave transitions, we monitor the population of both monomers and dimers in real-time. We extract experimental rate constants and kinetic isotope effect (KIE) ratios at 10 K. KIEs are key measurements for elucidating mechanisms and testing numerical simulations.[187] We present data for the water dimer and seven of its isotopologues and show how different quantum tunneling processes control the low-temperature dimer formation kinetics. To our knowledge, this is the first observation of water dimer isotopologue formation in a controlled cryogenic environment and a new approach to obtain kinetic cluster data and insights into tunneling processes. The three most dominant tunneling mechanisms for the water dimer are shown in figure 6.6. In each dimer, one water molecule acts at the hydrogen-bond donor and the other one acts as the the hydrogen-bond acceptor. In Methyl-Amine type of tunneling (or Acceptor Switching), the two acceptor hydrogens interchange causing rotational level splittings of 200 GHz. This is the only tunneling mechanism that does not break the hydrogen bond and is present in all dimer isotopomers [173]. The second most prevalent type of tunneling motion in the water dimer is Donor-Acceptor Interchange. Here, the acceptor and donor monomers interchange roles [188]. This causes splittings at the 10 GHz - 22 GHz level depending on the isotopomer in question [173]. In water dimers where H<sub>2</sub>O or D<sub>2</sub>O is the proton donor, Proton Donor Interchange tunneling mechanism is present. In this case, the hydrogen or deuterium within the proton donor switches positions in a more complex motion known as bifurcation [173]. These motion causes rotational splittings that are less than 1.8 GHz [178].

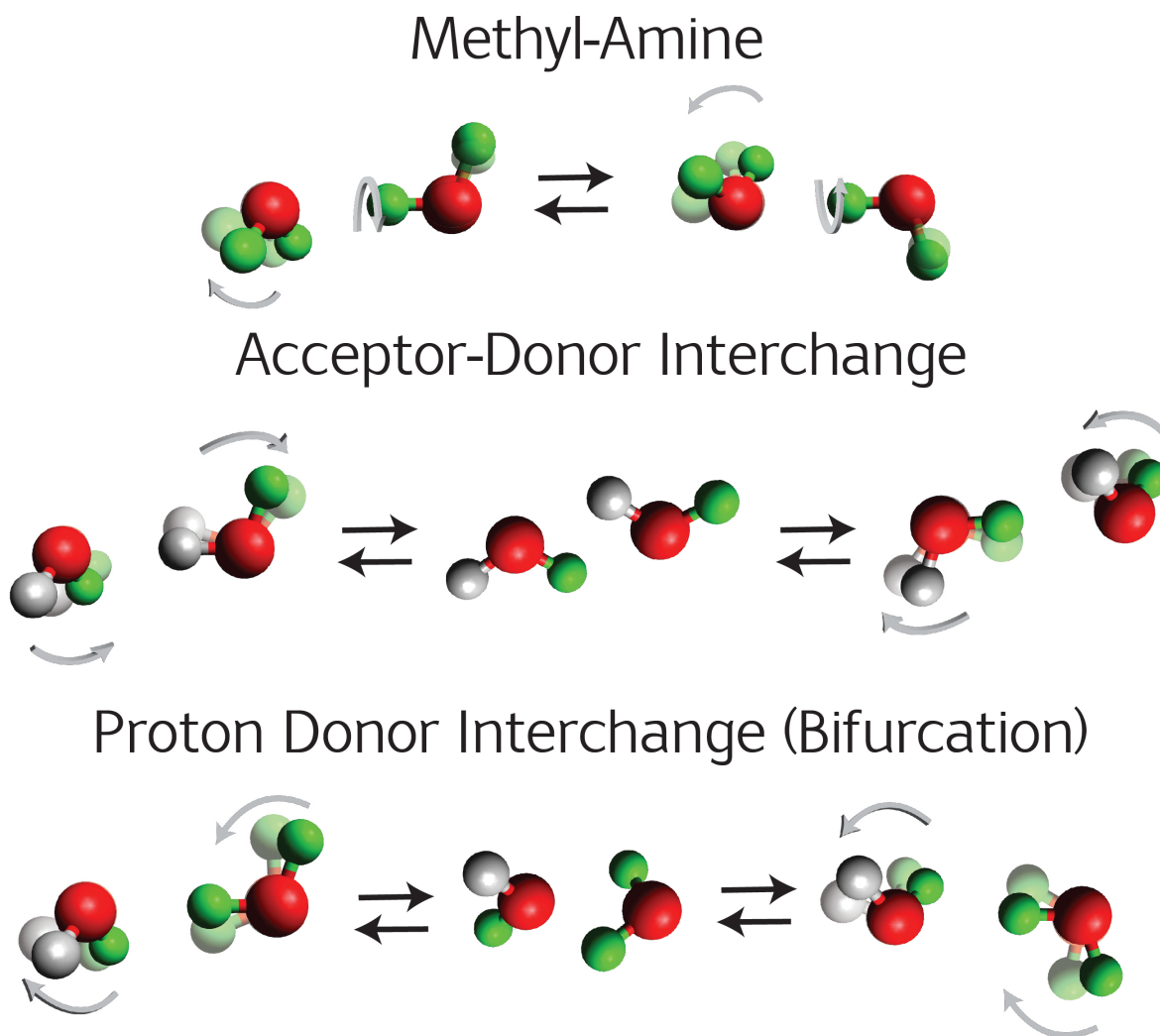


Figure 6.6: Qualitative schematic of the three tunneling processes of the water dimer. Hydrogen atoms (white) are substituted by deuterium atoms (green) to represent different isotopologues. Different isotopologues exhibit different tunneling pathways due to change in symmetry. The symmetry of  $\text{HDO} \cdots \text{HDO}$  allows for Acceptor-Donor Interchange but not for interchanging protons within its donor (bifurcation). The opposite case is true for  $\text{HDO} \cdots \text{D}_2\text{O}$ .

## 6.2.2 Apparatus and Experimental Methods

The experimental setup for dimer formation in a buffer gas cell has been described in detail in the Experimental Apparatus chapter and the previous section. The monomers are introduced via two separate but identical heated pulsed valves, ensuring dimer formation takes place inside the cell. Cold helium buffer gas is continuously flowed into the cell at 4 SCCM, which produces a helium density of  $10^{14}$  molecules  $\cdot$  cm $^{-3}$  inside the cell [185]. The helium buffer gas plays a double role: it thermalizes the water molecules to 7 K via collisions and acts as the third body absorbing the excess kinetic energy required for dimer formation at low temperatures.

For acquiring kinetic data, we collect time-domain spectroscopic data from time zero, up to 80 ms after each monomer valve has fired, as in [185]. Both valves remain open for 7 msecs. Data for the H<sub>2</sub>O  $\cdots$  DOD dimer and its D<sub>2</sub>O monomer are shown in Figure 6.7. We record time-dependent densities for the eight water dimer isotopomers shown in Table 6.2. To ensure reliable comparison between the kinetics of each isotopomer species, we monitor the same  $|1_{01}\rangle - |0_{00}\rangle$  transition for all species. This transition lies within 11-18 GHz range for the seven species, but it is out of the range of our instrument for two of the total isotopomers: D<sub>2</sub>O  $\cdots$  HOH and D<sub>2</sub>O  $\cdots$  HOD, therefore no kinetic data were acquired of these species.[173]

At the same time, we monitor the  $|3_{13}\rangle - |2_{20}\rangle$  D<sub>2</sub>O transition at 10919.227 MHz and the  $|2_{21}\rangle - |2_{20}\rangle$  HDO transition at 10278.25 MHz.[189] The signal strength on these transitions is a useful proxy for extracting concentrations, but is not appropriate for quantitative density measurements because these monomer lines are lines that belong to non-properly thermalized species at 150 K. Accurate temperature profiles within the cell would be required to calibrate these signal strengths to absolute densities, which are in turn a requirement for calculating rate constants for the isotopomer species. Instead,

we chose to use the already reported value of the rate constant for the water dimer available by CRESU experiments. Bourgalais et al. measured a rate constant of  $9.9 \times 10^{-10} \text{ cm}^3 \text{ molecule}^{-1} \text{ s}^{-1}$  at 22.5 K for the water dimer, which we then extrapolated to 10 K using their proposed approximate formula that the rate constant  $k$  is proportional to  $T^{-1/6}$ . [143]

### 6.2.3 Results

Figure 6.7 shows the real-time formation of the  $\text{H}_2\text{O} \cdots \text{DOD}$  dimer inside the buffer gas cell. The two monomers were introduced from two separate valve inputs. The dimer signal (orange) appears 15 ms after the monomer signal (blue) confirming that dimerization occurs inside the cell under cryogenic conditions. We collect similar data for the seven other isotopomers shown in Table 6.2.

The equation describing the relative reaction rates is

$$\frac{d[\text{dimer}]}{dt} = k * [\text{monomer}][\text{monomer}]$$

Where  $k$  is the rate constant. The reaction rate,  $\frac{d[\text{dimer}]}{dt}$  for each species is extracted by performing a linear fit on the rising part of the spectroscopic time data, describing the cold dimer formation. An exponential decay was fit to the decreasing signal portion of the signal versus time data, to extract decay times and study conformational relaxation between the dimers. No evidence of conformational relaxation was observed between the dimers after they are formed.

Table 6.3 shows water dimer isotopologue structures sorted by measured rate constants and Kinetic Isotope Effect (KIE) ratios. Rate constants are calibrated using the measured CRESU value for water dimer formation at extrapolated to 10 K. KIE is defined as the ratio of the rate constant of the isotopomer species divided by the rate constant of



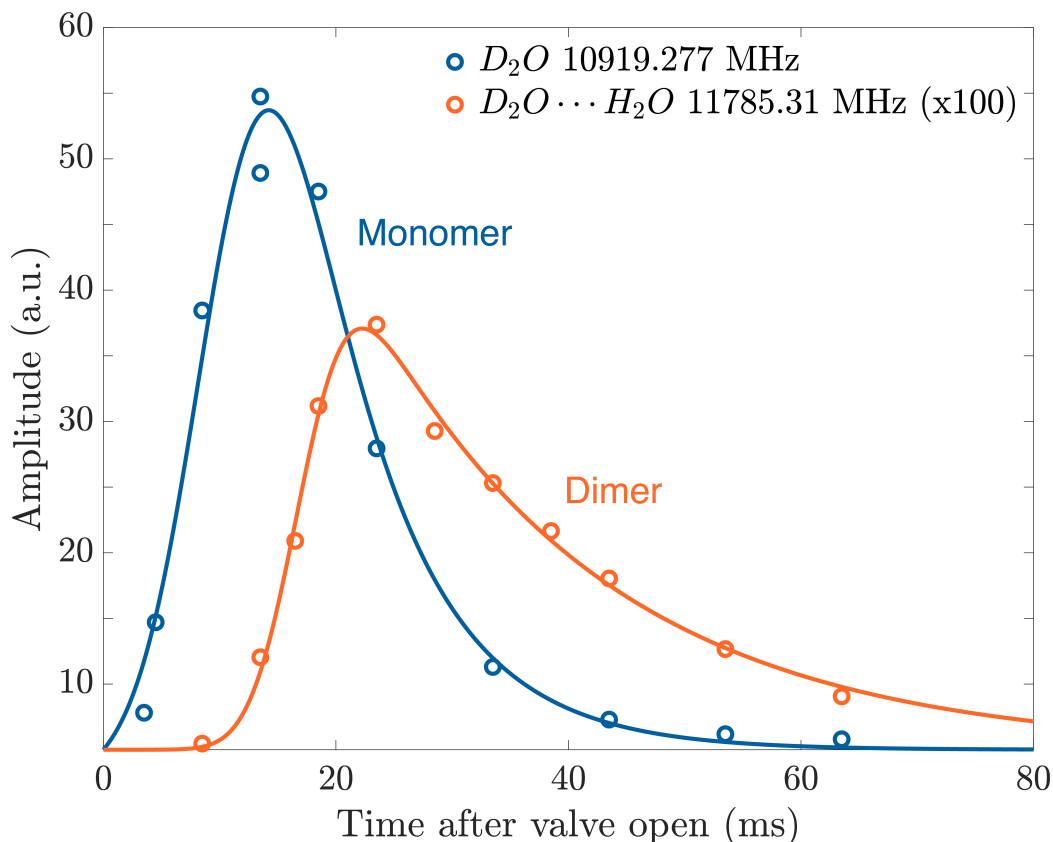


Figure 6.7: Formation of  $D_2O \cdots HOH$  at 10 K. Time-domain spectroscopic data of  $D_2O$  monomer (blue) and the  $D_2O \cdots HOH$  dimer (orange) formed at later times in cryogenic conditions. The rising side of the dimer trace describes its formation kinetics. The decay is governed by diffusion dynamics inside the buffer gas cell.

the water dimer,  $\frac{k_{\text{mixed}}}{k_{(H_2O)_2}}$ . On the right side for the table, we include the type of tunneling mechanism present for each dimer.

We observe that the four mixed isotopologues containing HDO display the slowest rates, with  $(HDO)_2$  forming 72 times slower than  $(H_2O)_2$  and 40 times slower than  $H_2O \cdots DOD$  that has the same number of deuterium atoms. The large (2-72) KIEs suggest that quantum tunnelling plays a significant role in the formation kinetics.

We compare the trends in the reaction rate data with the type and number of tunneling mechanisms of each species. This way, we can deconstruct the water dimer dynamics

Donor		Acceptor		Dimer	Transition
HDO	+	DOH	→	HDO ... DOH	13120.12 MHz
DHO	+	HOH	→	DHO ... HOH	11810.30 MHz
DHO	+	DOD	→	DHO ... DOD	11296.38 MHz
H <sub>2</sub> O	+	DOH	→	H <sub>2</sub> O ... DOH	12239.00 MHz
D <sub>2</sub> O	+	DOH	→	D <sub>2</sub> O ... DOH	11349.75 MHz
H <sub>2</sub> O	+	DOD	→	H <sub>2</sub> O ... DOD	11785.31 MHz
D <sub>2</sub> O	+	DOD	→	D <sub>2</sub> O ... DOD	12036.27 MHz
H <sub>2</sub> O	+	HOH	→	H <sub>2</sub> O ... HOH	12321.00 MHz

Table 6.2: List of the eight isotopologues of the water dimer formed inside the buffer gas cell with corresponding microwave transitions. In our notation, the first monomer always refers to hydrogen-bond donor and the latter one to the hydrogen-bond acceptor.

into contributions of individual tunneling motions.

We observe that lowering the symmetry removes tunneling permutations, since H and D are not equivalent. (HDO)<sub>2</sub> cannot bifurcate (proton donor interchange) while the two isomers of H<sub>2</sub>O ... DOH and D<sub>2</sub>O ... DOH cannot tunnel between donor and acceptor (donor-acceptor interchange). The (H<sub>2</sub>O)<sub>2</sub>, (D<sub>2</sub>O)<sub>2</sub> dimers possess all three tunneling mechanisms.[180]

Dimers with HDO monomers form significantly slower than the rest. The trend goes with (HDO)<sub>2</sub> being the slowest, followed by dimers with HDO as an acceptor and then the dimers with HDO as the hydrogen bond donor, being the fastest mixed isotopologues. Higher symmetry of the product leads to faster formation rates.

One can also compare any species, one substitution at a time. Starting from the water dimer, we see that substituting one hydrogen of the donor H<sub>2</sub>O ... DOH with D, decreases the rate a factor of 3.5, while substituting one hydrogen of the acceptor HDO ... HOH causes a 20-fold decrease. This trend persists when comparing more species as well: H<sub>2</sub>O ... DOD (85) with HDO ... DOD (13) and H<sub>2</sub>O ... DOH (43) and the D<sub>2</sub>O ... DOD equivalent substitutions.

Donor-acceptor interchange and proton donor interchange both disrupt the hydrogen

bond, thus slowing down dimer formation compared to species such as  $\text{H}_2\text{O} \cdots \text{DOH}$  and  $\text{D}_2\text{O} \cdots \text{DOH}$  that only display the methyl amine type. However, in species with higher symmetry, especially in the acceptor, faster formation as seen for the  $\text{H}_2\text{O} \cdots \text{DOD}$  case might be the result of more complex, currently unexplored theoretically, mechanisms such as coupling between pathways. No obvious trend was observed for the number of available tunneling states or the number of deuterium atoms.

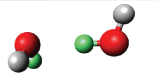
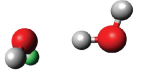
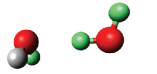
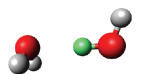
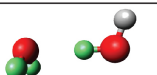
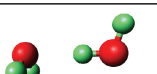
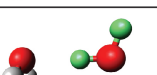
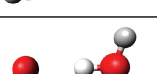
Molecule		Kinetic Isotope Effect Relative to $(\text{H}_2\text{O})_2$	Rate Constant ( $\times 10^{-10}/\text{s}$ )	Tunneling Pathway		
Acceptor $\cdots$ Donor	Donor-acceptor Interchange			Proton Donor Interchange	Methyl Amine	
 $\text{HDO} \cdots \text{DOH}$	72	2	✓		✓	
 $\text{HDO} \cdots \text{HOH}$	20	7		✓	✓	
 $\text{HDO} \cdots \text{DOD}$	11	13		✓	✓	
 $\text{H}_2\text{O} \cdots \text{DOH}$	3.4	43			✓	
 $\text{D}_2\text{O} \cdots \text{DOH}$	3.4	43			✓	
 $\text{D}_2\text{O} \cdots \text{D}_2\text{O}$	2.1	67	✓	✓	✓	
 $\text{H}_2\text{O} \cdots \text{DOD}$	1.6	85		✓	✓	
 $\text{H}_2\text{O} \cdots \text{H}_2\text{O}$	1.0	144	✓	✓	✓	

Table 6.3: Water dimer isotopologue experimental rate constants and Kinetic Isotope Effects (KIEs) at 10 K as a function of the three main water dimer tunneling pathways. By selectively substituting specific atoms, we deconstruct low temperature water dimerization into contributions of individual tunneling motions.

## 6.2.4 Conclusion

We present a spectroscopic low-temperature kinetic study of the water dimer and seven of its isotopologues formed in real-time inside a cryogenic buffer gas cell. We extract dimer formation rates and calculate the kinetic isotope effects for all species. This is a new approach on studying the kinetics via a quantum tunneling lens, providing specific insights on how tunneling motions participate in the dynamics. Formation rate trends show a dependence on the symmetry and tunneling pathways of the hydrogen bond acceptor or donor atoms. The broad isotopic study allows for deconstruction of the water dimer dynamics to the effects of individual tunneling motions, providing a new approach on studying low temperature quantum effects in water and other van der Waals complexes. This method offers a solution that complements the challenges encountered by performing isotopic studies using the CRESU method, allowing for new directions in studying low temperature kinetics.

# Chapter 7

## Future Directions

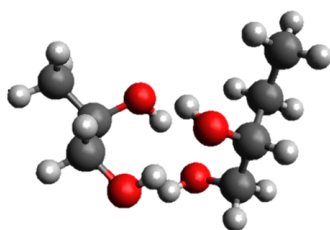
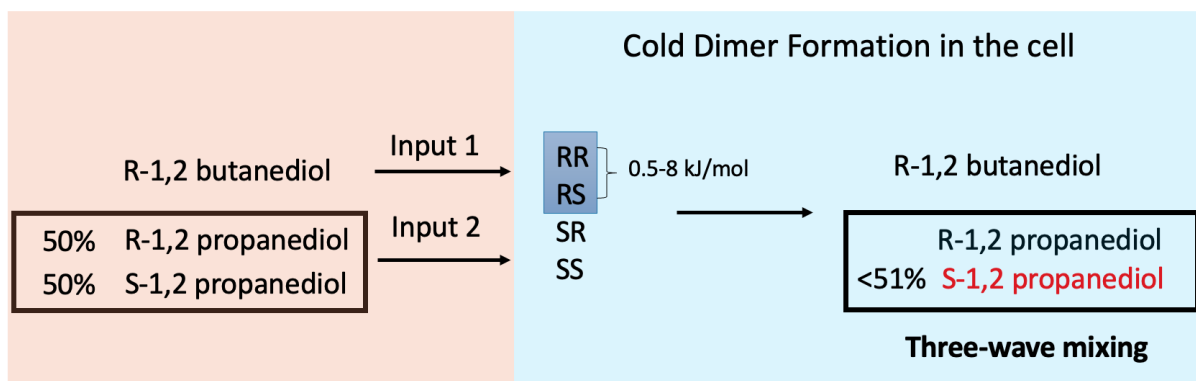
### 7.1 Towards the observation of chiral imprinting via M3WM

It would be very interesting to combine our recent results of dimer formation inside the buffer gas cell and the chiral detection capabilities of the three-wave mixing experiments by forming dimers from chiral monomers in the cell. This way, we could try to measure induced enantiomeric excess as a result of dimerization.

For instance, if we use one valve to introduce a chiral molecule such as 1,2-butanediol in enantiomeric excess and the second valve to introduce a chiral molecule such as 1,2-propanediol as a racemate we could observe chiral recognition effects, via the schematic shown in Figure 7.1. Chiral recognition due to van der Waals interaction leads to differences in the energetics of homochiral and heterochiral dimers. Many studies in vibrational and microwave spectroscopy have measured such differences but there has not yet been a direct chirality measurement to such system.[190, 191, 192, 193] For a system such as the 1,2-propanediol-1,2 butanediol one, we could expect that due to chiral recognition

effects either the homodimer or the heterodimer will be preferentially produced at 6 K. As a result, the species started in racemic form will eventually acquire small enantiomeric excess due to dimerization effects. Then, we can use M3WM to observe that induced excess in the cell.

For this experiment, we have successfully coupled a multiple input source for dimer formation with the three-wave mixing buffer gas cell, as shown in Figure 7.2 The two inputs enter the cell in an angled manner (12 degrees) for increased interaction volume. Two chiral molecules, one in enantiopure form and one in racemic form will be introduced at the same time but through different inputs inside the buffer gas cell. Dimer formation from chiral monomers would lead to the formation of RR, RS, SS and SR diastereomers. In chiral recognition cases, RR or RS dimer could be favored energetically between 0.5-2 kJ/mol. We believe for energy differences above 500 K, there will be preferential production of the favored species at 7K. Then, the species starting as a racemate would be consumed unevenly resulting to a non-zero induced enantiomeric excess that we are planning to measure using microwave three-wave mixing.



**R-1,2 propanediol-R-1,2 butanediol dimer**

Figure 7.1: Two chiral molecules, one in enantiopure form and one in racemic form will be introduced at the same time but through different inputs inside the buffer gas cell. Dimer formation from chiral monomers would lead to the formation of RR, RS, SS and SR diastereomers. In chiral recognition cases, RR or RS dimer could be favored energetically between 0.5-2 kJ/mol. We believe for energy differences above 500 K, there will be preferential production of the favored species at 7K. Then, the species starting as a racemate would be consumed unevenly resulting to a non-zero induced enantiomeric excess that we are planning to measure using microwave three-wave mixing.

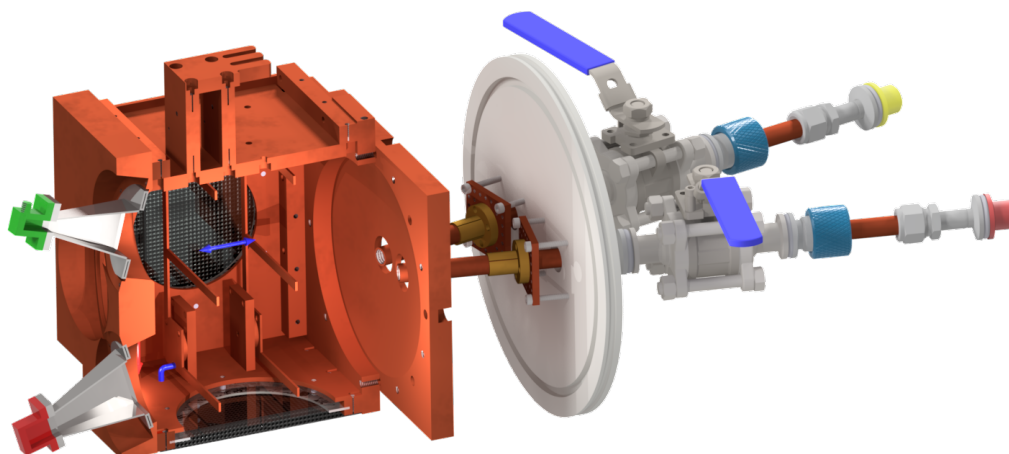


Figure 7.2: CAD design of the experimental apparatus for measuring induced enantiomeric excess from dimer formation inside the buffer gas cell. We have coupled the multiple input source for dimer formation along with the buffer gas cell design optimized for microwave three-wave mixing experiments. The two inputs enter the cell in an angled manner (12 degrees) for increased interaction volume.



## 7.2 Studying Radical species in the buffer gas cell

Two-thirds of the neutral species detected in cold environments, such as the interstellar medium and dark clouds, are open-shell radicals. Radical species are highly reactive due to their unpaired electrons. The past decades, many small molecular radical species have been identified to play key roles in the synthetic pathways to complex organic molecules in such environments.[194, 195]

Many molecule + radical reactions have no activation barrier to form products. These types of reactions have been studied extensively the past years and provide great frameworks for studying the fundamentals of cold chemistry. In all of those experiments, the radical species are ions and not neutrals. Mass spectrometry has been routinely used as a diagnostics tool for synthetic chemists. The resulting ion fragments, which can be closed shell ionized molecules, or radical cations/anions provide clues for the mechanism of a reaction. However, for each fragmentation reaction there is the equivalent neutral radical produced that is invisible to the ion detector that could provide much more conclusive mechanistic insights.

This chapter describes our preliminary efforts in studying neutral radical species in a cryogenic buffer gas cell. This capability can open up many interesting future studies such as:

1. the exploration of the kinetics of radical + molecule reactions in the gas phase such as terpene oxidation by OH radicals in the troposphere.
2. the study of barrierless radical reactions relevant to astrochemistry at 10 K, such as vinyl cyanide and the  $\beta$ -cyanovinyl radical (HCCHCN,  $\beta$ -CV) forming pyridine.  
[196]
3. the investigation of interstellar molecule formation such as the production of ben-

zonitrile from the benzene + CN radical.[195]

4. exploring capabilities of neutral radicals as sensitive probes for effects such as forbidden transitions or parity-violation studies.

Microwave spectroscopy has been used extensively for identifying radical species and study their structure [197, 198, 199]. Our goal is to combine this capability with the advantages of buffer gas cooling. We are interested in exploring the kinetics of radical + molecule reaction in the gas phase, similar to our dimer formation experiments. Also, we were particularly interested in producing and detecting chiral radicals in the gas-phase, providing the first tool that can measure % enantiomeric excess in those species.

### 7.2.1 Experimental design

One of the main challenge of radical studies in the buffer gas cell is the production of radical species in high enough densities for spectroscopic detection. Radical species in molecular beam experiments are usually produced via discharge or pyrolysis. We attempted both methods and present preliminary results.

#### Radical pyrolysis setup

The main design for the pyrolysis setup was inspired by the pyrolysis source used by Zwier et al.[197, 198] For the first prototype, we focused on adapting a simple version of the design to the requirements of our apparatus that operates under cryogenic conditions.

As seen in Figure 7.3, our standard copper tube goes into an induction coil for heating before the cell aperture. Inside the copper tube, there is a 4" inch quartz tubing and at the edge of the tube, near the exit, there is a 2" cast iron sleeve. The choice of materials is very important, and very informative videos of how each material reacts to inductive heating can be found at Himmerlwerk's website [200]. Cast iron was selected for our

heating sleeve because it is magnetic and heating via induction takes place much more rapidly than it occurs in copper. This way we can heat up the sleeve up to 1500 K while minimizing heatloads which is one of the main concerns of running a pyrolysis source by the cryogenic cell at 6 K. Quartz was selected for its chemical inertness to minimize radicals reacting with the tube walls. The steel sleeve was doubly wrapped with high temperature wrap sleeving (Mica/Silicone rubber blend, 6811A21, McMaster) that can withstand temperatures up to 1500 K. For additional temperature shielding, the coil was placed inside an aluminum cylindrical radiation shield that was further wrapped with ceramic fiber tape (87575K88, McMaster). Alumina oxide ceramic fiber has the lowest heat-flow rate of all the ceramic fiber materials. Thermal crayons 230-730 °C were used for initial testing and troubleshooting. A type K thermocouple was used to monitor the temperature of the experiment while in vacuum.

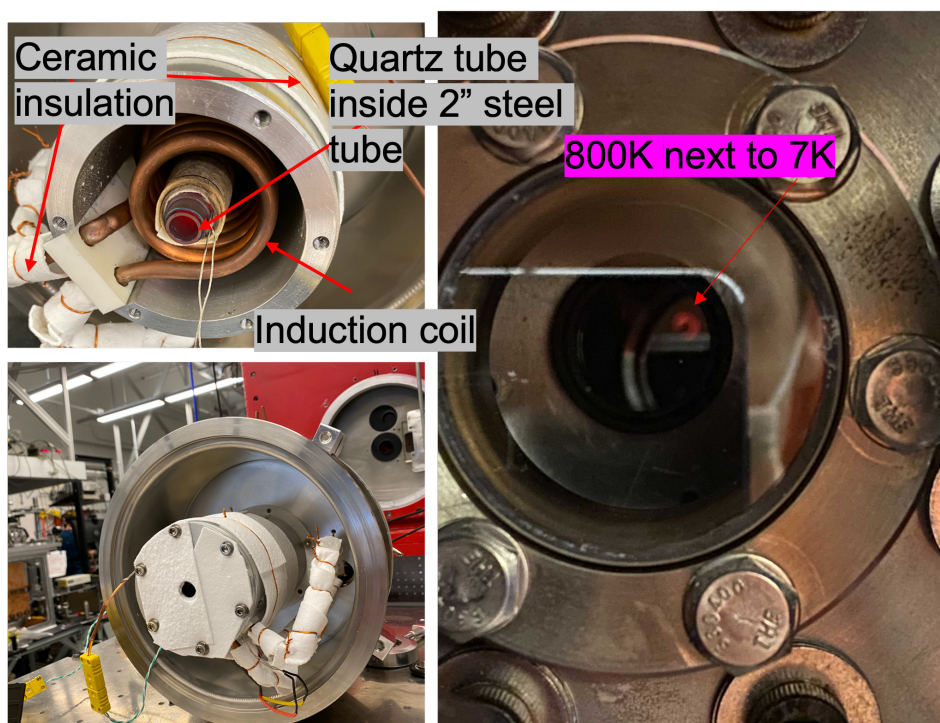


Figure 7.3: Custom-built cryogenic-friendly pyrolysis setup. The copper tube goes into an induction coil for heating before the cell aperture. Inside the copper tube, there is a 4" inch quartz tubing and at the edge of the tube, near the exit, there is a 2" cast iron sleeve. The steel sleeve was doubly wrapped with high temperature wrap sleeving that can withstand temperatures up to 1500 K. For additional temperature shielding, the coil was placed inside an aluminum cylindrical radiation shield that was further wrapped with ceramic fiber tape. A type K thermocouple was used to monitor the temperature of the experiment while in vacuum.

## Pyrolysis results and discussion

During our first attempts with the pyrolysis setup, we tried to detect 2-furanyloxy or phenoxy radicals, which are two radical species with well documented microwave transitions at certain pyrolysis temperatures. [198, 197]

We attempted to produce 2-furanyloxy with 2-methoxyfuran as the precursor, aiming to see the product around 620 K which was within the setup's pyrolysis capabilities. We also attempted to see phenoxy radical from phenyl allyl ether (PAE) which should show optimal radical signal at 850 K. Both efforts did not succeed. In both cases, the difference in spectra with pyrolysis on and pyrolysis off did not produce any conclusive data.

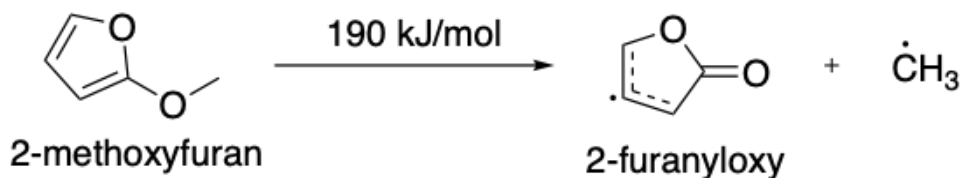


Figure 7.4: Pyrolysis reaction of 2-methoxyfuran producing 2-furanyloxy and methyl radicals.

It is entirely possible that the species were present but we did not have the sensitivity to detect them. Radical species, because of their unpaired electron, exhibit Zeeman splittings due to Earth's magnetic field which raise the sensitivity requirements necessary for detection. Higher sensitivity is also needed for a second reason, the concentration of the radicals produced is much lower ( $\leq 1$  percent) than standard samples.

Figure 7.5 points towards potential issues of the current design that could further improved. There are always issues with working with solid precursors, which get vaporized but end up freezing on the walls or the coldest part of the tube. Also, as seen on the right, after an experiment we noticed that the quartz tube was burnt on the side closer to the coil, away from the aperture. Both clues suggest issues with temperature homogeneity. It is unclear if radical species produced at one side of the tube, would actually survive

all the way to the cell.

The current setup took 15 mins to reach 715 K and was held there continuously. A future design with a gated power supply that can apply high temperature in a pulsed manner for milliseconds or seconds could potentially produce high density radicals that survive and reach the buffer gas cell. A pulsed valve could also be coupled to the setup. A few challenges with that are that Parker 9 series valves can only withstand temperatures up to 355 K max and struggle to produce large enough gas sample densities from solid samples.

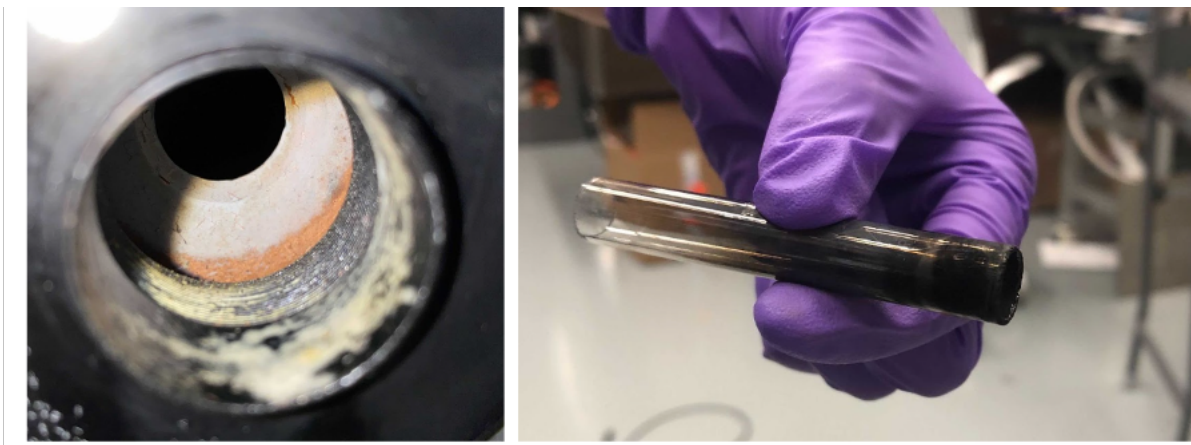


Figure 7.5: (left) Solid sample of cinnamyl alcohol deposited on the surface before entering the buffer gas cell. (right) Quartz tube after running the pyrolysis setup.

## 7.2.2 Pulsed discharge setup

We also attempted to produce radical species using a pulsed discharge setup, initially designed by the McCarthy Group (Harvard-Smithsonian Center for Astrophysics). Precursor sample in the gas-phase is being introduced through a Parker 9 series valve, passes through a copper disc, electrically insulated by G10/Delrin parts and sleeve, as seen in Figure 7.6. Delrin is a type of plastic that is an excellent high voltage insulator. Heaters are attached at two places for uniform heating. The Parker 9 Series valve can withstand maximum temperatures up to 80°C. The copper disc is connected to a DC voltage supply that can operate up to 2000 V in both polarities.



Figure 7.6: Pulsed discharge design for radical production. Precursor sample in the gas-phase is being introduced through a Parker 9 series valve, which passes through a copper disc that is electrically insulated from the rest of the valve. The copper disc is connected to a DC voltage supply and can operate up to 2000 V in both polarities.

With this setup, we successfully detected cyclopropenylidene ( $C_3H_2$ ) and OH radicals. Methyl acetylene was used as a precursor for the cyclopropenylidene radical and water was used as the precursor for the OH radical. The setup was operated at -2100 V. As seen in Figure 7.7, we saw the  $J = 7/2$ ,  $F = 3 \rightarrow F = 3$  and  $F = 4 \rightarrow F = 4$  hyperfine transitions of OH radical with center frequencies at 13434.62 MHz and 13441.36

MHz, respectively.[201] However, we still have not been able to detect larger resonance-stabilized radicals such as phenoxy in the buffer gas cell but the OH and ( $C_3H_2$ ) radical measurements prove that buffer gas cell conditions can be used for radical studies.



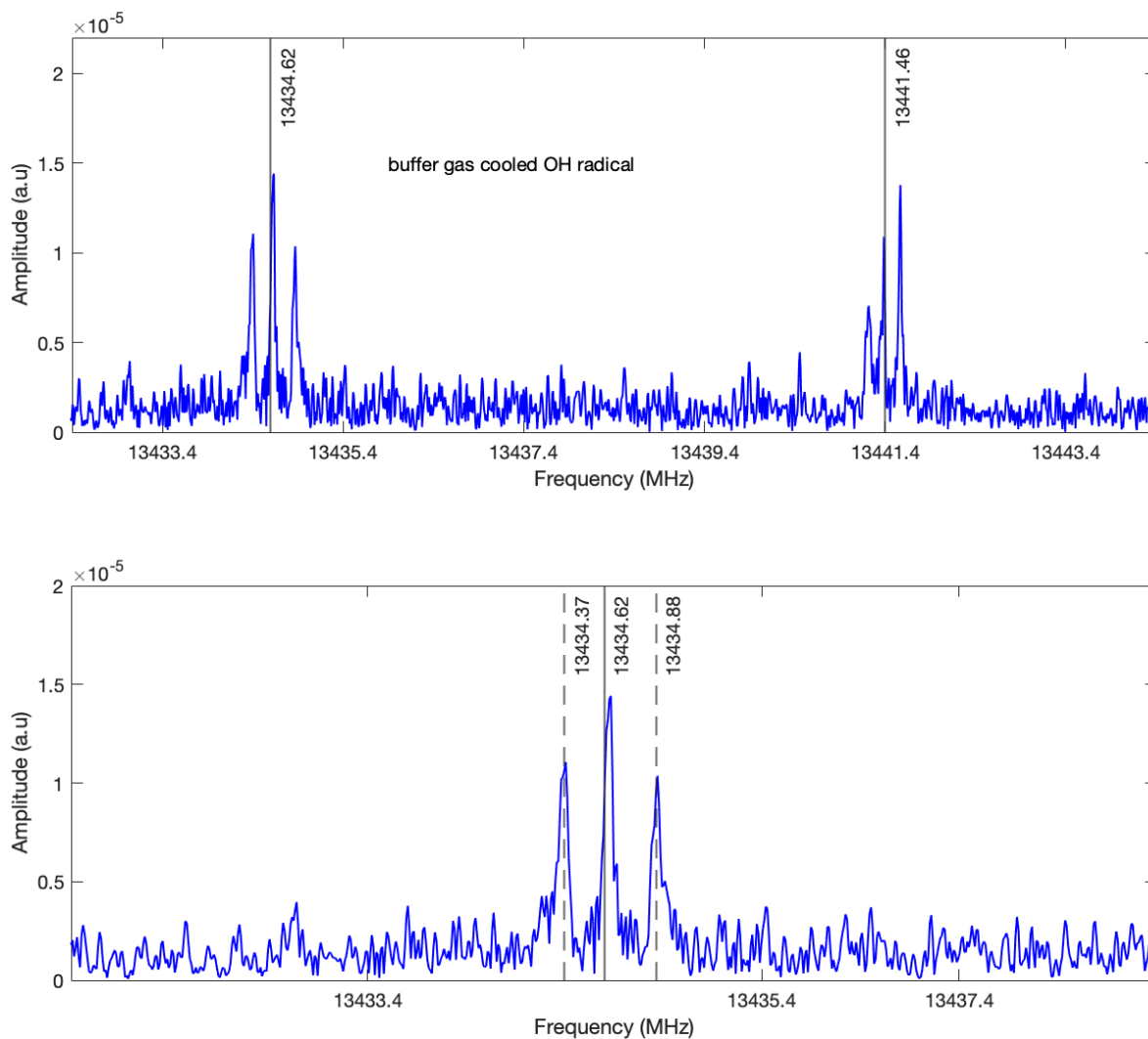


Figure 7.7: (top) Experimental microwave transitions of buffer-gas cooled OH radicals. These are the  $J = 7/2$ ,  $F = 3 \rightarrow F = 3$  and  $F = 4 \rightarrow F = 4$  hyperfine transitions. The structure is caused by Earth's magnetic field.(bottom) Zoomed-in portion of top figure, magnetic structure of the transition is highlighted.

### 7.2.3 Formation of gas-phase chiral radicals

Chiral radicals are molecules with an unpaired electron and a stereogenic center. Even though chiral radical compounds are common intermediates in asymmetric synthetic mechanistic pathways [202], there is very limited literature on experimental studies and properties of chiral radicals. Dreiling et al. studied the production of the bromocamphor radical via dissociative electron detachment[203, 96]. However, most spectroscopic experimental efforts feature resonance-stabilized radicals, and as a result there is currently no established method for producing high density chiral radical species for spectroscopic detection or any microwave spectroscopy study of such species.

Given our previously successful efforts in producing OH radicals and our double-input capabilities, one way to produce chiral species is OH radical initiated terpene oxidation. For example, as seen in [204, 205] the first step of  $\beta$ - or  $\alpha$ -pinene oxidation with OH radical results in chiral radical species. Another possible route could be using bromocamphor or bromo-1,2-propanediol as starting materials and use an ablation setup to break the C-Br bond, where the unpaired electron and stereogenic carbon are at different carbon atoms.

## 7.3 Singlet-oxygen barrierless photooxidations in a buffer gas cell

Singlet oxygen ( $^1\text{O}_2$ ) is an important intermediate in many photochemical and photo-biological processes and is one of the products of UV photolysis of  $\text{O}_3$  in the atmosphere.[206, 207, 208] Due to its high reactivity,  $^1\text{O}_2$  could be an interesting potential candidate for studying cold chemistry reactions under cold conditions that have chemical or biological significance. Some great examples are the barrierless reactions of  $^1\text{O}_2$  with biomolecules such as guanine and histidine or biological precursors such as aniline.[209, 210].  $^1\text{O}_2$  could also be used for studying for the first time, key chemical reactions such as the Diels–Alder and ene ones at cold conditions. [211]

Similar to the dimer formation experiments, the two reactants will be introduced inside the cell via two separate inputs. This means that the first experimental requirement is the design and testing of a robust method for the production and detection of singlet oxygen ( $^1\text{O}_2$ ) that can be integrated to the buffer gas cell. In this section, I discuss our preliminary attempts for such process.

### 7.3.1 Preliminary production and detection setup

There are two main methods for the gas-phase generation of ( $^1\text{O}_2$ ), a) via a microwave discharge of ( $^3\text{O}_2$ ) and b) via the quenching of the triplet state of sensitizers, as seen in Eq. 7.1.[212, 208, 213] More specifically, we explored the idea behind using sensitizers while synthesizing endoperoxides, as seen in Figure 7.8. Endoperoxides can be easily transported and introduced into the cell and then release ( $^1\text{O}_2$ ) upon gently heating around 30-60 °C.

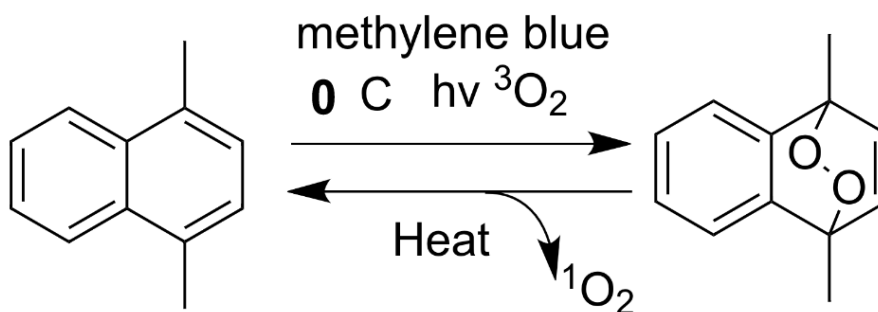
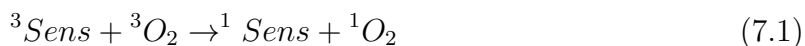


Figure 7.8: Endoperoxide reaction scheme for singlet oxygen precursor.

The synthetic scheme was adapted from Refs.[212, 214] and it was chosen because it is a one-pot simple synthetic route that only requires light, oxygen gas, and a sensitizer. Common sensitizers are dyes such as tetraphenylporphyrin (TPP), rose bengal (RB), and methylene blue (MB). In our case, we used methylene blue:

In a round bottom flask, we added 5mL of dichloromethane (DCM), 0.15mL of 1,4-Dimethylnaphthalene (1,4DMN) and 2mg of methylene blue (MB). The flask was sealed with a rubber septum. The mixture was placed in an ice bath with the solution exposed to a 625 watt quartz-iodine lamp. We bubble  $\text{O}_2$  via long lore lock needle plug into the septum at 4psi for 24 hours. Another needle was used to prevent overpressuring the flask while adding  $\text{O}_2$  gas. As the product starts forming, the solution changes color from bright blue (color of MB) to teal-green blue color. Final endoperoxide product formation was confirmed by NMR spectroscopy.

The detection setup was based on singlet oxygen  ${}^1\text{O}_2$  luminescence at 1270 nm [215]. The setup can be seen in Figure 7.9. A mixture of the unpurified product (after DCM was evaporated for safety reasons) was dissolved in acetone and injected into the vacuum setup. After pumping all acetone, we apply heat via a heat gun while monitoring the

pressure inside the vessel and the output of Ge photodiode (PDA30B2, 800-1800 nm, Thorlabs). While heating up to 40 °C, we see a DC voltage increase out of the photodiode (right part of Figure 7.9), confirming the method was successful in producing amounts of singlet oxygen after gentle heating of the endoperoxide. Next steps would be to optimize density and integrate the detection setup to the buffer gas cell.

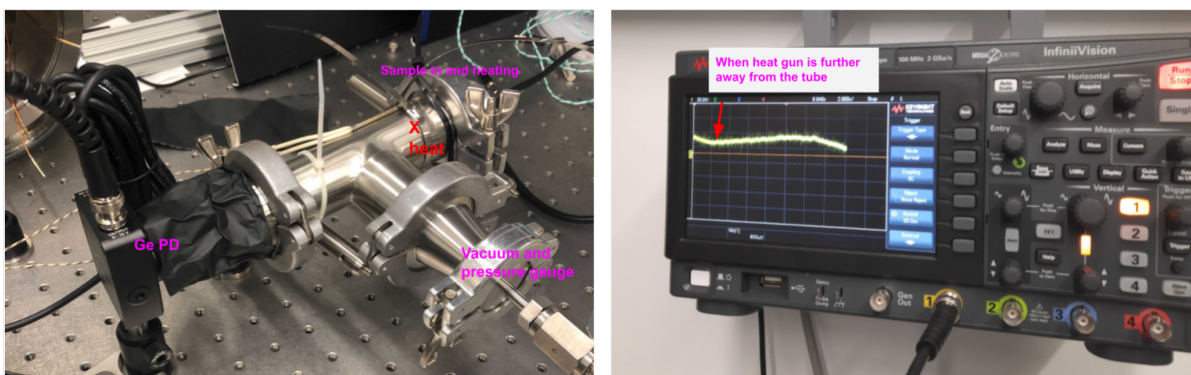


Figure 7.9: (left)  $^1\text{O}_2$  Detection setup for luminiscense at 1270 nm. (right) Signal monitoring out of Ge photodiode, showing a voltage increase upon heating the endoperoxide sample.

# Bibliography

- [1] Walther Caminati and Jens-Uwe Grabow. Advancements in microwave spectroscopy. In *Frontiers and Advances in Molecular Spectroscopy*, pages 569–598. Elsevier, 2018.
- [2] David Patterson, Melanie Schnell, and John M Doyle. Enantiomer-specific detection of chiral molecules via microwave spectroscopy. *Nature*, 497(7450):475–477, 2013.
- [3] Simon Lobsiger, Cristobal Perez, Luca Evangelisti, Kevin K Lehmann, and Brooks H Pate. Molecular structure and chirality detection by fourier transform microwave spectroscopy. *The journal of physical chemistry letters*, 6(1):196–200, 2015.
- [4] V Alvin Shubert, David Schmitz, David Patterson, John M Doyle, and Melanie Schnell. Identifying enantiomers in mixtures of chiral molecules with broadband microwave spectroscopy. *Angewandte Chemie International Edition*, 53(4):1152–1155, 2014.
- [5] V Alvin Shubert, David Schmitz, Cristóbal Pérez, Chris Medcraft, Anna Krin, Sérgio R Domingos, David Patterson, and Melanie Schnell. Chiral analysis using broadband rotational spectroscopy. *The journal of physical chemistry letters*, 7(2):341–350, 2016.
- [6] Sérgio R Domingos, Cristóbal Pérez, and Melanie Schnell. Sensing chirality with rotational spectroscopy. *Annual review of physical chemistry*, 69:499–519, 2018.
- [7] María Mar Quesada-Moreno, Anna Krin, and Melanie Schnell. Analysis of thyme essential oils using gas-phase broadband rotational spectroscopy. *Physical Chemistry Chemical Physics*, 21(48):26569–26579, 2019.
- [8] Garrett K Drayna, Christian Hallas, Kenneth Wang, Sergio R Domingos, Sandra Eibenberger, John M Doyle, and David Patterson. Direct time-domain observation of conformational relaxation in gas-phase cold collisions. *Angewandte Chemie International Edition*, 55(16):4957–4961, 2016.

- [9] Weixing Li, Cristóbal Pérez, Amanda L Steber, Melanie Schnell, Dingding Lv, Guanjun Wang, Xiaoqing Zeng, and Mingfei Zhou. Evolution of solute–water interactions in the benzaldehyde-(h<sub>2</sub>o) 1–6 clusters by rotational spectroscopy. *Journal of the American Chemical Society*, 2023.
- [10] Jeremy O Richardson, Cristóbal Pérez, Simon Lobsiger, Adam A Reid, Berhane Temelso, George C Shields, Zbigniew Kisiel, David J Wales, Brooks H Pate, and Stuart C Althorpe. Concerted hydrogen-bond breaking by quantum tunneling in the water hexamer prism. *Science*, 351(6279):1310–1313, 2016.
- [11] Fan Xie, Nathan A Seifert, Arsh S Hazrah, Wolfgang Jäger, and Yunjie Xu. Conformational landscape, chirality recognition and chiral analyses: Rotational spectroscopy of tetrahydro-2-furoic acid propylene oxide conformers. *ChemPhysChem*, 22(5):455–460, 2021.
- [12] J Paul I Hearn, Rachel V Cogley, and Brian J Howard. High-resolution spectroscopy of induced chiral dimers: A study of the dimers of ethanol by fourier transform microwave spectroscopy. *The Journal of chemical physics*, 123(13):134324, 2005.
- [13] Daniel R Willey, DN Bittner, and Frank C De Lucia. Pressure broadening cross sections for the h<sub>2</sub>s he system in the temperature region between 4.3 and 1.8 k. *Journal of Molecular Spectroscopy*, 134(1):240–242, 1989.
- [14] Julia Piskorski, David Patterson, Sandra Eibenberger, and John M Doyle. Cooling, spectroscopy and non-sticking of trans-stilbene and nile red. *ChemPhysChem*, 15(17):3800–3804, 2014.
- [15] P Bryan Changala, Marissa L Weichman, Kevin F Lee, Martin E Fermann, and Jun Ye. Rovibrational quantum state resolution of the c<sub>60</sub> fullerene. *Science*, 363(6422):49–54, 2019.
- [16] Sean K Tokunaga, RJ Hendricks, MR Tarbutt, and B Darquié. High-resolution mid-infrared spectroscopy of buffer-gas-cooled methyltrioxorhenium molecules. *New Journal of Physics*, 19(5):053006, 2017.
- [17] Jessica P Porterfield, Lincoln Satterthwaite, Sandra Eibenberger, David Patterson, and Michael C McCarthy. High sensitivity microwave spectroscopy in a cryogenic buffer gas cell. *Review of Scientific Instruments*, 90(5):053104, 2019.
- [18] L Satterthwaite, G Koumarianou, PB Carroll, R Sedlik, I Wang, and D Patterson. Low-temperature gas-phase kinetics of ethanol-methanol heterodimer formation. *Journal of Physical Chemistry A (submitted)*, X(X):XXXX, 2023.
- [19] Albert G Tobin, Douglas W Sedgley, Thomas H Batzer, and Wayne R Call. Evaluation of charcoal sorbents for helium cryopumping in fusion reactors. *Journal*

## BIBLIOGRAPHY

---

- of Vacuum Science & Technology A: Vacuum, Surfaces, and Films*, 5(1):101–105, 1987.
- [20] David Patterson and John M Doyle. Cooling molecules in a cell for ftmw spectroscopy. *Molecular Physics*, 110(15-16):1757–1766, 2012.
- [21] Peter Morgan. Gas chromatography liner selection guide, thermofisher, uk. [https://www.separatedbyexperience.com/documents/Liner\\_Selection\\_Guide.pdf](https://www.separatedbyexperience.com/documents/Liner_Selection_Guide.pdf).
- [22] Jaap de Zeeuw. Why use glass/quartz wool in splitted injection liners? <https://www.restek.com/en/chromablography/chromablography/why-use-glassquartz-wool-in-splitted-injection-liners/>.
- [23] Jonas Bonn. *Improved Techniques for Sampling and Sample Introduction in Gas Chromatography*. PhD thesis, School of Chemical Science and Engineering Department of Chemistry, Division of Analytical Chemistry.
- [24] Dr. Konrad Grob. Sample evaporation in hot gc injectors. <https://www.restek.com/en/technical-literature-library/articles/sample-evaporation-in-hot-GC-injectors/>.
- [25] Jonas Bonn, Johan Redeby, and Johan Roeraade. Electrostatic sample nebulization for improved sample vaporization in the split/splitless gas chromatography inlet. *Analytical chemistry*, 81(13):5327–5332, 2009.
- [26] Andres F Ordonez and Olga Smirnova. Generalized perspective on chiral measurements without magnetic interactions. *Physical Review A*, 98(6):063428, 2018.
- [27] Maurice HM Janssen and Ivan Powis. Detecting chirality in molecules by imaging photoelectron circular dichroism. *Physical Chemistry Chemical Physics*, 16(3):856–871, 2014.
- [28] Ivan Powis. Photoelectron circular dichroism of the randomly oriented chiral molecules glyceraldehyde and lactic acid. *The Journal of Chemical Physics*, 112(1):301–310, 2000.
- [29] Eizi Hirota. Triple resonance for a three-level system of a chiral molecule. *Proceedings of the Japan Academy, Series B*, 88(3):120–128, 2012.
- [30] David Patterson and John M Doyle. Sensitive chiral analysis via microwave three-wave mixing. *Physical Review Letters*, 111(2):023008, 2013.
- [31] Walter Gordy, Robert L Cook, and Arnold Weissberger. *Microwave molecular spectra*, volume 18. Wiley New York, 1984.



## BIBLIOGRAPHY

---

- [32] Jens-Uwe Grabow. Fourier transform microwave spectroscopy: handedness caught by rotational coherence. *Angewandte Chemie (International ed. in English)*, 52(45):11698–11700, 2013.
- [33] Sandra Eibenberger, John Doyle, and David Patterson. Enantiomer-specific state transfer of chiral molecules. *Physical review letters*, 118(12):123002, 2017.
- [34] Cristóbal Pérez, Amanda L Steber, Sérgio R Domingos, Anna Krin, David Schmitz, and Melanie Schnell. Coherent enantiomer-selective population enrichment using tailored microwave fields. *Angewandte Chemie International Edition*, 56(41):12512–12517, 2017.
- [35] Nicole T Moon, Klaus Woelk, and Garry S Grubbs. Construction and demonstration of a 6–18 ghz microwave three-wave mixing experiment using multiple synchronized arbitrary waveform generators. *Symmetry*, 14(5):848, 2022.
- [36] A Comby, E Bloch, CMM Bond, D Descamps, J Miles, S Petit, S Rozen, JB Greenwood, V Blanchet, and Y Mairesse. Real-time determination of enantiomeric and isomeric content using photoelectron elliptical dichroism. *Nature communications*, 9(1):1–14, 2018.
- [37] Jessica S Creamer, Maria F Mora, and Peter A Willis. Enhanced resolution of chiral amino acids with capillary electrophoresis for biosignature detection in extraterrestrial samples. *Analytical chemistry*, 89(2):1329–1337, 2017.
- [38] Maria F Mora, Florian Kehl, Eric Tavares da Costa, Nathan Bramall, and Peter A Willis. Fully automated microchip electrophoresis analyzer for potential life detection missions. *Analytical Chemistry*, 92(19):12959–12966, 2020.
- [39] Yanchuan Zhao and Timothy M Swager. Simultaneous chirality sensing of multiple amines by 19f nmr. *Journal of the American Chemical Society*, 137(9):3221–3224, 2015.
- [40] Mohammad M Rafiee Fanood, N Bhargava Ram, C Stefan Lehmann, Ivan Powis, and Maurice HM Janssen. Enantiomer-specific analysis of multi-component mixtures by correlated electron imaging–ion mass spectrometry. *Nature communications*, 6(1):1–8, 2015.
- [41] Márcio S Silva. Recent advances in multinuclear nmr spectroscopy for chiral recognition of organic compounds. *Molecules*, 22(2):247, 2017.
- [42] Dimitris Sofikitis, Lykourgos Bougas, Georgios E Katsoprinakis, Alexandros K Spiliotis, Benoit Loppinet, and T Peter Rakitzis. Evanescent-wave and ambient chiral sensing by signal-reversing cavity ringdown polarimetry. *Nature*, 514(7520):76–79, 2014.

- [43] Jim C Visschers, Oleg Tretiak, Dmitry Budker, and Lykourgos Bougas. Continuous-wave cavity ring-down polarimetry. *The Journal of chemical physics*, 152(16):164202, 2020.
- [44] AK Spiliotis, M Xygkis, E Klironomou, E Kardamaki, GK Boulogiannis, GE Katsoprinakis, D Sofikitis, and TP Rakitzis. Gas-phase optical activity measurements using a compact cavity ringdown polarimeter. *Laser Physics*, 30(7):075602, 2020.
- [45] Antoine Comby, Caoimhe MM Bond, Etienne Bloch, Dominique Descamps, Baptiste Fabre, Stephane Petit, Yann Mairesse, Jason B Greenwood, and Valérie Blanchet. Using photoelectron elliptical dichroism (peeld) to determine real-time variation of enantiomeric excess. *Chirality*, 32(10):1225–1233, 2020.
- [46] Hassan Ganjitarbar, Rim Hadidi, Gustavo A Garcia, Laurent Nahon, and Ivan Powis. Vibrationally-resolved photoelectron spectroscopy and photoelectron circular dichroism of bicyclic monoterpene enantiomers. *Journal of Molecular Spectroscopy*, 353:11–19, 2018.
- [47] Tao Wu, Guojie Li, Josef Kapitan, Jiří Kessler, Yunjie Xu, and Petr Bouř. Two spectroscopies in one: Interference of circular dichroism and raman optical activity. *Angewandte Chemie*, 132(49):22079–22082, 2020.
- [48] Georg Westphal, Johannes Wega, Rasika EA Dissanayake, and Tim Schäfer. Chirality detection of surface desorption products using photoelectron circular dichroism. *The Journal of Chemical Physics*, 153(5):054707, 2020.
- [49] Alexander Kastner, Greta Koumarianou, Pavle Glodic, Peter C Samartzis, Nicolas Ladda, Simon T Ranecky, Tom Ring, Sudheendran Vasudevan, Constantin Witte, Hendrike Braun, et al. High-resolution resonance-enhanced multiphoton photoelectron circular dichroism. *Physical Chemistry Chemical Physics*, 22(14):7404–7411, 2020.
- [50] Brooks H Pate, Justin L Neill, and Matt T Muckle. Molecular rotational resonance spectroscopy-chiral analysis without chromatography. *Mass Spectrometry*, 2021.
- [51] Justin L Neill, Alexander V Mikhonin, Ted Chen, Reilly E Sonstrom, and Brooks H Pate. Rapid quantification of isomeric and dehalogenated impurities in pharmaceutical raw materials using mrr spectroscopy. *Journal of Pharmaceutical and Biomedical Analysis*, 189:113474, 2020.
- [52] Leo A Joyce, Danielle M Schultz, Edward C Sherer, Justin L Neill, Reilly E Sonstrom, and Brooks H Pate. Direct regioisomer analysis of crude reaction mixtures via molecular rotational resonance (mrr) spectroscopy. *Chemical science*, 11(24):6332–6338, 2020.

- [53] Brooks H Pate, Luca Evangelisti, Walther Caminati, Yunjie Xu, Javix Thomas, David Patterson, Cristobal Perez, and Melanie Schnell. Quantitative chiral analysis by molecular rotational spectroscopy. In *Chiral Analysis*, pages 679–729. Elsevier, 2018.
- [54] Sérgio R Domingos, Cristóbal Pérez, Mark D Marshall, Helen O Leung, and Melanie Schnell. Assessing the performance of rotational spectroscopy in chiral analysis. *Chemical science*, 11(40):10863–10870, 2020.
- [55] Sérgio R Domingos, Cristóbal Pérez, Nora M Kreienborg, Christian Merten, and Melanie Schnell. Dynamic chiral self-recognition in aromatic dimers of styrene oxide revealed by rotational spectroscopy. *Communications Chemistry*, 4(1):1–11, 2021.
- [56] Fan Xie, Sethupathy Mahendiran, Nathan A Seifert, and Yunjie Xu. Modifying conformational distribution of chiral tetrahydro-2-furoic acid through its interaction with water: a rotational spectroscopic and theoretical investigation. *Physical Chemistry Chemical Physics*, 23(6):3820–3825, 2021.
- [57] Fan Xie, Nathan A Seifert, Arsh S Hazrah, Wolfgang Jäger, and Yunjie Xu. Conformational landscape, chirality recognition and chiral analyses: Rotational spectroscopy of tetrahydro-2-furoic acid propylene oxide conformers. *ChemPhysChem*, 22(5):455–460, 2021.
- [58] Joshua E Isert, Frank E Marshall, William C Bailey, and Garry S Grubbs. Dipole forbidden, nuclear electric quadrupole allowed transitions and chirality: The broadband microwave spectrum and structure of 2-bromo-1, 1, 1, 2-tetrafluoroethane. *Journal of Molecular Structure*, 1216:128277, 2020.
- [59] W Leo Meerts and Michael Schmitt. Application of genetic algorithms in automated assignments of high-resolution spectra. *International Reviews in Physical Chemistry*, 25(3):353–406, 2006.
- [60] Lia Yeh, Lincoln Satterthwaite, and David Patterson. Automated, context-free assignment of asymmetric rotor microwave spectra. *The Journal of chemical physics*, 150(20):204122, 2019.
- [61] P Brandon Carroll, Kin Long Kelvin Lee, and Michael C McCarthy. A high speed fitting program for rotational spectroscopy. *Journal of Molecular Spectroscopy*, 379:111467, 2021.
- [62] Michael McCarthy and Kin Long Kelvin Lee. Molecule identification with rotational spectroscopy and probabilistic deep learning. *The Journal of Physical Chemistry A*, 124(15):3002–3017, 2020.

## BIBLIOGRAPHY

---

- [63] V Alvin Shubert, David Schmitz, Chris Medcraft, Anna Krin, David Patterson, John M Doyle, and Melanie Schnell. Rotational spectroscopy and three-wave mixing of 4-carvomenthenol: A technical guide to measuring chirality in the microwave regime. *The Journal of chemical physics*, 142(21):214201, 2015.
- [64] V Alvin Shubert, David Schmitz, and Melanie Schnell. Enantiomer-sensitive spectroscopy and mixture analysis of chiral molecules containing two stereogenic centers—microwave three-wave mixing of menthone. *Journal of Molecular Spectroscopy*, 300:31–36, 2014.
- [65] Lincoln Satterthwaite, Cristóbal Pérez, Amanda L Steber, Dylan Finestone, Robert L Broadrup, and David Patterson. Enantiomeric analysis of chiral isotopomers via microwave three-wave mixing. *The Journal of Physical Chemistry A*, 123(14):3194–3198, 2019.
- [66] Francis J Lovas, David F Plusquellic, Brooks H Pate, Justin L Neill, Matthew T Muckle, and Anthony J Remijan. Microwave spectrum of 1, 2-propanediol. *Journal of Molecular Spectroscopy*, 257(1):82–93, 2009.
- [67] Zachary G Brill, Matthew L Condakes, Chi P Ting, and Thomas J Maimone. Navigating the chiral pool in the total synthesis of complex terpene natural products. *Chemical reviews*, 117(18):11753–11795, 2017.
- [68] Alexandra E Gollhofer, Antonio J Tenorio, Nina O Dimauro, Nicolas R Mairata, F Omar Holguin, and William Maio. Using (+)-carvone to access novel derivatives of (+)-ent-cannabidiol: The first asymmetric syntheses of (+)-ent-cbdp and (+)-ent-cbdv. *Tetrahedron Letters*, 67:152891, 2021.
- [69] Carter N Stout and Hans Renata. Reinvigorating the chiral pool: chemoenzymatic approaches to complex peptides and terpenoids. *Accounts of chemical research*, 54(5):1143–1156, 2021.
- [70] Qi Liu, Xinyue Xie, Mancheng Tang, Wentao Tao, Ting Shi, Yuanzhen Zhang, Tingting Huang, Yilei Zhao, Zixin Deng, and Shuangjun Lin. One-pot asymmetric synthesis of an aminodiol intermediate of florfenicol using engineered transketolase and transaminase. *ACS Catalysis*, 11:7477–7488, 2021.
- [71] Zai-Bao Sun, Zhi-Jun Zhang, Fu-Long Li, Yao Nie, Hui-Lei Yu, and Jian-He Xu. One pot asymmetric synthesis of (r)-phenylglycinol from racemic styrene oxide via cascade biocatalysis. *ChemCatChem*, 11(16):3802–3807, 2019.
- [72] EM Neeman, J-R Avilés-Moreno, and TR Huet. The quasi-unchanged gas-phase molecular structures of the atmospheric aerosol precursor  $\beta$ -pinene and its oxidation product nopinone. *Physical Chemistry Chemical Physics*, 19(21):13819–13827, 2017.

## BIBLIOGRAPHY

---

- [73] Anthony J Remijan, A Markwick-Kemper, et al. Splatalogue: Database for astronomical spectroscopy. In *American Astronomical Society Meeting Abstracts*, volume 211, pages 132–11, 2007.
- [74] Christian P Endres, Stephan Schlemmer, Peter Schilke, Jürgen Stutzki, and Holger SP Müller. The cologne database for molecular spectroscopy, cdms, in the virtual atomic and molecular data centre, vamdc. *Journal of Molecular Spectroscopy*, 327:95–104, 2016.
- [75] Marie-Aline Martin-Drumel, Michael C McCarthy, David Patterson, Brett A McGuire, and Kyle N Crabtree. Automated microwave double resonance spectroscopy: A tool to identify and characterize chemical compounds. *The Journal of chemical physics*, 144(12):124202, 2016.
- [76] Alexandra N Pilidi, Irini K Gavra, and Athanassios A Tsekouras. Spontaneous polarization of cryo-deposited films for five normal saturated monohydroxy alcohols,  $C_nH_{2n+1}OH$ ,  $n=1-5$ . *The Journal of Physical Chemistry B*, 123(40):8505–8511, 2019.
- [77] Toshiki Sugimoto and Yoshiyasu Matsumoto. Orientational ordering in heteroepitaxial water ice on metal surfaces. *Physical Chemistry Chemical Physics*, 22(29):16453–16466, 2020.
- [78] SM Jackson and Robert W Whitworth. Evidence for ferroelectric ordering of ice  $ih$ . *The Journal of chemical physics*, 103(17):7647–7648, 1995.
- [79] Hanfu Wang, Richard C Bell, Martin J Iedema, Athanassios A Tsekouras, and James P Cowin. Sticky ice grains aid planet formation: Unusual properties of cryogenic water ice. *The Astrophysical Journal*, 620(2):1027, 2005.
- [80] Yuan Liu and Lars Ojamae. Raman and ir spectra of ice  $ih$  and ice  $xi$  with an assessment of dft methods. *The Journal of Physical Chemistry B*, 120(42):11043–11051, 2016.
- [81] P Parkkinen, S Riikonen, and L Halonen. Ice  $xi$ : not that ferroelectric. *The Journal of Physical Chemistry C*, 118(45):26264–26275, 2014.
- [82] Xingcai Su, L Lianos, Y Ron Shen, and Gabor A Somorjai. Surface-induced ferroelectric ice on  $pt(111)$ . *Physical review letters*, 80(7):1533, 1998.
- [83] D Field, O Plekan, A Cassidy, R Balog, NC Jones, and J Dunger. Spontaneous electric fields in solid films: spontelectrics. *International Reviews in Physical Chemistry*, 32(3):345–392, 2013.
- [84] Richard Balog, P Cicman, NC Jones, and D Field. Spontaneous dipole alignment in films of  $n_2o$ . *Physical review letters*, 102(7):073003, 2009.

- [85] Karin M Rabe, Matthew Dawber, Céline Lichtensteiger, Charles H Ahn, and Jean-Marc Triscone. Modern physics of ferroelectrics: Essential background. In *Physics of Ferroelectrics*, pages 1–30. Springer, 2007.
- [86] Andrew Cassidy, Oksana Plekan, Richard Balog, Jack Dunger, David Field, and Nykola C Jones. Electric field structures in thin films: Formation and properties. *The Journal of Physical Chemistry A*, 118(33):6615–6621, 2014.
- [87] Maksymilian Roman, Aimee Dunn, Skandar Taj, Zibo Goabaone Keolopile, Alexander Rosu-Finsen, Maciej Gutowski, Martin RS McCoustra, Andrew M Cassidy, and David Field. Assigning a structural motif using spontaneous molecular dipole orientation in thin films. *Physical Chemistry Chemical Physics*, 20(46):29038–29044, 2018.
- [88] A Drobyshev, A Aldiyarov, D Sokolov, and A Shinbayeva. Refractive indices and density of cryovacuum-deposited thin films of methane in the vicinity of the  $\alpha$ - $\beta$ -transition temperature. *Low Temperature Physics*, 43(6):724–727, 2017.
- [89] Clara Stoeffler, Benoît Darquié, Alexander Shelkovnikov, Christophe Daussy, Anne Amy-Klein, Christian Chardonnet, Laure Guy, Jeanne Crassous, Thérèse R Huet, Pascale Soulard, et al. High resolution spectroscopy of methyltrioxorhenium: towards the observation of parity violation in chiral molecules. *Physical Chemistry Chemical Physics*, 13(3):854–863, 2011.
- [90] Chien-Shiung Wu, Ernest Ambler, Raymond W Hayward, Dale D Hoppes, and Ralph Percy Hudson. Experimental test of parity conservation in beta decay. *Physical Review*, 105(4):1413, 1957.
- [91] NH Edwards, SJ Phipp, PEG Baird, and S Nakayama. Precise measurement of parity nonconserving optical rotation in atomic thallium. *Physical Review Letters*, 74(14):2654, 1995.
- [92] DM Meekhof, PA Vetter, PK Majumder, SK Lamoreaux, and EN Fortson. Optical-rotation technique used for a high-precision measurement of parity nonconservation in atomic lead. *Physical Review A*, 52(3):1895, 1995.
- [93] MJD Macpherson, KP Zetie, RB Warrington, DN Stacey, and JP Hoare. Precise measurement of parity nonconserving optical rotation at 876 nm in atomic bismuth. *Physical Review Letters*, 67(20):2784, 1991.
- [94] Konstantin Tsigutkin, D Dounas-Frazer, A Family, Jason E Stalnaker, Valeriy V Yashchuk, and D Budker. Observation of a large atomic parity violation effect in ytterbium. *Physical review letters*, 103(7):071601, 2009.
- [95] Sosale Chandrasekhar. Molecular homochirality and the parity-violating energy difference. a critique with new proposals. *Chirality*, 20(2):84–95, 2008.

## BIBLIOGRAPHY

---

- [96] Cheryl D Stevenson and John P Davis. Magnetars and magnetic separation of chiral radicals in interstellar space: Homochirality. *The Journal of Physical Chemistry A*, 123(44):9587–9593, 2019.
- [97] William A Bonner. Parity violation and the evolution of biomolecular homochirality. *Chirality*, 12(3):114–126, 2000.
- [98] Masato Senami and Tomoki Shimizu. Electron chirality in amino acid molecules. *Physics Letters A*, 384(32):126796, 2020.
- [99] Jon K Laerdahl and Peter Schwerdtfeger. Fully relativistic ab initio calculations of the energies of chiral molecules including parity-violating weak interactions. *Physical Review A*, 60(6):4439, 1999.
- [100] Peter Schwerdtfeger, Johannes Gierlich, and Tobias Bollwein. Large parity-violation effects in heavy-metal-containing chiral compounds. *Angewandte Chemie International Edition*, 42(11):1293–1296, 2003.
- [101] Benoît Darquié, Nidal Saleh, Sean K Tokunaga, Monika Srebro-Hooper, Aurora Ponzi, Jochen Autschbach, Piero Decleva, Gustavo Adolfo Garcia, Jeanne Crassous, and Laurent Nahon. Valence-shell photoelectron circular dichroism of ruthenium (iii)-tris-(acetylacetonato) gas-phase enantiomers. *Physical Chemistry Chemical Physics*, 2021.
- [102] VS Letokhov. On difference of energy levels of left and right molecules due to weak interactions. *Physics Letters A*, 53(4):275–276, 1975.
- [103] Benoît Darquié, Clara Stoeffler, Alexander Shelkovnikov, Christophe Daussy, Anne Amy-Klein, Christian Chardonnet, Samia Zrig, Laure Guy, Jeanne Crassous, Pascale Soulard, et al. Progress toward the first observation of parity violation in chiral molecules by high-resolution laser spectroscopy. *Chirality*, 22(10):870–884, 2010.
- [104] Martin Quack, Jürgen Stohner, and Martin Willeke. High-resolution spectroscopic studies and theory of parity violation in chiral molecules. *Annu. Rev. Phys. Chem.*, 59:741–769, 2008.
- [105] John W Blanchard, Jonathan P King, Tobias F Sjolander, Mikhail G Kozlov, and Dmitry Budker. Molecular parity nonconservation in nuclear spin couplings. *Physical Review Research*, 2(2):023258, 2020.
- [106] James Eills, John W Blanchard, Lykourgos Bougas, Mikhail G Kozlov, Alexander Pines, and Dmitry Budker. Measuring molecular parity nonconservation using nuclear-magnetic-resonance spectroscopy. *Physical Review A*, 96(4):042119, 2017.

## BIBLIOGRAPHY

---

- [107] Bruno Chanteau, Bérengère Argence, Olivier Lopez, Wei Zhang, Daniele Nicolodi, Michel Abgrall, F Auguste, PLT Sow, Sinda Mejri, SK Tokunaga, et al. Mid-ir frequency control using an optical frequency comb and a remote near-infrared frequency reference. In *International Quantum Electronics Conference*, page ID\_P\_6. Optica Publishing Group, 2013.
- [108] Sean K Tokunaga, Clara Stoeffler, Frédéric Auguste, Alexander Shelkovnikov, Christophe Daussy, Anne Amy-Klein, Christian Chardonnet, and Benoît Darquié. Probing weak force-induced parity violation by high-resolution mid-infrared molecular spectroscopy. *Molecular Physics*, 111(14-15):2363–2373, 2013.
- [109] Peter Schwerdtfeger, Andreas Kühn, Radovan Bast, Jon K Laerdahl, Francesco Faglioni, and Paolo Lazzeretti. The vibrational spectrum of camphor from ab initio and density functional theory and parity violation in the c–c\*–co bending mode. *Chemical Physics Letters*, 383(5-6):496–501, 2004.
- [110] Anne Cournol, Mathieu Manceau, M Pierens, Louis Lecordier, DBA Tran, Rosa Santagata, B Argence, A Goncharov, Olivier Lopez, Michel Abgrall, et al. A new experiment to test parity symmetry in cold chiral molecules using vibrational spectroscopy. *Quantum Electronics*, 49(3):288, 2019.
- [111] Ennio Arimondo, P Glorieux, and T Oka. Observation of inverted infrared lamb dips in separated optical isomers. *Optics Communications*, 23(3):369–372, 1977.
- [112] M Ziskind, C Daussy, T Marrel, and Ch Chardonnet. Improved sensitivity in the search for a parity-violating energy difference in the vibrational spectrum of the enantiomers of chfclbr. *The European Physical Journal D-Atomic, Molecular, Optical and Plasma Physics*, 20(2):219–225, 2002.
- [113] AS Lahamer, SM Mahurin, RN Compton, D House, JK Laerdahl, M Lein, and P Schwerdtfeger. Search for a parity-violating energy difference between enantiomers of a chiral iron complex. *Physical Review Letters*, 85(21):4470, 2000.
- [114] Elijah G Schnitzler, Brandi LM Zenchyzen, and Wolfgang Jäger. High-resolution fourier-transform microwave spectroscopy of methyl-and dimethylnaphthalenes. *The Astrophysical Journal*, 805(2):141, 2015.
- [115] Jessica P Porterfield, Lincoln Satterthwaite, Sandra Eibenberger, David Patterson, and Michael C McCarthy. High sensitivity microwave spectroscopy in a cryogenic buffer gas cell. *Review of Scientific Instruments*, 90(5):053104, 2019.
- [116] GK White. The thermal and electrical conductivity of copper at low temperatures. *Australian Journal of Physics*, 6(4):397–404, 1953.



## BIBLIOGRAPHY

---

- [117] TJ Balle and WH Flygare. Fabry–perot cavity pulsed fourier transform microwave spectrometer with a pulsed nozzle particle source. *Review of Scientific Instruments*, 52(1):33–45, 1981.
- [118] Sebastien Bize, Yvan Sortais, Cipriana Mandache, André Clairon, and Christophe Salomon. Cavity frequency pulling in cold atom fountains. *IEEE Transactions on Instrumentation and Measurement*, 50(2):503–506, 2001.
- [119] Jacques Viennet, Claude Audoin, and Michel Desaintfusicien. Cavity pulling in passive frequency standards. *IEEE Transactions on Instrumentation and Measurement*, 21(3):204–209, 1972.
- [120] Aldo Godone, Salvatore Micalizio, Filippo Levi, and Claudio Calosso. Microwave cavities for vapor cell frequency standards. *Review of Scientific Instruments*, 82(7):074703, 2011.
- [121] David Patterson and John M Doyle. Sensitive chiral analysis via microwave three-wave mixing. *Physical Review Letters*, 111(2):023008, 2013.
- [122] Richard Balog, P Cicman, NC Jones, and D Field. Spontaneous dipole alignment in films of n 2 o. *Physical Review Letters*, 102(7):073003, 2009.
- [123] Oksana Plekan, Andrew Cassidy, Richard Balog, Nykola C Jones, and David Field. A new form of spontaneously polarized material. *Physical Chemistry Chemical Physics*, 13(47):21035–21044, 2011.
- [124] Oksana Plekan, Alexander Rosu-Finsen, Andrew M Cassidy, Jérôme Lasne, Martin RS McCoustra, and David Field. A review of recent progress in understanding the spontelectric state of matter. *The European Physical Journal D*, 71(6):1–8, 2017.
- [125] Colin M Western. Pgopher: A program for simulating rotational, vibrational and electronic spectra. *Journal of Quantitative Spectroscopy and Radiative Transfer*, 186:221–242, 2017.
- [126] ZD Reed, DA Long, Helene Fleurbaey, and JT Hodges. Si-traceable molecular transition frequency measurements at the 10- 12 relative uncertainty level. *Optica*, 7(9):1209–1220, 2020.
- [127] David Patterson and John M Doyle. Bright, guided molecular beam with hydrodynamic enhancement. *The Journal of Chemical Physics*, 126(15):154307, 2007.
- [128] Nicholas R Hutzler, Hsin-I Lu, and John M Doyle. The buffer gas beam: An intense, cold, and slow source for atoms and molecules. *Chemical Reviews*, 112(9):4803–4827, 2012.

## BIBLIOGRAPHY

---

- [129] David Patterson, Julia Rasmussen, and John M Doyle. Intense atomic and molecular beams via neon buffer-gas cooling. *New Journal of Physics*, 11(5):055018, 2009.
- [130] Di Xiao, David M Lancaster, Cameron H Allen, Mckenzie J Taylor, Thomas A Lancaster, Gage Shaw, Nicholas R Hutzler, and Jonathan D Weinstein. Shaped nozzles for cryogenic buffer-gas beam sources. *Physical Review A*, 99(1):013603, 2019.
- [131] Melanie Schnell and Jochen Küpper. Tailored molecular samples for precision spectroscopy experiments. *Faraday discussions*, 150:33–49, 2011.
- [132] Marit R Fiechter, Pi AB Haase, Nidal Saleh, Pascale Soulard, Benoît Tremblay, Remco WA Havenith, Rob GE Timmermans, Peter Schwerdtfeger, Jeanne Crasous, Benoît Darquié, et al. Toward detection of the molecular parity violation in chiral ru (acac) 3 and os (acac) 3. *The Journal of Physical Chemistry Letters*, 13(42):10011–10017, 2022.
- [133] Michael Thomas, Irene Suarez-Martinez, Li-Juan Yu, Amir Karton, Graham S Chandler, Marc Robinson, Isabelle Cherchneff, Dahbia Talbi, and Dino Spagnoli. Atomistic simulations of the aggregation of small aromatic molecules in homogenous and heterogenous mixtures. *Physical Chemistry Chemical Physics*, 22(37):21005–21014, 2020.
- [134] Mariyam Fatima, Amanda L Steber, Anja Poblitzki, Cristóbal Pérez, Sabrina Zinn, and Melanie Schnell. Rotational signatures of dispersive stacking in the formation of aromatic dimers. *Angewandte Chemie*, 131(10):3140–3145, 2019.
- [135] Hilda Sandstrom and Martin Rahm. The beginning of hcn polymerization: Iminoacetonitrile formation and its implications in astrochemical environments. *ACS Earth and Space Chemistry*, 5(8):2152–2159, 2021.
- [136] Luyao Zou, Brian M Hays, and Susanna L Widicus Weaver. Weakly bound clusters in astrochemistry? millimeter and submillimeter spectroscopy of trans-ho3 and comparison to astronomical observations. *The Journal of Physical Chemistry A*, 120(5):657–667, 2016.
- [137] Tamar Stein and Jeeno Jose. Molecular formation upon ionization of van der waals clusters and implication to astrochemistry. *Israel Journal of Chemistry*, 60(8-9):842–849, 2020.
- [138] LH Coudert, FJ Lovas, RD Suenram, and JT Hougen. New measurements of microwave transitions in the water dimer. *The Journal of chemical physics*, 87(11):6290–6299, 1987.

- [139] AC Legon, DJ Millen, and PJ Mjoberg. The hydrogen cyanide dimer: identification and structure from microwave spectroscopy. *Chemical Physics Letters*, 47(3):589–591, 1977.
- [140] Elias M Neeman, Juan Ramón Avilés Moreno, and Thérèse R Huet. Gas-phase hydration of nopinone: the interplay between theoretical methods and experiments unveils the conformational landscape. *Physical Chemistry Chemical Physics*, 23(33):18137–18144, 2021.
- [141] Thomas R Dyke, Brian J Howard, and William Klemperer. Radiofrequency and microwave spectrum of the hydrogen fluoride dimer; a nonrigid molecule. *The Journal of Chemical Physics*, 56(5):2442–2454, 1972.
- [142] Cristóbal Pérez, Daniel P Zaleski, Nathan A Seifert, Berhane Temelso, George C Shields, Zbigniew Kisiel, and Brooks H Pate. Hydrogen bond cooperativity and the three-dimensional structures of water nonamers and decamers. *Angewandte Chemie*, 126(52):14596–14600, 2014.
- [143] Jérémy Bourgalais, Vivien Roussel, Michael Capron, Abdessamad Benidar, AW Jasper, SJ Klippenstein, Ludovic Biennier, and Sébastien D Le Picard. Low temperature kinetics of the first steps of water cluster formation. *Physical review letters*, 116(11):113401, 2016.
- [144] Divita Gupta, Sidaty Cheikh Sid Ely, Ilsa R Cooke, Théo Guillaume, Omar Abdelkader Khedaoui, Thomas S Hearne, Brian M Hays, and Ian R Sims. Low temperature kinetics of the reaction between methanol and the cn radical. *The Journal of Physical Chemistry A*, 123(46):9995–10003, 2019.
- [145] James M Oldham, Chamara Abeysekera, Baptiste Joalland, Lindsay N Zack, Kirill Prozument, Ian R Sims, G Barratt Park, Robert W Field, and Arthur G Suits. A chirped-pulse fourier-transform microwave/pulsed uniform flow spectrometer. i. the low-temperature flow system. *The Journal of chemical physics*, 141(15):154202, 2014.
- [146] Ian WM Smith. Reactions at very low temperatures: gas kinetics at a new frontier. *Angewandte Chemie International Edition*, 45(18):2842–2861, 2006.
- [147] Garrett K Drayna, Christian Hallas, Kenneth Wang, Sergio R Domingos, Sandra Eibenberger, John M Doyle, and David Patterson. Direct time-domain observation of conformational relaxation in gas-phase cold collisions. *Angewandte Chemie*, 128(16):5041–5045, 2016.
- [148] Ramesh K Kakar and C Richard Quade. Microwave rotational spectrum and internal rotation in gauche ethyl alcohol. *The Journal of Chemical Physics*, 72(8):4300–4307, 1980.

## BIBLIOGRAPHY

---

- [149] Ian A Finneran, P Brandon Carroll, Griffin J Mead, and Geoffrey A Blake. Hydrogen bond competition in the ethanol–methanol dimer. *Physical Chemistry Chemical Physics*, 18(32):22565–22572, 2016.
- [150] Ian A Finneran, P Brandon Carroll, Marco A Allodi, and Geoffrey A Blake. Hydrogen bonding in the ethanol–water dimer. *Physical Chemistry Chemical Physics*, 17(37):24210–24214, 2015.
- [151] RM Lees, FJ Lovas, WH Kirchhoff, and DRs Johnson. Microwave spectra of molecules of astrophysical interest: Iii. methanol. *Journal of Physical and Chemical Reference Data*, 2(2):205–214, 1973.
- [152] Garrett Korda Drayna. *Novel Applications of Buffer-gas Cooling to Cold Atoms, Diatomic Molecules, and Large Molecules*. PhD thesis, Harvard University, 2016.
- [153] Kevin M Hickson, Somnath Bhowmick, Yury V Suleimanov, João Brandão, and Daniela V Coelho. Experimental and theoretical studies of the gas-phase reactions of o (1 d) with h 2 o and d 2 o at low temperature. *Physical Chemistry Chemical Physics*, 23(45):25797–25806, 2021.
- [154] Kevin M Hickson and Jean-Christophe Loison. Kinetic study of the gas-phase o (1d)+ ch3oh and o (1d)+ ch3cn reactions: Low-temperature rate constants and atomic hydrogen product yields. *The Journal of Physical Chemistry A*, 2022.
- [155] Ilsa R Cooke and Ian R Sims. Experimental studies of gas-phase reactivity in relation to complex organic molecules in star-forming regions. *ACS Earth and Space Chemistry*, 3(7):1109–1134, 2019.
- [156] Robin J Shannon, Mark A Blitz, Andrew Goddard, and Dwayne E Heard. Accelerated chemistry in the reaction between the hydroxyl radical and methanol at interstellar temperatures facilitated by tunnelling. *Nature chemistry*, 5(9):745–749, 2013.
- [157] Meryem Tizniti, Sébastien D Le Picard, François Lique, Coralie Berteloite, André Canosa, Millard H Alexander, and Ian R Sims. The rate of the f+ h2 reaction at very low temperatures. *Nature chemistry*, 6(2):141–145, 2014.
- [158] Kevin M Hickson, Jean-Christophe Loison, Dianailys Nuñez-Reyes, and Raphaël Méreau. Quantum tunneling enhancement of the c+ h2o and c+ d2o reactions at low temperature. *The journal of physical chemistry letters*, 7(18):3641–3646, 2016.
- [159] April M Cooper and Johannes Kastner. Low-temperature kinetic isotope effects in ch3oh+ h→ ch2oh+ h2 shed light on the deuteration of methanol in space. *The Journal of Physical Chemistry A*, 123(42):9061–9068, 2019.

## BIBLIOGRAPHY

---

- [160] Boris Nizamov and Stephen R Leone. Rate coefficients and kinetic isotope effect for the c2h reactions with nh3 and nd3 in the 104- 294 k temperature range. *The Journal of Physical Chemistry A*, 108(17):3766–3771, 2004.
- [161] Michele Ceriotti, Wei Fang, Peter G Kusalik, Ross H McKenzie, Angelos Michaelides, Miguel A Morales, and Thomas E Markland. Nuclear quantum effects in water and aqueous systems: Experiment, theory, and current challenges. *Chemical reviews*, 116(13):7529–7550, 2016.
- [162] Emilio Méndez and Daniel Laria. Nuclear quantum effects on the hydrogen bond donor–acceptor exchange in water–water and water–methanol dimers. *The Journal of Chemical Physics*, 153(5):054302, 2020.
- [163] Eleftherios Lambros and Francesco Paesani. How good are polarizable and flexible models for water: Insights from a many-body perspective. *The Journal of Chemical Physics*, 153(6):060901, 2020.
- [164] Xin Xu and William A Goddard. Bonding properties of the water dimer: A comparative study of density functional theories. *The Journal of Physical Chemistry A*, 108(12):2305–2313, 2004.
- [165] Huafeng Xu, Harry A Stern, and BJ Berne. Can water polarizability be ignored in hydrogen bond kinetics? *The Journal of Physical Chemistry B*, 106(8):2054–2060, 2002.
- [166] Joel D Mallory and Vladimir A Mandelshtam. Diffusion monte carlo studies of mb-pol (h2o) 2- 6 and (d2o) 2- 6 clusters: Structures and binding energies. *The Journal of Chemical Physics*, 145(6):064308, 2016.
- [167] X Huang, Bastiaan J Braams, Joel M Bowman, Ross EA Kelly, Jonathan Tennyson, Gerrit C Groenenboom, and Ad van der Avoird. New ab initio potential energy surface and the vibration-rotation-tunneling levels of (h 2 o) 2 and (d 2 o) 2. *The Journal of chemical physics*, 128(3):034312, 2008.
- [168] Kevin P Bishop and Pierre-Nicholas Roy. Quantum mechanical free energy profiles with post-quantization restraints: Binding free energy of the water dimer over a broad range of temperatures. *The Journal of Chemical Physics*, 148(10):102303, 2018.
- [169] Victor GM Lee and Anne B McCoy. An efficient approach for studies of water clusters using diffusion monte carlo. *The Journal of Physical Chemistry A*, 123(37):8063–8070, 2019.
- [170] Manas Ranjan Dash and B Rajakumar. Abstraction and addition kinetics of c 2 h radicals with ch 4, c 2 h 6, c 3 h 8, c 2 h 4, and c 3 h 6: Cvt/sct/ispe and hybrid meta-dft methods. *Physical Chemistry Chemical Physics*, 17(5):3142–3156, 2015.

## BIBLIOGRAPHY

---

- [171] Brian J Opansky and Stephen R Leone. Low-temperature rate coefficients of c2h with ch4 and cd4 from 154 to 359 k. *The Journal of Physical Chemistry*, 100(12):4888–4892, 1996.
- [172] Frank N Keutsch and Richard J Saykally. Water clusters: Untangling the mysteries of the liquid, one molecule at a time. *Proceedings of the National Academy of Sciences*, 98(19):10533–10540, 2001.
- [173] Gerald T Fraser, Francis J Lovas, RD Suenram, EN Karyakin, A Grushow, WA Burns, and KR Leopold. Microwave and submillimeter-wave spectra of the mixed deuterated–protonated water-dimer isotopomers. *Journal of molecular spectroscopy*, 181(2):229–245, 1997.
- [174] G Barratt Park and Robert W Field. Perspective: The first ten years of broadband chirped pulse fourier transform microwave spectroscopy. *The Journal of chemical physics*, 144(20):200901, 2016.
- [175] Cristóbal Pérez, Daniel P Zaleski, Nathan A Seifert, Berhane Temelso, George C Shields, Zbigniew Kisiel, and Brooks H Pate. Hydrogen bond cooperativity and the three-dimensional structures of water nonamers and decamers. *Angewandte Chemie*, 126(52):14596–14600, 2014.
- [176] Marcos Juanes, Rizalina T Saragi, Walther Caminati, and Alberto Lesarri. The hydrogen bond and beyond: Perspectives for rotational investigations of non-covalent interactions. *Chemistry—A European Journal*, 25(49):11402–11411, 2019.
- [177] Cristóbal Pérez, Matt T Muckle, Daniel P Zaleski, Nathan A Seifert, Berhane Temelso, George C Shields, Zbigniew Kisiel, and Brooks H Pate. Structures of cage, prism, and book isomers of water hexamer from broadband rotational spectroscopy. *Science*, 336(6083):897–901, 2012.
- [178] Anna Gutberlet, Gerhard Schwaab, and Martina Havenith. High-resolution ir spectroscopy of dimers of hdo with h2o in helium nanodroplets. *The Journal of Physical Chemistry A*, 115(23):6297–6305, 2011.
- [179] Kirill Kuyanov-Prozument, Myong Yong Choi, and Andrey F Vilesov. Spectrum and infrared intensities of oh-stretching bands of water dimers. *The Journal of chemical physics*, 132(1):014304, 2010.
- [180] Jeremy O Richardson, Stuart C Althorpe, and David J Wales. Instanton calculations of tunneling splittings for water dimer and trimer. *The Journal of chemical physics*, 135(12):124109, 2011.
- [181] Ryan J DiRisio, Jacob M Finney, and Anne B McCoy. Diffusion monte carlo approaches for studying nuclear quantum effects in fluxional molecules. *Wiley Interdisciplinary Reviews: Computational Molecular Science*, page e1615, 2022.

## BIBLIOGRAPHY

---

- [182] Apurba Nandi, Chen Qu, Paul L Houston, Riccardo Conte, Qi Yu, and Joel M Bowman. A ccSD (t)-based 4-body potential for water. *The Journal of Physical Chemistry Letters*, 12(42):10318–10324, 2021.
- [183] Jeremy O Richardson. Perspective: Ring-polymer instanton theory. *The Journal of chemical physics*, 148(20):200901, 2018.
- [184] Pablo E Videla, Peter J Rossky, and D Laria. Nuclear quantum effects on the structure and the dynamics of [h<sub>2</sub>O]<sub>8</sub> at low temperatures. *The Journal of Chemical Physics*, 139(17):174315, 2013.
- [185] Lincoln Satterthwaite, Greta Koumarianou, Brandon P Carroll, RJ Sedlik, Michael C. McCarthy, and David Patterson. Conformer-selected dimer formation. *X, X(X):X*, 2022.
- [186] Greta Koumarianou, Irene Wang, Lincoln Satterthwaite, and David Patterson. Assignment-free chirality detection in unknown samples via microwave three-wave mixing. *Communications Chemistry*, 5(1):1–7, 2022.
- [187] Lu Gem Gao, Donald G Fleming, Donald G Truhlar, and Xuefei Xu. Large anharmonic effects on tunneling and kinetics: Reaction of propane with muonium. *The Journal of Physical Chemistry Letters*, 12(17):4154–4159, 2021.
- [188] T Kumagai, M Kaizu, S Hattta, H Okuyama, T Aruga, I Hamada, and Y Morikawa. Direct observation of hydrogen-bond exchange within a single water dimer. *Physical review letters*, 100(16):166101, 2008.
- [189] Anthony J Remijan, A Markwick-Kemper, et al. Splatalogue: database for astronomical spectroscopy. In *American Astronomical Society Meeting Abstracts*, volume 211, pages 132–11, 2007.
- [190] Zheng Su, Nicole Borho, and Yunjie Xu. Chiral self-recognition: Direct spectroscopic detection of the homochiral and heterochiral dimers of propylene oxide in the gas phase. *Journal of the American Chemical Society*, 128(51):17126–17131, 2006.
- [191] Anne Zehnacker and Martin A Suhm. Chirality recognition between neutral molecules in the gas phase. *Angewandte Chemie International Edition*, 47(37):6970–6992, 2008.
- [192] Nicole Borho and Martin A Suhm. Glycidol dimer: anatomy of a molecular handshake. *Physical Chemistry Chemical Physics*, 4(12):2721–2732, 2002.
- [193] Alberto Macario, Susana Blanco, Javix Thomas, Yunjie Xu, and Juan Carlos López. Competition between intra-and intermolecular hydrogen bonding: o-anisic acid formic acid heterodimer. *Chemistry—A European Journal*, 25(53):12325–12331, 2019.

## BIBLIOGRAPHY

---

- [194] Marcelino Agúndez, Carlos Cabezas, Belén Tercero, Nuria Marcelino, JD Gallego, P de Vicente, and José Cernicharo. Discovery of the propargyl radical (ch<sub>2</sub>cch) in tmc-1: One of the most abundant radicals ever found and a key species for cyclization to benzene in cold dark clouds. *Astronomy & Astrophysics*, 647:L10, 2021.
- [195] Andrew M Burkhardt, Ryan A Loomis, Christopher N Shingledecker, Kin Long Kelvin Lee, Anthony J Remijan, Michael C McCarthy, and Brett A McGuire. Ubiquitous aromatic carbon chemistry at the earliest stages of star formation. *Nature Astronomy*, 5(2):181–187, 2021.
- [196] Sommer L Johansen, Marie-Aline Martin-Drumel, and Kyle N Crabtree. Rotational spectrum of the  $\beta$ -cyanovinyl radical: a possible astrophysical n-heterocycle precursor. *The Journal of Physical Chemistry A*, 123(24):5171–5177, 2019.
- [197] Chamara Abeysekera, AO Hernandez-Castillo, John F Stanton, and Timothy S Zwier. Broadband microwave spectroscopy of 2-furanyloxy radical: primary pyrolysis product of the second-generation biofuel 2-methoxyfuran. *The Journal of Physical Chemistry A*, 122(34):6879–6885, 2018.
- [198] Alicia O Hernandez-Castillo, Chamara Abeysekera, John F Stanton, and Timothy S Zwier. Structural characterization of phenoxy radical with mass-correlated broadband microwave spectroscopy. *The Journal of Physical Chemistry Letters*, 10(11):2919–2923, 2019.
- [199] Michael C McCarthy, Kin Long Kelvin Lee, P Brandon Carroll, Jessica P Porterfield, P Bryan Changala, James H Thorpe, and John F Stanton. Exhaustive product analysis of three benzene discharges by microwave spectroscopy. *The Journal of Physical Chemistry A*, 124(25):5170–5181, 2020.
- [200] Himmelwerk conductive materials and their properties with videos. <https://www.himmelwerk.com/en/technology/conductive-materials/>. Accessed: 2023-02-26.
- [201] JA Coxon, KVLN Sastry, JA Austin, and DH Levy. The microwave spectrum of the oh x 2 $\pi$  radical in the ground and vibrationally-excited ( $\nu$  6) levels. *Canadian Journal of Physics*, 57(5):619–634, 1979.
- [202] Gregory Bar and Andrew F Parsons. Stereoselective radical reactions. *Chemical Society Reviews*, 32(5):251–263, 2003.
- [203] JM Dreiling and Timothy J Gay. Chirally sensitive electron-induced molecular breakup and the vester-ulbricht hypothesis. *Physical review letters*, 113(11):118103, 2014.



- [204] Luc Vereecken and Jozef Peeters. A theoretical study of the oh-initiated gas-phase oxidation mechanism of  $\beta$ -pinene (c 10 h 16): first generation products. *Physical Chemistry Chemical Physics*, 14(11):3802–3815, 2012.
- [205] Lu Xu, Kristian H Møller, John D Crouse, Rasmus V Otkjær, Henrik G Kjaergaard, and Paul O Wennberg. Unimolecular reactions of peroxy radicals formed in the oxidation of  $\alpha$ -pinene and  $\beta$ -pinene by hydroxyl radicals. *The Journal of Physical Chemistry A*, 123(8):1661–1674, 2019.
- [206] Adrien Schlachter, Paul Asselin, and Pierre D Harvey. Porphyrin-containing mofs and cofs as heterogeneous photosensitizers for singlet oxygen-based antimicrobial nanodevices. *ACS Applied Materials & Interfaces*, 13(23):26651–26672, 2021.
- [207] David R Kearns. Physical and chemical properties of singlet molecular oxygen. *Chemical Reviews*, 71(4):395–427, 1971.
- [208] Marco Ruzzi, Elena Sartori, Alberto Moscatelli, Igor V Khudiyakov, and Nicholas J Turro. Time-resolved epr study of singlet oxygen in the gas phase. *The Journal of Physical Chemistry A*, 117(25):5232–5240, 2013.
- [209] Barbara Marchetti and Tolga NV Karsili. An exploration of the reactivity of singlet oxygen with biomolecular constituents. *Chemical Communications*, 52(73):10996–10999, 2016.
- [210] Jomana Al-Nu’airat, Mohammednoor Altarawneh, Xiangpeng Gao, Phillip R Westmoreland, and Bogdan Z Dlugogorski. Reaction of aniline with singlet oxygen (o2 1 $\delta$ g). *The Journal of Physical Chemistry A*, 121(17):3199–3206, 2017.
- [211] Andrew G Leach and KN Houk. Diels–alder and ene reactions of singlet oxygen, nitroso compounds and triazolinediones: transition states and mechanisms from contemporary theory. *Chemical communications*, (12):1243–1255, 2002.
- [212] Ashwini A Ghogare and Alexander Greer. Using singlet oxygen to synthesize natural products and drugs. *Chemical reviews*, 116(17):9994–10034, 2016.
- [213] Ivana Pibiri, Silvestre Buscemi, Antonio Palumbo Piccionello, and Andrea Pace. Photochemically produced singlet oxygen: applications and perspectives. *ChemPhotoChem*, 2(7):535–547, 2018.
- [214] Nicholas J Turro and Ming Fea Chow. Mechanism of thermolysis of endoperoxides of aromatic compounds. activation parameters, magnetic field, and magnetic isotope effects. *Journal of the American Chemical Society*, 103(24):7218–7224, 1981.
- [215] Peter R Ogilby and Christopher S Foote. Chemistry of singlet oxygen. 42. effect of solvent, solvent isotopic substitution, and temperature on the lifetime of singlet molecular oxygen (1. delta. g). *Journal of the American Chemical Society*, 105(11):3423–3430, 1983.